VŠB – Technical University of Ostrava
University Study Programmes
Nanotechnology Centre

Characterization of special anisotropic structures using Mueller matrix ellipsometry

Studium speciálních anizotropních struktur pomocí elipsometrie Muellerovy matice

2018

Author: Daniel Vala
Supervisor: doc. Dr. Mgr. Kamil Postava

VŠB - Technical University of Ostrava
University Study Programmes
CNT - Nanotechnology Centre

Bachelor Thesis Assignment

Student: **Daniel Vala**

Study Programme: B3942 Nanotechnology

Study Branch: 3942R001 Nanotechnology

Title: Characterization of special anisotropic structures using Mueller matrix ellipsometry
Studium speciálních anizotropních struktur pomocí elipsometrie Muellerovy matice

The thesis language: English

Description:

Optical nondestructive methods including Mueller matrix ellipsometry are recently applied for research of anisotropic structures and systems, for example, crystals with reduced symmetry or periodic diffracting systems and gratings. The main target of the Bachelor thesis is experimental measurement using the ellipsometer RC2 from Woollam company, preparation and characterization of samples, and application of theory to experimental data processing. The thesis mainly consists of:
1. Description of anisotropic optical response using Mueller matrix.
2. Growth and characterization of anisotropic molecular crystals and determination of their permittivity tensor spektra.
3. Characterization of diffraction structures using ellipsometric measurement of diffraction efficiency.

References:

1. E. Garcia-Caurel, et al., Advanced Mueller ellipsometry instrumentation and data analysis. Ellipsometry at the Nanoscale, Springer Berlin Heidelberg, 2013.
2. H. Fujiwara, Spectroscopic Ellipsometry: Principles and Applications, John Willey & Sons 2007.
3. R. M. A. Azzam and N. M. Bashara, Ellipsometry and Polarized Light, North-Holland, Amsterdam, 1977.
4. J. F. Nye -Physical properties of crystals-Oxford Clarendon Press 2006.
5. Optics and photonics – Holography – Methods of measuring diffraction efficiency and associated optical characteristics of holograms, ISO 17901-1:2015(E).

Extent and terms of a thesis are specified in directions for its elaboration that are opened to the public on the web sites of the faculty.

Supervisor: **doc. Dr. Mgr. Kamil Postava**

Date of issue: 10.11.2017

Date of submission: 21.05.2018

prof. Ing. Jaromír Pištora, CSc.
Head of Department

Ing. Zdeňka Chmelíková, Ph.D.
Vice-rectress for Study Affairs

Prohlašuji že,

- jsem celou bakalářskou práci včetně příloh vypracoval samostatně pod vedením vedoucího bakalářské práce a uvedl jsem všechny použité podklady a literaturu
- byl jsem seznámen s tím, že na moji bakalářskou práci se plně vztahuje zákon č. 121/2000 Sb. — autorský zákon, zejména §35 — užití díla v rámci občanských a náboženských obřadů, v rámci školních představení a užití díla školního a §60 — školní dílo
- beru na vědomí, že Vysoká škola báňská — Technická univerzita Ostrava (dále jen VŠB-TUO) má právo nevýdělečně ke své vnitřní potřebě bakalářskou práci užít (§35 odst. 3)
- souhlasím s tím, že jeden výtisk bakalářské práce bude uložen v Ústřední knihovně VŠB-TUO k prezenčnímu nahlédnutí a jeden výtisk bude uložen u vedoucího bakalářské práce. Souhlasím s tím, že údaje o bakalářské práci, obsažené v Záznamu o závěrečné práci, umístěném v příloze mé bakalářské práce, budou zveřejněny v informačním systému VŠB-TUO
- bylo sjednáno, že s VŠB-TUO, v případě zájmu z její strany, uzavřu licenční smlouvu s oprávněním užít dílo v rozsahu §12 odst. 4 autorského zákona
- bylo sjednáno, že užít své dílo — bakalářskou práci nebo poskytnout licenci k jejímu využití mohu jen se souhlasem VŠB-TUO, která je oprávněna v takovém případě ode mne požadovat přiměřený příspěvek na úhradu nákladů, které byly VŠB-TUO na vytvoření díla vynaloženy (až do jejich skutečné výše)
- beru na vědomí, že odevzdáním své práce souhlasím se zveřejněním své práce podle zákona č. 111/1998 Sb., o vysokých školách a o změně a doplnění dalších zákonů (zákon o vysokých školách), ve znění pozdějších předpisů, bez ohledu na výsledek její obhajoby

V Ostravě 21. 5. 2018

Daniel Vala
Ahepjukova 2812/5,
Ostrava, Czech Republic

I hereby declare that this bachelor's thesis was written by myself. I have quoted all the references I have drawn upon.

In Ostrava, 21. 5. 2018 .....

Daniel Vala

At this point, I would like to thank all those, who have helped in writing this thesis in any way. The greatest gratitude belongs to my supervisor doc. Dr. Mgr. Kamil Postava for his unwavering patience, warm approach, countless suggestive and his precious time-consuming consultations, without which this work would not be brought to its present form. I also thank Ing. Martin Mičica for his hints and tips during the crystal growth and discussions about the optical activity, Ing. Tomáš Kohut for help with the design and the realization of the diffraction efficiency measurements, doc. Ing. Jonáš Tokarský, PhD., and Ing. Mgr. Daniel Cvejn, PhD. for consultations focusing on general chemistry and the optical activity, Ing. Petra Váňová, PhD., and Mrs. Naděžda Brychtová for the possibility of using their metallographic laboratory, and Dr. Ing. Dalibor Matýsek for the crystallographic consultations and beautiful transmission polarization microscopy images.

Last but not least, many and many thanks belongs to my family, friends, colleagues, and especially girlfriend Nikola for their patience, all the support and moral help in writing this thesis.

Abstrakt

Záměrem této bakalářské práce je rozšířit a rozvinout techniku měření pomocí elipsometrie Muellerovy matice. V rámci této práce byla navrhnuta původní metoda měření optické aktivity a exkluzivně přes širokou spektrální oblast mezi 400–900 nm byla vypočtena specifická optická stáčivost cukerných roztoků. K ověření správnosti této metody bylo použito Lu-Chipmanova rozkladu. Značný důraz byl v této práci kladen na pěstování monokrystalů sacharózy a kokrystalů butandiových kyselin metodou pomalé evaporace. Výsledkem jsou kvalitní krystaly, jejichž monokrystalická struktura byla potvrzena užitím polarizačního mikroskopu. Za účely budoucího výzkumu byla elipsometricky změřena optická spektra minerálů pyritu a kasiteritu, přičemž jejich dielektrické tensory byly vypočítány užitím modelů splňující Kramers-Kronigovy relace. Jeden z cílů této práce je také charakterizace difrakčních struktur. Přenastavením a změnou hardwarové konfigurace RC2 elipsometru společnosti Woollam bylo dosaženo možnosti automaticky a efektivně charakterizovat blejzované difrakční mřížky, za účelem stanovení jejich difrakčních účinností.

Klíčová slova: blejzovaná difrakční mřížka, butandiové kyseliny, dielektrický tensor, difrakční účinnost, elipsometrie Muellerovy matice, Lu-Chipmanův rozklad, optická aktivita roztoků, specifická optická stáčivost, pěstování a růst monokrystalů

Abstract

This bachelor thesis is focused on the developement and extension of the Mueller matrix spectroscopic ellipsometry measurement techniques. A novel method of optical activity measurement was developed and specific rotatory powers of the saccharides solutions were calculated exclusively over spectral range of 400–900 nm. Lu-Chipman decomposition of according experimental Mueller matrix was conducted to confirm the corectness of the method. Particular emphasis was placed on the growth of sucrose monocrystal and butanedioic acid cocrystals using slow evaporation method. Good-quality monoctystals were grown as was verifyed using polarization microscopy. For the purpose of future research, pyrite and cassiterite minerals were measured ellipsometrically, and their dielectric tensor spectra were determined using Kramers-Kronig consistent models. The one of this thesis goals is also to characterize the diffraction structures. We rearrange the standard Woollam RC2 ellipsometer reflection configuration used for the measurements, to acquire the possibility of extended and automated characterization of blazed diffraction gratings, in order to calculate the diffraction efficiencies of these diffraction structures.

Key Words: blazed diffraction grating, butanedioic acids, monocrystal growth, dielectric tensor, diffraction efficiency, Lu-Chipman decomposition, Mueller matrix ellipsometry, optical activity of solutions, specific rotation power

Contents

List of symbols and abbreviations

Symbols and abbreviations used throughout the thesis are defined and alphabetically ordered here. Symbols with only local meaning are defined close to where they are used, and are not included here.

$\boldsymbol{g}$	–	normal vector to the grating surface
$\boldsymbol{k}$	–	wave vector
$\boldsymbol{n}$	–	normal vector to the grating facet
$\boldsymbol{r}$	–	radius vector
$\hat{\boldsymbol{u}}$	–	unit vector $\boldsymbol{u}$
$\boldsymbol{D}$	–	electric displacement
$\boldsymbol{D}_{\mathrm{m}}$	–	diattenuation vector
$\boldsymbol{E}$	–	electric field
$\tilde{\boldsymbol{E}}$	–	complex amplitude of Electric field
$\boldsymbol{H}$	–	magnetic field
$\mathbf{J}$	–	Jones matrix
$\boldsymbol{J}$	–	Jones vector
$\boldsymbol{J}^*$	–	complex conjugate of $\boldsymbol{J}$
$\boldsymbol{J}^{\mathrm{T}}$	–	transposed $\boldsymbol{J}$
$\boldsymbol{J}^\dagger$	–	Hermitean adjoint of $\boldsymbol{J}$
$\mathbf{M}$	–	Mueller matrix
$\mathbf{M}_{\mathrm{D}}$	–	Diatenuattion Mueller matrix
$\mathbf{M}_{\mathrm{J\text{-}M}}$	–	Jones-Mueller matrix
$\mathbf{M}_{\mathrm{NCS}}$	–	Mueller matrix of the NCS system
$\mathbf{M}_{\mathrm{R}}$	–	Retardance Mueller matrix
$\mathbf{M}_{\Delta}$	–	Depolarization Mueller matrix
$\boldsymbol{S}$	–	Stokes vector
$\boldsymbol{P}_{\mathrm{m}}$	–	polarizance vector
a_e	–	lattice parameter along a-axis
b_e	–	lattice parameter along b-axis
c	–	concentration
c_e	–	lattice parameter along c-axis
c_{im}	–	impurity concentration in solution
d	–	grating period
e	–	Euler number
g_i	–	i-fold symmetry axis
i	–	imaginary unit
k	–	imaginary part of the refractive index
$k_{\mathrm{i,t}}$	–	tangential component of the incident wave vector

$k_{\mathrm{m,t}}$ – tangential component of the wave vector diffracted in the order m
k_{B} – Boltzmann constant
l – length of cuvette
m – plane of symmetry
m – mass
m_{ij} – Mueller matrix components
n – refractive index
n_m – ammount of substance
p – pressure
r – radius
r_{c} – critical radius of sphere embryo
$r_{\mathrm{s,p}}$ – Fresnel reflection coefficients of s and p-polarized wave
$r_{\mathrm{ss,pp}}$ – Fresnel reflection coefficients with no polarization conversion
$r_{\mathrm{sp,ps}}$ – Fresnel reflection coefficients with polarization conversion
t – time
v – light speed in medium with refraction index n
v_c – speed of light in vacuum
v_ω – angular frequency
A – Cauchy dispersion parameter
B – Cauchy dispersion parameter
C – centre of the symmetry of the crystal
C – Cauchy dispersion parameter
D – diatenuattion
E – photon energy
G_{im} – face growth rate in the presence of impurity
$G_{(l)}$ – absolute Gibbs energy of liquid
R_{p} – face growth rate in pure solution
$G_{(s)}$ – absolute Gibbs energy of solid
ΔG – Gibbs free energy
ΔG_{max} – Gibbs energy value related with r_{c}
ΔG_{V} – Gibbs energy of volume of the nucleus
ΔH – change of the enthalpy
$I_{\mathrm{x,y}}$ – intensity of the wave in x and y direction
I_{45} – intensity of the wave in direction 45° from the x(y) axis.
$I_{\mathrm{LCP,RCP}}$ – intensity of the LCP and RCP wave
K – Langmuir adsorption isotherm constant
L – separation of active sites available for impurity adsorption
M – molar mass
P – Cauchy principal value

P_Δ – depolarization index
R – retardance
R_{im} – step velocity in the presence of impurity
R_{p} – step velocity in pure solution
S – entropy
S_{c} – surface area occupied by one crystallizing molecule
$S_{\mathrm{substance}}$ – solubility of the substance
V – volume
α – angle of rotation of the Cartezian coordinate system
α_e – Euler angle between b_e and c_e
α_{obs} – observed angle of optical rotation
$[\alpha]_\lambda^T$ – specific rotatory power at wavelength λ and temperature T
β_e – Euler angle between a_e and c_e
γ_e – Euler angle between a_e and b_e
δ – absolute phase
$\varepsilon_{1,2}$ – real and imaginary part of pseudodielectric function
ε_r – relative permittivity
$\hat{\varepsilon}$ – permittivity tensor
ζ – effectiveness factor of an impurity
θ_{B} – blaze angle
λ – wavelength
λ_i – eigenvalue
μ – permeability
μ_i – chemical potential of i-th substance
μ_r – relative permeability
ξ – angle between the 3rd phase surface and (l)-(s) interface surface tension component
π – Ludolph's number
ρ – r_{p} and r_{s} ratio
σ – surface tension
φ – angle of incidence
ψ – ellipsometric angle
ω – frequency
Δ – ellipsometric angle
Δ_p – depolarizance
Ξ – relative supersaturation
Ω – fractional surface coverage of the crystal surface impurities
$\mathscr{P}(\mathscr{P}_c, r)$ – Poincaré sphere with centre $\mathscr{P}_{\mathrm{c}}$ and radius r
$\mathrm{tr}(\mathbf{M})$ – trace of $\mathbf{M}$

$\otimes$	–	Cronecker product
$f = f(x)$	–	function of variable x
$\mathrm{d}f$	–	total differential of function f
$\frac{\mathrm{d}f(x)}{\mathrm{d}x}$	–	derivation of f with respect to x
$\frac{\partial f(x,y,...)}{\partial x}$	–	partial derivation of f with respect to x
DNA	–	Deoxyribonucleic acid
IR	–	Infrared
LCP	–	Left cirucular polarization
LTA	–	L-tartaric acid
RCP	–	Right circular polarization
SCA	–	Succinic acid
USA	–	Urea-succinic acid cocrystal
XRD	–	X-Ray Diffraction

1 Introduction

Nowdays, the Mueller matrix spectroscopic ellipsometry is a very widespread optical and nondestructive method suitable for complex description of the optical response of matter [1]. The Mueller matrix ellipsometers analyze the change of the polarized light properties after the interaction with the matter. The change of the polarization state between incident and reflected beam is particularly sensitive to many physical phenomena within the sample. Therefore, the Mueller matrix spectroscopic ellipsometry is very powerful method, how to describe broad variety of the samples, from very simple isotropic thin films [2], through liquids [3] and anisotropic crystals [4], to very complex biological structures, e.g. butterflies [5], human tissues [6, 7, 8, 9]. In fact, the latter are practically optically indefinable, and special sample preparation and data analysis must be performed. Currently, Mueller matrix decompositions [10, 11, 12, 13] represent the most promising method, how to deal with these structures. If performed correctly, it can be further determined, if such a tissue is cancerous or not [14]. Author of this work further considers this fact to be the most important and crucial application of Mueller matrix ellipsometry and therefore as an incentive to write this work.

The goal of my bachelor thesis is to bring new characterization techniques of anisotropic samples, develop the new and extend the standard techniques of the Mueller matrix ellipsometry measurements, and to bring a new insight into the field of the ostensibly explored phenomenons. The secondary objective of this work is to provide a introductory, but comprehensive view into the analysis of the most complicated samples measurements through characterizing various types of anisotropic, but less chaotic and more descriptive samples.

In the first part of this work, the optical activity of saccharides solutions is shown. The often used simple chemical spectrometers are spectraly limited using monochromatic source only. The specific rotatory power is therefore broadly tabulated for a single wavelength 589 nm. We propose a novel method, how to efficiently measure the optical activity parameters in the spectral range from 193 nm to 1700 nm using the Woollam RC2 Mueller matrix spectroscopic ellipsometer. The great advantage and a big potential of our method is the ability to measure also mutarotation effects and reaction kinetics.

The second part of this work is focused on the growth and measurement of the anisotropic crystals. Great emphasis is laid on the growth of the monocrystals and their preparation for the ellipsometric measurements. The organic molecular crystals of tartaric acid, D-(+)-sucrose and 2:1 Urea-Succinic acid cocrystal are in the field of this study, due to the presence of the hydrogen bonds in their structure. According to their vibration spectra, they can act as a potential source in the nonlinear applications, e.g. terahertz lasers. Ellipsometric measurements of the anisotropic crystals are treated on pyrite and cassiterite minerals, and their dielectric tensor spectra are calculated.

Apart from the Mueller matrix measurements, we further extend the ability of the Woollam RC2 ellipsometer to measure diffraction efficiencies of the diffraction structures. Arranging the

ellipsometer into special reflection configuration, the blazed diffraction grating with a period of 1000 nm was measured in order to obtain absolute diffraction efficiencies as the dependances of the reflected angle and the wavelength. Our configuration offers a viable way how to measure even more complicated structures e.g. safety holograms.

2 Properties and measurement of the polarized light

In electromagnetism, in general, and in optics in particular, rigorous description of every physically reliable phenomena can be treated by solving the Maxwell's equations [15]. In this Chapter, we derive the polarization properties of the light from the Maxwell's equations in order to introduce the Jones and Mueller formalism and discuss their physical meaning, applicability and measurements.

2.1 Maxwell's equations

The following equations show Maxwell's equation in well-known differential form:

$$\boldsymbol{\nabla} \cdot \boldsymbol{D} = \rho \tag{2.1}$$

$$\boldsymbol{\nabla} \cdot \boldsymbol{B} = 0 \tag{2.2}$$

$$\boldsymbol{\nabla} \times \boldsymbol{H} = \boldsymbol{j} + \frac{\partial \boldsymbol{D}}{\partial t} \tag{2.3}$$

$$\boldsymbol{\nabla} \times \boldsymbol{E} = -\frac{\partial \boldsymbol{B}}{\partial t} \tag{2.4}$$

Now, it is possible to solve any problem using these equations describing the most complex variant of any particular problem. Despite the fact we always obtain very correct solution by treating with these equations, it comes out, that the actual math on them could be needlessly difficult and unnecessary. For purposes of this Bachelor thesis, it is sufficient to assume reduced form of the equations.

Consider homogenous linear insulator with no surface carriers and no electrical conductivity. We get reduced Maxwell's equations:

$$\boldsymbol{\nabla} \cdot \boldsymbol{D} = 0 \tag{2.5}$$

$$\boldsymbol{\nabla} \cdot \boldsymbol{H} = 0 \tag{2.6}$$

$$\boldsymbol{\nabla} \times \boldsymbol{H} = \frac{\partial \boldsymbol{D}}{\partial t} \tag{2.7}$$

$$\boldsymbol{\nabla} \times \boldsymbol{E} = -\mu \frac{\partial \boldsymbol{H}}{\partial t} \tag{2.8}$$

Please make note, that just shown equations desribe also anisotropic media, in other words,

$$\boldsymbol{D} = \hat{\varepsilon} \boldsymbol{E}. \tag{2.9}$$

For derivation of the polarization properties of the light, we are free to consider the isotropic media – we deal with the dielectric tensor $\hat{\varepsilon}$ as with scalar ε. If we substitute (2.8) into (2.7) and

use some vector algebra, we obtain the wave equation for homogenous, isotropic, linear media with no charge and conductivity [16],

$$\nabla^2 \boldsymbol{E} - \mu\varepsilon \frac{\partial^2 \boldsymbol{E}}{\partial t^2} = 0. \tag{2.10}$$

2.2 Jones calculus

The partial differential equation (2.10) is satisfied for the wave with the amplitude $\tilde{E}$ propagating along direction given by radius vector r with frequency ω and absolute phase δ:

$$\boldsymbol{E}(\boldsymbol{r}, t) = \mathrm{Re}\Big\{\tilde{E}(\boldsymbol{r}) e^{i\omega t}\Big\} = \tilde{E}\cos(\omega t - \boldsymbol{k}\cdot\boldsymbol{r} + \delta) \tag{2.11}$$

Now, the wave can be decomposed into the superpostition of two mutually orthogonal modes propagating along directions given by its unit vectors $\hat{\boldsymbol{u}}_{\mathrm{i}}$ [17]:

$$\boldsymbol{E}(\boldsymbol{r}, t) = \Big[\tilde{E}_{\mathrm{u1}}\cos(\omega t - \boldsymbol{k}\cdot\boldsymbol{r} + \delta_1)\Big]\,\hat{\boldsymbol{u}}_{\boldsymbol{1}} + \Big[\tilde{E}_{\mathrm{u2}}\cos(\omega t - \boldsymbol{k}\cdot\boldsymbol{r} + \delta_2)\Big]\,\hat{\boldsymbol{u}}_{\boldsymbol{2}} \tag{2.12}$$

Vectors $\hat{\boldsymbol{u}}_{\boldsymbol{1}}$ and $\hat{\boldsymbol{u}}_{\boldsymbol{2}}$ can be chosen to be the unit vectors along the x and y direction in the Cartezian coordinate system oriented with z-axis the wave propagation, therefore the superposition (2.12) completely determines the polarization state of the wave. It is possible to get rid off the summation, rewriting (2.12) into the vector form $\Big([\boldsymbol{E}(\boldsymbol{r},t)]_{\mathrm{x}},\ [\boldsymbol{E}(\boldsymbol{r},t)]_{\mathrm{y}}\Big)^{\mathrm{T}}$. From geometry of the problem, it is easy to see, that $\hat{\boldsymbol{x}}\cdot\hat{\boldsymbol{y}} = 0 \wedge \hat{\boldsymbol{x}}\cdot\hat{\boldsymbol{z}} = 0$, so we can write $\Big([\boldsymbol{E}(z,t)]_{\mathrm{x}},\ [\boldsymbol{E}(z,t)]_{\mathrm{y}}\Big)^{\mathrm{T}}$. Note, that the frequency of the wave is invariant with the time, therefore ωt in (2.12) can be supressed. The polarization state of the wave remains the same in every point of the space, so without loss of generality, the spatial information of the wave can be dropped by simply chosing $z = 0$. The resulting vector is called the **Jones vector** and it completely determines the polarization state of the wave:

$$\boldsymbol{J} = \begin{pmatrix} |E_{\mathrm{x}}|\ \mathrm{e}^{i\delta_x} \\ |E_{\mathrm{y}}|\ \mathrm{e}^{i\delta_y} \end{pmatrix} \tag{2.13}$$

The intensity of the wave is given by multiplying the Jones vector by its Hermitian adjoint $\boldsymbol{J}^{\dagger}$,

$$I = \boldsymbol{J}^{\dagger}\boldsymbol{J}. \tag{2.14}$$

If we consider a wave of unit intensity, we call the wave to be normalized. The Jones vector of such a wave is normal too.

Every pair of two orthonormal Jones vectors generates two-dimensional linear space. This pair is called a set of basis vectors. Because the basis vectors are linearly independent, every vector in the linear space can be expressed as a linear combination of the set of basis vectors [18]. In matrix form, this linear combination is represented by 2×2 transformation matrix. For

example, transformation of the Jones vector upon rotation in xy plane by the angle α is expressed as follows:

$$\begin{pmatrix} E_{\mathrm{x}+\alpha} \\ E_{\mathrm{y}+\alpha} \end{pmatrix} = \begin{pmatrix} \cos\alpha & \sin\alpha \\ -\sin\alpha & \cos\alpha \end{pmatrix} \begin{pmatrix} E_{\mathrm{x}} \\ E_{\mathrm{y}} \end{pmatrix} \tag{2.15}$$

The matrix, which describes the transformation of the Jones vector by a polarization optical component is called the Jones matrix $\mathbf{J}$,

$$\boldsymbol{J'} = \mathbf{J}\boldsymbol{J}. \tag{2.16}$$

2.3 Mueller calculus

Altough the Jones calculus is very effective and elegant mathematical way, how to describe totally polarized light and its transformations, it is *impossible* to use this formalism when treating with unpolarized light. Beside this extremes of totally polarized and totally unpolarized light, we very often have to deal with partially polarized light. In order to do so, we have to implement more complex formalism and define the Stokes vector $\boldsymbol{S}$ [1, 17, 19]:

$$\boldsymbol{S} = \begin{pmatrix} I_{\mathrm{x}} + I_{\mathrm{y}} \\ I_{\mathrm{x}} - I_{\mathrm{y}} \\ I_{45} - I_{\text{-}45} \\ I_{\mathrm{LCP}} - I_{\mathrm{RCP}} \end{pmatrix}, \tag{2.17}$$

where I_{x}, I_{y}, $I_{\pm 45}$, denotes the wave intensities along the x, y, $\pm 45°$ directions, respectively. I_{LCP} and I_{RCP} defines the intensities of left-circular polarized (LCP) and right-circular polarized light (RCP), respectively.

In order to find the transformation matrix of the arbitrary optical system between input and output Stokes vectors, let us define the coherence vector $\boldsymbol{C} = \left(\langle E_{\mathrm{x}} E_{\mathrm{x}}^{*} \rangle, \left\langle E_{\mathrm{x}} E_{\mathrm{y}}^{*} \right\rangle, \langle E_{\mathrm{y}} E_{\mathrm{x}}^{*} \rangle, \left\langle E_{\mathrm{y}} E_{\mathrm{y}}^{*} \right\rangle\right)^{\mathrm{T}}$. The relation between $\boldsymbol{C}$ and $\boldsymbol{S}$ is given:

$$\begin{pmatrix} S_0 \\ S_1 \\ S_2 \\ S_3 \end{pmatrix} = \begin{pmatrix} 1 & 0 & 0 & 1 \\ 1 & 0 & 0 & -1 \\ 0 & 1 & 1 & 0 \\ 0 & -i & i & 0 \end{pmatrix} \begin{pmatrix} \langle E_{\mathrm{x}} E_{\mathrm{x}}^{*} \rangle \\ \left\langle E_{\mathrm{x}} E_{\mathrm{y}}^{*} \right\rangle \\ \langle E_{\mathrm{y}} E_{\mathrm{x}}^{*} \rangle \\ \left\langle E_{\mathrm{y}} E_{\mathrm{y}}^{*} \right\rangle \end{pmatrix} \tag{2.18}$$

We often call S_0–S_3 parameters to be the Stokes parameters. The 4×4 matrix in Eq. (2.18) is widely known as the $\mathbf{A}$ matrix. In the most general case, when partially depolarized light interacts with depolarizing optical system, the transformation between input and output $\boldsymbol{C}$ is

given by

$$\boldsymbol{C}' = \mathbf{F}\boldsymbol{C} = \langle \mathbf{J} \otimes \mathbf{J}^* \rangle \, \boldsymbol{C}, \tag{2.19}$$

where $\mathbf{F}$ is the coherence matrix, and symbol $\otimes$ stands for a Cronecker product. Substituting (2.19) into (2.18), we get

$$\boldsymbol{S}' = \mathbf{A} \, \langle \mathbf{J} \otimes \mathbf{J}^* \rangle \, \mathbf{A}^{-1} \boldsymbol{S}. \tag{2.20}$$

The transformation matrix of the polarization system between input and output Stokes vectors is called the **Mueller matrix** and is defined as follows:

$$\boldsymbol{S}' = \begin{pmatrix} S_0' \\ S_1' \\ S_2' \\ S_3' \end{pmatrix} = \begin{pmatrix} m_{11} & m_{12} & m_{13} & m_{14} \\ m_{21} & m_{22} & m_{23} & m_{24} \\ m_{31} & m_{32} & m_{33} & m_{34} \\ m_{41} & m_{42} & m_{43} & m_{44} \end{pmatrix} \begin{pmatrix} S_0 \\ S_1 \\ S_2 \\ S_3 \end{pmatrix} \equiv \mathbf{M}\boldsymbol{S}. \tag{2.21}$$

Finally, comparing (2.21) with (2.20), the Mueller matrix can be calculated using

$$\mathbf{M} = \mathbf{A} \, \langle \mathbf{J} \otimes \mathbf{J}^* \rangle \, \mathbf{A}^{-1}. \tag{2.22}$$

More detailed discussion about understanding and interpretation of the Mueller matrix, geometrical interpretation of Stokes vector, and the cases of partially polarized light are presented in the following sections.

2.4 Interpretation and physical meaning of the Mueller matrix

2.4.1 Jones-Mueller matrix

When speaking about ellipsometry, arbitrary orthogonal set of unit vectors in (2.12), is replaced with axes oriented along the directions perpendicular (s-polarization) and parallel (p-polarization) to the plane of incidence. If we consider nondepolarizing plane anisotropic sample, Eq. (2.16) can be rewriten in terms of the reflection coefficients as follows [19],

$$\begin{pmatrix} E_{\mathrm{s}}^{\mathrm{out}} \\ E_{\mathrm{p}}^{\mathrm{out}} \end{pmatrix} = \begin{pmatrix} r_{\mathrm{ss}} & r_{\mathrm{sp}} \\ r_{\mathrm{ps}} & r_{\mathrm{pp}} \end{pmatrix} \begin{pmatrix} E_{\mathrm{s}}^{\mathrm{in}} \\ E_{\mathrm{p}}^{\mathrm{in}} \end{pmatrix}. \tag{2.23}$$

Note, that equation bellow reffers to reflection configuration, but it is correct also for transmission, when calculating with tramsission coefficients. The non-diagonal elements determines the conversion between polarizations. This phenomenom is very common, when speaking about anisotropic samples, e.g. non-cubic crystals. For example, r_{ps} describes how much intensity of p-polarized wave is reflected into s-polarized wave. In Section 2.3 was shown, that from every Jones vector can be derived corresponding Stokes vector. Using Eq. (2.22), the same procedure

can be done when transforming Jones matrix to Mueller matrix. The calculated Mueller matrix can be abstractly divided into the quadrants, and the elements of the first and third quadrant (m_{13}, m_{14}, m_{23}, m_{24}, m_{31}, m_{32}, m_{41} and m_{42}) are connected with anisotropic phenomena of the sample.

Conversion (2.24) can be done for any Jones matrix – every Jones matrix has physically relieable Mueller matrix, but not every Mueller matrix has appropriate Jones matrix. The inverse conversion can be formaly done always for non-depolarizing optical system, otherwise, the operation would lead to the unphysical result. The non-depolarizing Mueller matrix is called the pure Mueller matrix or the Jones-Mueller matrix. Several necessary conditions were algebraicaly derived, however the sufficient condition was proposed by Cloud: The coherency matrix must be definite positive – all eigenvalues are non-negative and one must be strictly positive. [21]

The depolarization abillity of the Mueller matrix can be derived from necessary condition $\mathrm{tr}\left(\mathbf{M}^{\mathrm{T}}\mathbf{M}\right) = 2m_{00}$ and is given by the depolarization index [20]:

$$P_{\Delta} = \frac{\sqrt{\mathrm{tr}\left(\mathbf{M}^{\mathrm{T}}\mathbf{M}\right) - m_{11}^2}}{\sqrt{3}m_{11}} \in \langle 0; 1\rangle \tag{2.24}$$

Note, that the most general form of the Mueller matrix is reduced into the block-diagonal form in the case of isotropic and nondepolarizing sample.

$$\mathbf{M}_{\mathrm{NCS}} = \begin{pmatrix} 1 & -N & 0 & 0 \\ -N & 1 & 0 & 0 \\ 0 & 0 & C & S \\ 0 & 0 & -S & C \end{pmatrix}, \tag{2.25}$$

where

$$N = \cos 2\psi \tag{2.26}$$

$$C = \sin 2\psi \sin \Delta \tag{2.27}$$

$$S = \sin 2\psi \cos \Delta. \tag{2.28}$$

The ellipsometric angles ψ, Δ will be discussed in Section 2.5.

2.4.2 Mueller matrix decomposition

We showed, that calculation of the Jones matrix from the Jones-Mueller matrix is straightforward. To obtain corresponding Jones matrix from a depolarizing Mueller matrix, calculation based on a Mueller matrix decomposition is needed. Mueller matrix decompositions are devided into 2 cathegories – the sum and the product decomposition.

Cloud derived, that any Mueller matrix can be decomposed on the sum of 4 Mueller matrices, each multiplied by eigenvalue of related coherency matrix.

$$\mathbf{M} = \lambda_1\mathbf{M}_1 + \lambda_2\mathbf{M}_2 + \lambda_3\mathbf{M}_3 + \lambda_4\mathbf{M}_4 \tag{2.29}$$

Considering a nondepolarizing sample, the closest Jones-Mueller matrix is given by $\mathbf{M}_{\text{J-M}} \approx \lambda_1\mathbf{M}_1$, while the rest is related with the noise [21].

Apart from the sum decompositions, the product decompositions are very advantagenous for understanding particular physical phenomena of given experimental Mueller matrix. Lu-Chipman decomposition is a great tool for obtain the Mueller matrices each describing only one attribute (depolarization Δ, retardance R and diattenuation D, respectively) of the experimental matrix [11]:

$$\mathbf{M} = \mathbf{M}_\Delta\mathbf{M}_\text{R}\mathbf{M}_\text{D} \tag{2.30}$$

For following purposes, it is convinient to define polarizance $\boldsymbol{P}_\text{m}$ and diatenuattion vectors$\boldsymbol{D}_\text{m}$.

$$\boldsymbol{P}_\text{m} = \frac{1}{m_{11}}\begin{pmatrix} m_{21} \\ m_{31} \\ m_{41} \end{pmatrix} \tag{2.31}$$

$$\boldsymbol{D}_\text{m} = \frac{1}{m_{11}}\begin{pmatrix} m_{12} \\ m_{13} \\ m_{14} \end{pmatrix} \tag{2.32}$$

It allows us to rewrite Mueller matrix in the partitioned form:

$$\mathbf{M} = m_{11}\begin{pmatrix} 1 & \boldsymbol{D}_\text{m}^\text{T} \\ \boldsymbol{P}_\text{m} & \mathbf{m} \end{pmatrix}, \tag{2.33}$$

where $\mathbf{m}$ is 3x3 Mueller submatrix. It is obvious, that retardance and diatenuattion is basically described with given experimental matrix. Calculation of depolarization matrix leads to the eigenvalue problem. From these matrices, qualitative parameters retardance, depolarization and diatenuattion are defined:

$$\Delta = 1 - \frac{|\text{tr}\,(\mathbf{M}_\Delta) - 1|}{3} \tag{2.34}$$

$$R = \arccos\left[\frac{\text{tr}\,(\mathbf{M}_\text{R})}{2} - 1\right] \tag{2.35}$$

$$D = \sqrt{m_{12}^2 + m_{13}^2 + m_{14}^2} \tag{2.36}$$

Note, that this technique was further developed mostly by Ossikovski (e.g. in [12]), where one of the possible (physically meaningfull) way, how to the Mueller matrix is decomposed, is into product of two retardation, two diatenuattion and one depolarization matrix, respectively.

2.4.3 Geometrical representation of polarization states and depolarization

For certain applications and for better visualisation, any polarization state of the light given by the Stokes vector can be represented by a point on the spherical surface – Poincaré sphere $\mathscr{P}$, see Fig. 2.1. [17].

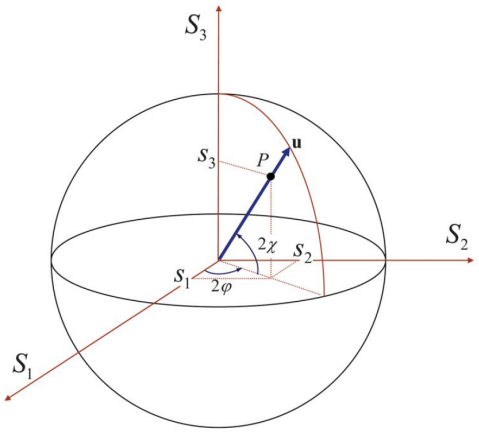

Figure 2.1: Poincaré sphere and Stokes parameters. Vector $\boldsymbol{u}$ on the picture describes general elliptical polarization state [22].

Stokes parameters are related to longitude (ellipticity) χ and latitude (azimuth) φ as follows:

$$S_1 = \cos 2\chi \cos 2\varphi \tag{2.37}$$

$$S_2 = \cos 2\chi \sin 2\varphi \tag{2.38}$$

$$S_3 = \sin 2\chi \tag{2.39}$$

It is easy to see, that the equator represents the linear polarization states of the light ($\chi = 0°$), while the south and north poles represent LCP and RCP states, respectively ($2\chi = 90°$). The hemispheres are related with the elliptical states. The parameter S_0 is connected with the radius of the sphere. For totally polarized Stokes vector, all polarization states are represented by the points on the surface of sphere $\mathscr{P}\,(0,\,1)$. In the case of depolarizations, the sphere is shrinked into $\mathscr{P}\left(0,\,\frac{1}{\sqrt{S_1^2+S_2^2+S_3^2}}\right)$. The unpolarized light is represented by the centre of the sphere. Using this representation, one can express every Stokes vector as a restriction of $\mathscr{P}$.

For a deeper understanding of the meaning of the experimental Mueller matrices, let us describe the geometrical meaning of the Lu-Chipman decomposition as shown in Fig. 2.2. The Poincaré spheres show the Stokes vectors after transformation by given Mueller matrix. The transformation of the Stokes vector after interaction with the sample characterized by $\mathbf{M} = \mathbf{M}_\Delta$ maps the sphere onto centered ellipsoid, according to the degree of depolarization (Fig. 2.2 left). If the sample is partially depolarizing retardation element characterized by $\mathbf{M} = \mathbf{M}_\Delta\mathbf{M}_\mathrm{R}$, the Poincaré sphere is shrinked and rotated (Fig. 2.2 centre) and for arbitrary optical element given

by $\mathbf{M} = \mathbf{M}_\Delta \mathbf{M}_\mathrm{R} \mathbf{M}_\mathrm{D}$ moreover displaces the ellipsoid from the origin of the Poincaré sphere (Fig. 2.2 right). Note, that the order of multiplication between the matrices must be respected.

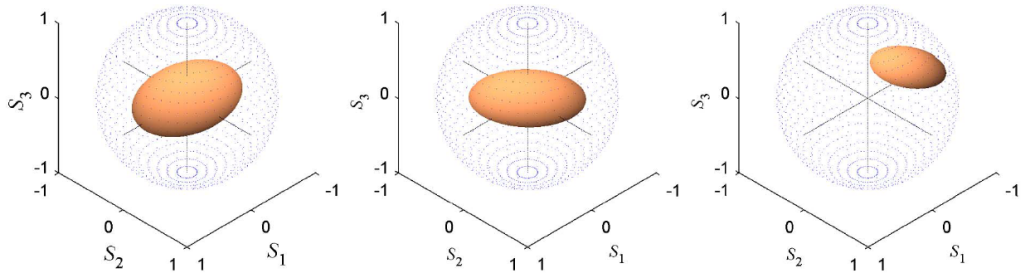

Figure 2.2: Poincaré sphere of the Stokes vector transformed by **Left:** a pure depolarizer, $\mathbf{M} = \mathbf{M}_\Delta$. **Centre:** depolarizer followed by retarder, $\mathbf{M} = \mathbf{M}_\Delta \mathbf{M}_\mathrm{R}$. **Right:** depolarized followed by retarder and diattenuator. $\mathbf{M} = \mathbf{M}_\Delta \mathbf{M}_\mathrm{R} \mathbf{M}_\mathrm{D}$ [22].

For further reading, kindhearted reader will find more in [22].

2.5 Spectroscopic ellipsometry

Whenever we are able to measure the change of the polarization property[1] of the light after interaction with measured sample, we call this measurement ellipsometry. In order to do that, there are 2 basic types of ellipsometers – rotating optical elements and phase-modulation ellipsometers. For purposes of this thesis, only rotation elements ellipsometers will be briefly described in following paragraphs.

The essential optical elements of every ellipsometer are polarizer and analyzer. Rotating-analyzer ellipsometers measure transmitted light intensity as the dependence on the instantaneous rotation of the analyzer. This function is measured in the form of Fourier series, where the Fourier coefficients must also be periodical functions. Therefore calculation of S_0–S_2 parameters is straightforward. However, LCP and RCP light intensities show the same angular dependence and can't be separated of each other – S_3 parameter cannot be calculated. This insufficiency can be eliminated by adding other optical component – a retarder, in the terms of ellipsometry usually called a compensator. It was shown, that placing the compensator in front of the rotating analyzer or behind the rotating polarizer is suitable way, how to measure also S_3 parameter, but still not all 16 elements of the Mueller matrix [1, 19].

First theoretical prediction of the full Mueller matrix ellipsometry was in 1973 by fixing the analyzer and the polarizer and addition of two rotating compensators before and after them, respectively. It was derived how the Mueller matrix can be obtained by direct analysis of the signal, further pointing out, that for the Fourier analysis of the signal, the ideal v_ω ratio between

[1] The *change* of the polarization state of the reflected beam must be compared to apriori known polarization state of the incident beam. Then, elements of the Mueller matrix can be calculated. *Polarizaton state* can be understood in terms of Stokes parameters, Poincaré representation, even in terms of change of ellipticity as plane projection of two eigenstates given by Jones basis vectors. But *always*, you must pay attention to the physical meaning of actual particular case you are treating with.

the compensators is 5:1 [23]. By further investigation of the intensity-angle dependances, 4.4–5:1, 2.5:1 and 3.5:1 ratios are equivalent – ideal [24]. Appart from that, classic PA ellipsometers are most likely set to $v_{\omega A}/v_{\omega P}$ ratio 3:1 [25]. The optical configurations and related measurable quantities are described in Fig. 2.3.

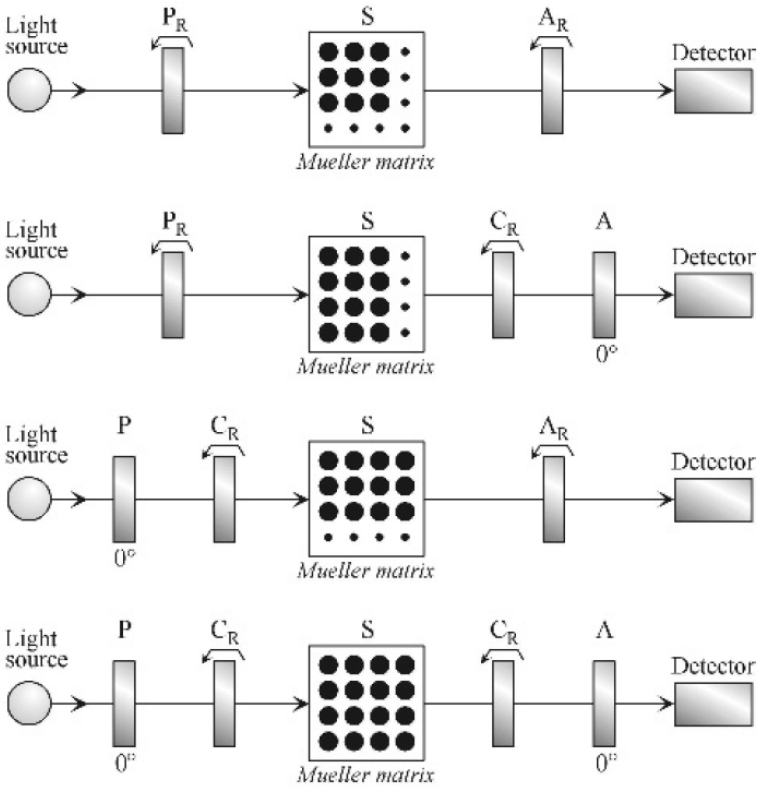

Figure 2.3: Optical configurations for rotating element ellipsometry. Subscripts R denotes the rotating element. Mueller matrix elements of the sample are denoted by dots, large dots represent measurable elements [1].

With respect to Eq. (2.23), for isotropic media, there is no cross-polarization (polarization conversion) and measurement of the change of polarization state is expressed in terms of the ellipsometric angles $\psi = \frac{|r_p|}{|r_s|}$ and $\Delta = \delta_p - \delta_s$.

$$\rho = \frac{r_p}{r_s} = \tan\psi \; e^{i\Delta} \tag{2.40}$$

It was already shown, that analysis of experimental Mueller matrix can lead to well-argumented description of the sample. However, we are often interested in the determination of the material properties of the sample itself. Optical material characteristics are usually given by dielectric tensor of the medium and it is treated in Chapter 5.2. At the end of this chapter, please, make note, that for isotropic, semi-infinite plane and perfectly smooth samples with no depolarization, analytical expression of dielectric function can be derived from Eq. (2.40) as the function of the

ellipsometric angles and the angle of incidence φ.

$$\varepsilon = \sin^2 \varphi \left[1 + \tan^2 \varphi \left(\frac{1-\rho}{1+\rho} \right)^2 \right] \tag{2.41}$$

This function can be mathematically calculated for any, generally anisotropic media with surface roughness, but it contains only negligible physically reliable information about sample. Therefore, we usually call this *pseudodielectric* function. However, even this distorted information (for example artificial absorptions when measuring transparent sample) can give us basic preview, overlook, and hints and tips, if our measurement is well-performed.

3 Optical activity of organic solutions

Optical activity is the abillity of a molecule to rotate the plane of linearly polarized light clockwise or counterclockwise. It has been known for a long time. Louis Pasteur is considered to be the pioneer in the field [26]. Optical activity is directly connected with the structure of chemical compounds and molecules. We focus on description of the origin of optical rotation in following section. The absolute goal of this chapter is to describe a method, how to measure optical activity using Mueller matrix ellipsometer.

3.1 The origin of optical activity

Optical activity of the molecule is conditioned by existence of the chirality (formerly chiral) centre. A chirality centre is an atom, that has 4 groups bonded to it in such a manner, that it has a nonsuperimposable mirror image. Usually, a chirality centre is easily recognizible, because each of the bonded groups are different and in most cases, the centre is located at carbon atom. We call this atom the chiral carbon. Of course, there may be exceptions, some molecules have its chirality centers in quaternary N, tetravalent P or sulfoxidic S [27].

If we arrange the molecule as shown in Fig. 3.1, we can construct its mirror image. If we rotate the mirror image of CHFClBr by 180°, and try to superimpose these two molecules, we can immediately see, that these molecules are different, despite the fact, that the chemical composition of the molecule is exactly the same. Thus, CHFClBr is a chiral molecule. If the molecule and its mirror image are exactly the same, this molecule is achiral. It can be done with ones hands. If one do the same procedure, one will find out, that ones hands are chiral. Therefore, we sometimes talk about the handeness of molecules.

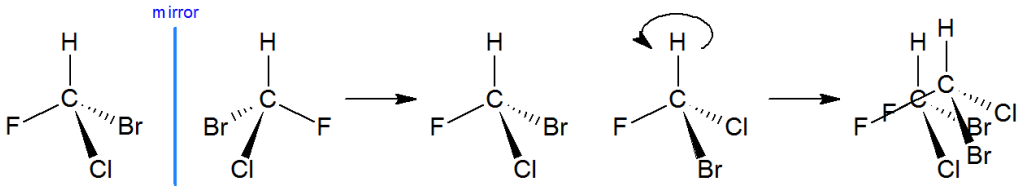

Figure 3.1: Prove of the chirality of the CHFClBr. By convention, solid lines represent bonds in the plane of the paper, bold lines are bonds that come out of the paper towards the reader, and dashed lines lie behind the paper. If we superimpose the CHFClBr molecule with its mirror image, we can see, that this molecule is surely chiral.

The most simple chiral molecule contains only one chirality centre. This molecule is logically always chiral. However, chiral molecules, which contains two or more chirality centers would not be *always* chiral. To understand this, we need to introduce formal nomenclatures. Right-handed and left-handed forms of molecules are most often described as D-molecule (from lat. *Dexter*) and L-molecule (from lat. *Laevus*). To be more precise, by further investigation it was shown,

that the D-form and L-form *may not* correspond to the side, in which the plane of the polarized light is rotated. To describe also this phenomenon, signs (+) for clockwise rotation and (−) for counterclockwise rotation were added as correction prefices before the molecule names. The letters D and L were left for the description of spatial structure of compounds. To avoid the confusion of using too many symbols, the most correctly we have to consider the configuration of chirality centers itself. With respect to the direction of the increase of bonded groups molar mass and their chemical priority, R (lat. rectus – right) and S (lat. sinister – left) chiral centres are distinguished. If there are as many R centers as S centers in the molecule, this molecule possesses no optical activity [28, 29], see Fig. 3.2.

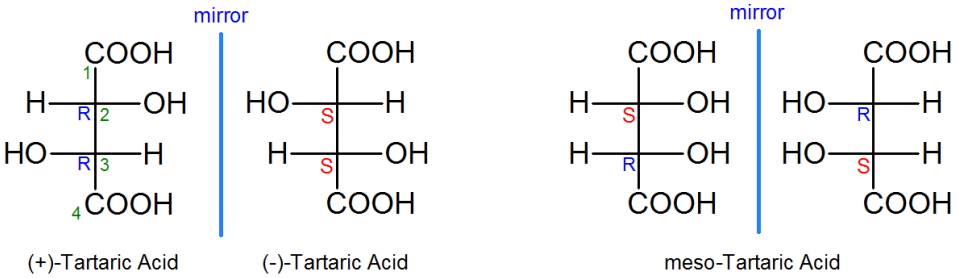

Figure 3.2: Geometrical interpretation of tartaric acid optical activity using R,S nomenclature. The chiral centers are carbons C2 and C3. (R,R) and (S,S)-tartaric acids are chiral, while (R,S) and (S,R) forms are achiral. Mixing equimolar ammount of (R,R) and (S,S)-tartaric acid solutions, we get achiral solution as well, known as *racemic mixture*.

Despite the fact RS system is formaly the most correct, in practice, *letter-(sign)-molecule* nomenclature was established for historical reason and simplicity.

3.2 Quantifying optical activity

Consider aqueous solution of sugar in a cuvette. When defined (angle of rotation α is known) linearly polarized light passes through the cuvette, its angle of polarization is changed. It is not difficult to think, that the amount of change is dependent on the path the light traveled – length of the cuvette l. Optical activity is caused by each chiral molecule in the solution, therefore the more molecules, the greater rotation. This is quantified as the concentration of the solution c. Concluding, the measured quantity is called specific rotation power for which an intuitive formula is defined [30]:

$$[\alpha]_{\lambda}^{T} = \frac{\alpha_{\text{obs}}}{lc} \tag{3.1}$$

Note, that the specific rotation is wavelength and temperature dependent. Subscript λ and superscript T specify the values at which the measurements are conducted.

There are slightly different construction types of spectrometers used for optical activity of solutions measurement, however the principle is the same and we present here the simplified description of such a polarimeter. It contains of the light source followed with monochromator.

The light passes through a polarizer into the tube (usually 10–30 cm long) filled with measured solution, in which the polarization azimuth is rotated. Using analyzer followed with the detector (photodiode), the specific rotatory power can be calculated according to the Malus's law [31].

This simple polarimeter works perfectly for every compound, due to the length of the tube, even low-concentrated solutions are well measurable. Unfortunatelly, only one wavelength of light can be measured at a time. Even modern polarimeters use Sodium lamps only, or Mercury lamps ocassionaly. Tabulated data from lots of experiments can be therefore found most often for the wavelength of 589 nm (D-line of Sodium lamp) and for 436, 546 and 579 nm, respectively.

Transmission ellipsometric measurement using RC2 Woollam Mueller matrix spectroscopic ellipsometer seems to be very convinient method, how to measure optical rotation of specific organic solutions without so strict spectral limitation. According to the rotation matrix from Eq. (2.15), corresponding Mueller matrix can be derived using Eq. (2.22):

$$\mathbf{M} = \frac{1}{2}\begin{pmatrix} 1 & 0 & 0 & 1 \\ 1 & 0 & 0 & -1 \\ 0 & 1 & 1 & 0 \\ 0 & i & -i & 1 \end{pmatrix} \begin{pmatrix} \cos^2\alpha & \sin\alpha\cos\alpha & \sin\alpha\cos\alpha & \sin^2\alpha \\ -\sin\alpha\cos\alpha & \cos^2\alpha & -\sin^2\alpha & \sin\alpha\cos\alpha \\ -\sin\alpha\cos\alpha & -\sin^2\alpha & \cos^2\alpha & \sin\alpha\cos\alpha \\ \sin^2\alpha & -\sin\alpha\cos\alpha & -\sin\alpha\cos\alpha & \cos^2\alpha \end{pmatrix} \begin{pmatrix} 1 & 1 & 0 & 0 \\ 0 & 0 & 1 & -i \\ 0 & 0 & 1 & i \\ 1 & -1 & 0 & 0 \end{pmatrix} \tag{3.2}$$

Performing the indicated calculation, the transmission Mueller matrix for opticaly active solutions is derived:

$$\mathbf{M} = \begin{pmatrix} 1 & 0 & 0 & 0 \\ 0 & \cos 2\alpha_{\mathrm{obs}} & \sin 2\alpha_{\mathrm{obs}} & 0 \\ 0 & -\sin 2\alpha_{\mathrm{obs}} & \cos 2\alpha_{\mathrm{obs}} & 0 \\ 0 & 0 & 0 & 1 \end{pmatrix} \tag{3.3}$$

3.3 Saccharides structure and optical activity

Every monosaccharide (monosugar) is formed by six-membered (pyranose) or five-membered (furanose) rings (as shows Fig. 3.3). Attaching these rings to each other in some manner will form disaccharide and so on. The rings exists in its α and β anomers. From now, we will talk about glucose (α/β-D-glucopyranose) and fructose (α/β-D-fructofuranose) only. The α anomer has hydroxyl group attached to C1 carbon with respect to C6 hydroxyl group antiperiplanary, while the β anomer is synperiplanar conformer. C1 atoms are chirality centers, therefore α and β tauntomers possesses different optical activity [32].

Melting five-membered β anomer, we get equilibrum solution of all other anomers, even the six-membered ones. For example, the equilibrum state of water solution of D-fructose is 70 % β-pyranose, 2 % α-pyranose, 23 % β-furanose, 5 % α-furanose and 0.7 % of open-chain form 4

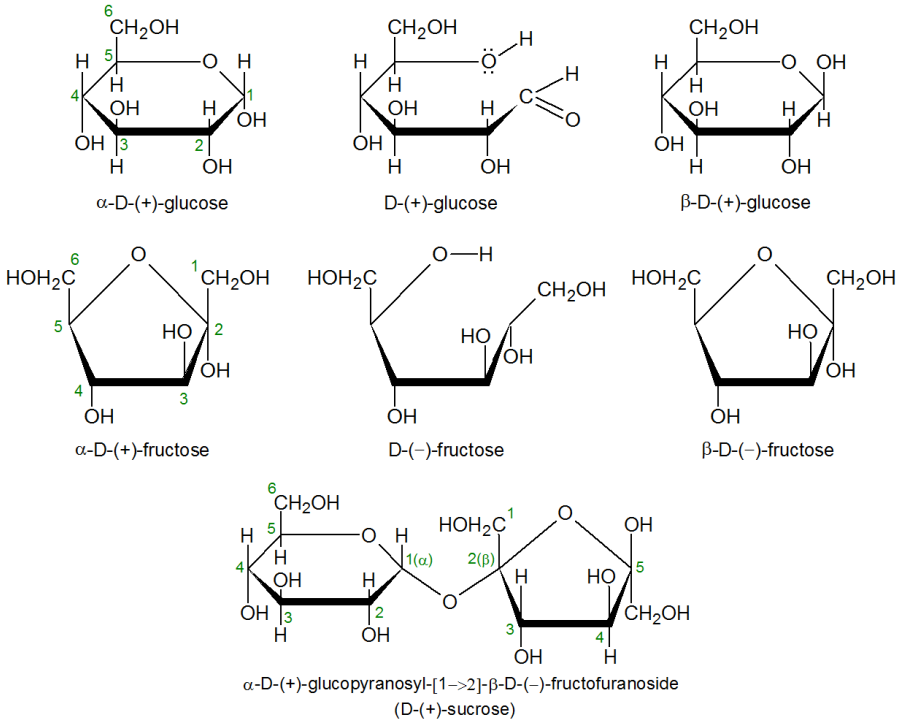

Figure 3.3: α, open-chain and β anomers of glucose and fructose. Pay attention about C1–C6 hydroxyl groups conformation. Disaccharide sucrose is formed, when we bond the six-membered ring of glucose with five-membered ring of fructose together via the oxygen atom.

[28]. This effect is called the mutarotation. Fortunately, when measuring optical activity of sugar solution in water at constant temperature, we obtain always the same values of specific rotatory powers, because the conversion is fast enough. The mutarotation is temperature dependent as well. For example, melting α-lactose at temperature higher then 93.5°C, the solution is composed only of β-anomers [33].

3.4 Hydrolysis of sucrose

Basic idea of the hydrolysis is that the water acts as an acid. When the molecule of water dissociates, it produces H^+ proton and OH^- anion. H^+ proton attacks the oxygen bond and therefore two different molecules of D-(+)-Glucose and L-(−)-Fructose are formed (Fig. 3.4). However, only a small amount of water molecules spontaneously dissociate and it causes very low efficiency of the hydrolysis. The reaction must be therefore catalyzed by surplus of achiral and non-reactive Brønsted acid (source of H^+ kations) and conducted under higher temperature or conducted and stirred for a long time. If we use Citric acid, which is commercialy available, it dissociates to hydrogen kations and citrate anions in the solution.

The oxygen bonding is the most vulnerable part of the molecule, so when exposed to protones, the decomposition occurs and D-(+)-Glucose and L-(−)-Fructose are formed. When there are

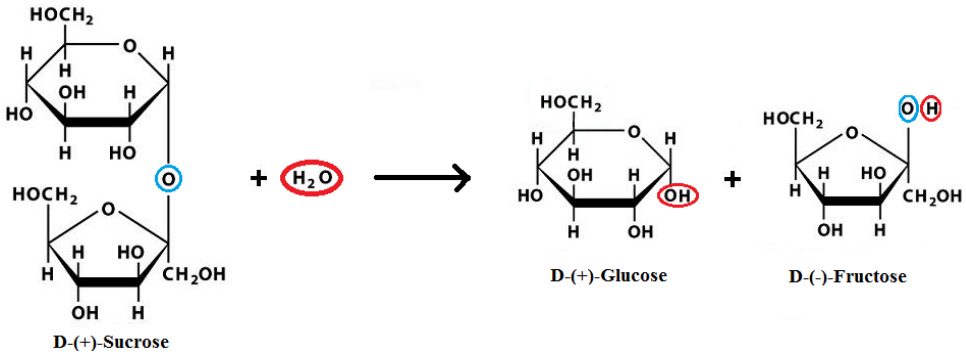

Figure 3.4: Mechanism of the hydrolysis of D-(+)-Sucrose.

no more D-(+)-Sucrose molecules left, citrate anions react with the remaining hydrogen kations forming the Citric acid again. The product is usually called *inverted sugar syrup*[2].

Now we can see, why the product of the hydrolysis of sucrose is called *Inverted Sugar*. $[\alpha]_{589}^{20}$ of D-(+)-Sucrose is dextrorotatory, while $[\alpha]_{589}^{20}$ of Inverted Sugar is laevorotatory. It is caused by the dominant effect of the D-(−)-Fructose specific rotation over D-(+)-Glucose specific rotation. Note, that $[\alpha]_{589}^{20}$ of the inverted Sugar is given by arithmetic mean of D-(+)-Glucose and L-(−)-Fructose specific rotations. Tabulated data of $[\alpha]_{589}^{20}$ for particular saccharides are summarized in Tab. 3.1.

Table 3.1: Specific rotations of sugars

Compound	$[\alpha]_{589}^{20}$ $[\circ \cdot \mathrm{ml} \cdot \mathrm{dm}^{-1} \cdot \mathrm{g}^{-1}]$ [34]
D-(+)-Glucose	52.70
D-(−)-Fructose	-92.00
D-(+)-Sucrose	66.37
Inverted Sugar	-19.65

[2]Hydrolysis of sucrose also takes place in nature. *Apis mellifera* uses enzyme called *invertase* when producing honey and it has the same effect on the sucrose, as it was decomposed acidically [35].

4 Optical activity ellipsometric measurements of the sugar solutions

This chapter's goal is to measure the optical activity of the differently concentrated sugar solutions ellipsometrically, show and discuss the precision of the method, and verify the correctness of the measurements and calculations on the sugar inversion reaction.

4.1 Preparation of the experiment

The optical rotation experiments were applied on sugar solutions of accurate concentrations. Lach:Ner analytical grade purity D-(+)-Glucose, D-(−)-Fructose, D-(+)-Sucrose and Dr. Oetker Citric acid were used. Saturated solutions were prepared according to the saturation curves given in Fig. 4.1. The $c = 0.25$ mol/l $\equiv 0.25$ M solutions were prepared using fundamental equation (4.1), that attaches the mass m of the substance needed for preparation of the solution of concentration c and volume V, and M represents the molar mass:

$$m = cMV \tag{4.1}$$

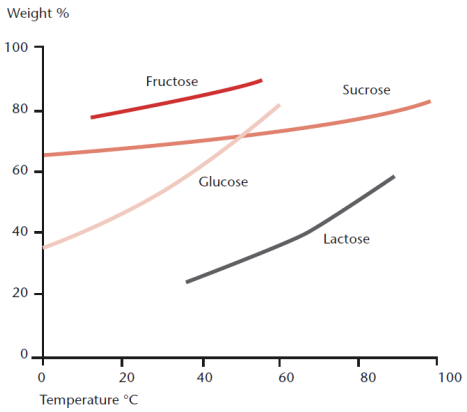

Figure 4.1: Saturation curves for different sugars [36]. Numerical data were obtained using Engauge Digitizer software [37].

Table 4.1: List of the prepared solutions:

Solution	M [g/mol]	m [g]
12 ml of saturated D-(+)-Glucose	180.16	12.9500
8 ml of saturated D-(−)-Fructose	180.16	32.2000
8 ml of saturated D-(+)-Sucrose	342.30	20.1700
100 ml of 0.25 M D-(+)-Glucose	180.16	4.5040
100 ml of 0.25 M D-(−)-Fructose	180.16	4.5040
100 ml of 0.25 M D-(+)-Sucrose	342.30	8.5575

4.2 Determining the ideal parameters of the measurements

All measurements were done using RC2 Woollam Spectroscopic Ellipsometer. Only glass cuvettes with the length of $l = 49.97$ mm were used. Each measurement was held for acquisition time of 80 s. Physically relevant results were obtained only within the wavelength range from 400 nm to 900 nm. Other wavelengths were dropped due to UV absorptions of the glass cuvette and IR excited vibrations of the organic molecules. Laboratory temperature was 23 °C.

First of all, 0.25 M solutions were measured. Figure 4.2 shows the Mueller matrix spectra for D-(+)-Glucose and D-(−)-Fructose solution, Fig. 4.3 shows the spectra for D-(+)-Sucrose solution.

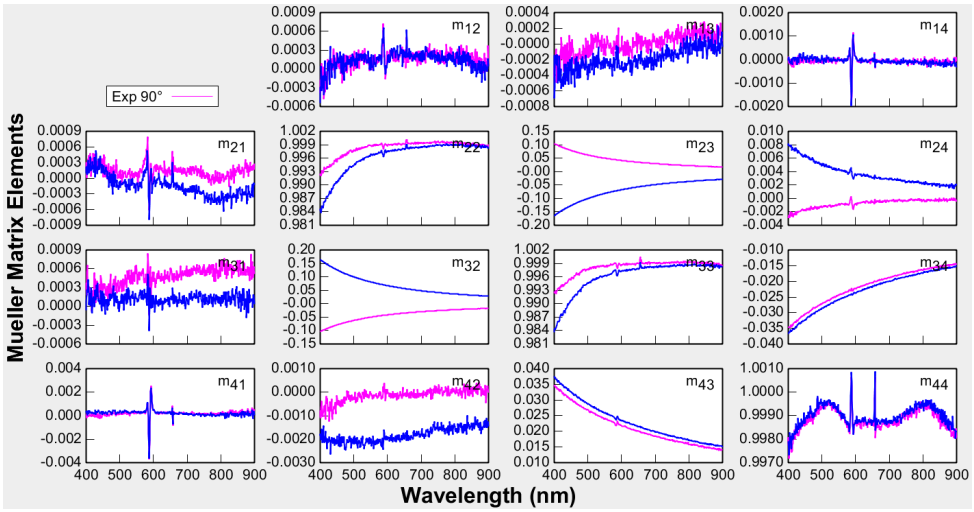

Figure 4.2: Mueller matrix of D-(+)-Glucose solution (purple lines) and D-(−)-Fructose solution (blue lines).

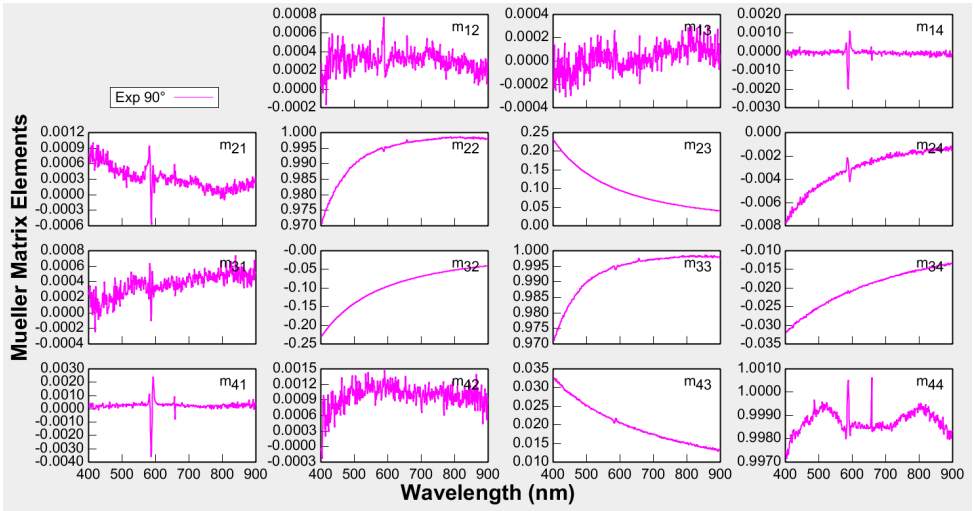

Figure 4.3: Mueller matrix of D-(+)-Sucrose solution.

Experimental matrices on Figs. 4.1 and 4.2 can be compared to theoretical model given by Eq. (3.3), however parasite effects within m_{24}, m_{34}, m_{44}, m_{42}, m_{43} elements are noticed.

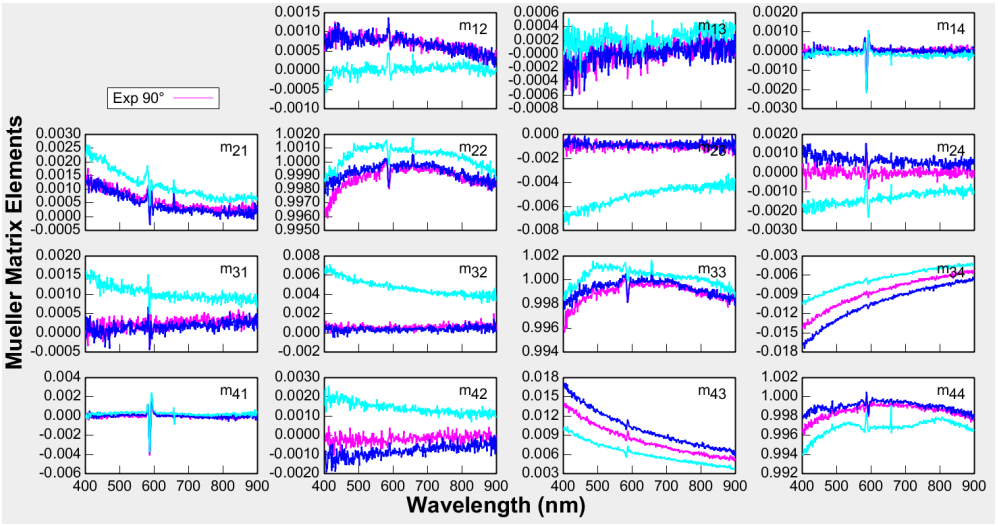

Figure 4.4: Mueller matrix spectra of empty cuvette (purple lines), cuvette filled with Distilled Water (blue lines) and cuvette filled with Citric Acid (cyan lines).

From the measurement of the empty cuvette, cuvette filled with distilled water, and cuvette filled with citric acid solution, two conclusions are obvious: First, the parasite effects are caused by the glass cuvette and they does not afflict the m_{22}, m_{23}, m_{32}, m_{33} elements. Second, it is clear, that distiiled water nor citric acid does not possess the optical activity. The deviations from the theoretical Mueller matrix model are negligibly small. Therefore, the optical activity measurements are not distorted by both possible cases.

From now, we will show only these Mueller matrix elements, that are in the field of the interest (m_{22}, m_{23}, m_{32}, m_{33} elements). Figures 4.5 and 4.6 compare the Mueller matrix spectra of D-(+)-Glucose, D-(−)-Fructose solutions and equimolar mixture of these solutions.

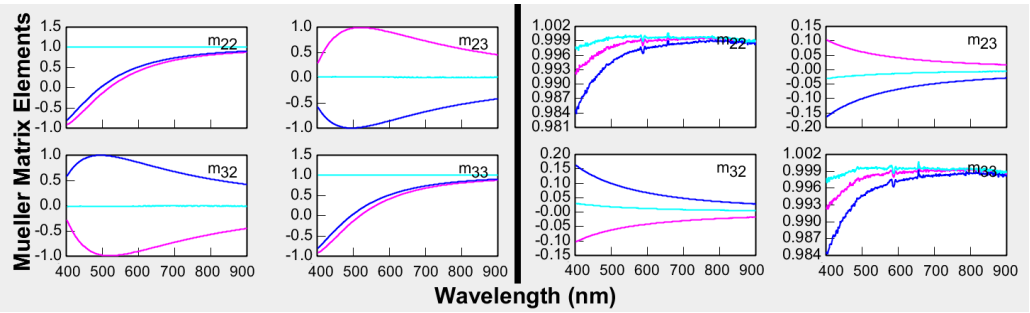

Figure 4.5: The m_{22}, m_{23}, m_{32}, m_{33} elements of two different experimental Mueller matrices. **Left:** Cyan line shows the experimental Mueller matrix of the equimolar solution of saturated D-(+)-Glucose and D-(−)-Fructose. **Right:** Equimolar (cyan) mixture of 0.25 M solutions.

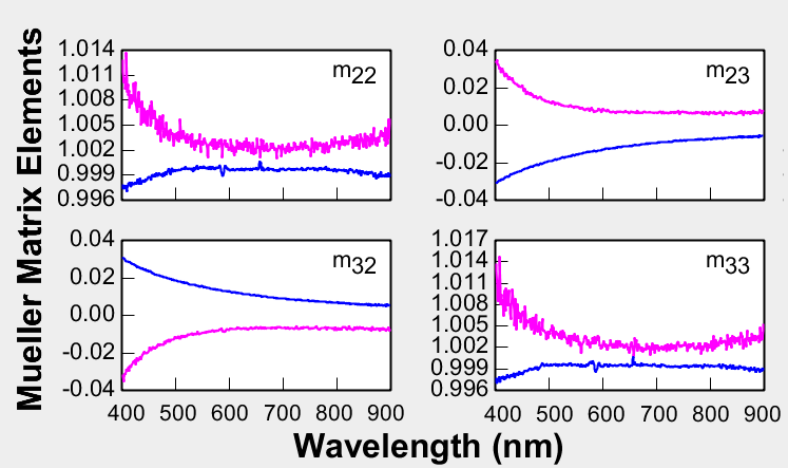

Figure 4.6: More detailed comparison of equimolar solutions. Mixture of saturated solution is drawn with the purple lines, 0.25 M mixtures are the blue lines.

It comes up, that saturated or very concentrated solutions are not very suitable for the optical activity measurements. The correct qualitative behaviour of the m_{23} and m_{32} elements are the blue ones, because sinus is a odd function, and we know, that equimolar solution of D-(+)-Glucose and D-(−)-Fructose is artificially prepared inverted sugar – we know the sign of the optical rotation. Morover, m_{22} and m_{33} elements show unphysical results in the case of the saturated mixtures. These deviations are the most probably caused due the preparation itself. The saccharides are generally extremely soluble, and it is difficult to dissolve such a quantity without the heating. Even very small evaporation from a sealed beaker may cause crucial concentration changes. The differency between the concentrations and mixing the solutions will result in very inappropriate results. Following measurements and calculations will be done using 0.25 M solutions only for mentioned reasons.

At the end of this section, we emphasize again the temperature dependence of optical activity and mutarotaion effects. The solutions must be measured after some time (2 hours) and after serious tempering.

4.3 Specific rotatory power calculations

The observed angles of optical activity – the values over which the plane of polarized light is rotated – can be calculated according to measured Mueller matrices from m_{22}, m_{23}, m_{32}, m_{33} elements. To avoid deviations caused by the noise from the measurements, the data were fitted with Cauchy dispersion model

$$n(\lambda) = A + \frac{B}{\lambda^2} + \frac{C}{\lambda^4}. \tag{4.2}$$

This model is sufficient enough, because we are fitting transparent, non-absorbing sample, dominantly over visible region of light. For the fitting and upcoming calculations, only m_{23} and m_{32} elements were chosen. We expect that the observed angles are very small, due to the nature

of the solutions. Therefore, m_{23} and m_{32} sine-dependent elements are the most sensitive, so the most accurate, as the sinus function has inflection point at the zero, while m_{22} and m_{33} cosine-dependent elements are less sensitive.

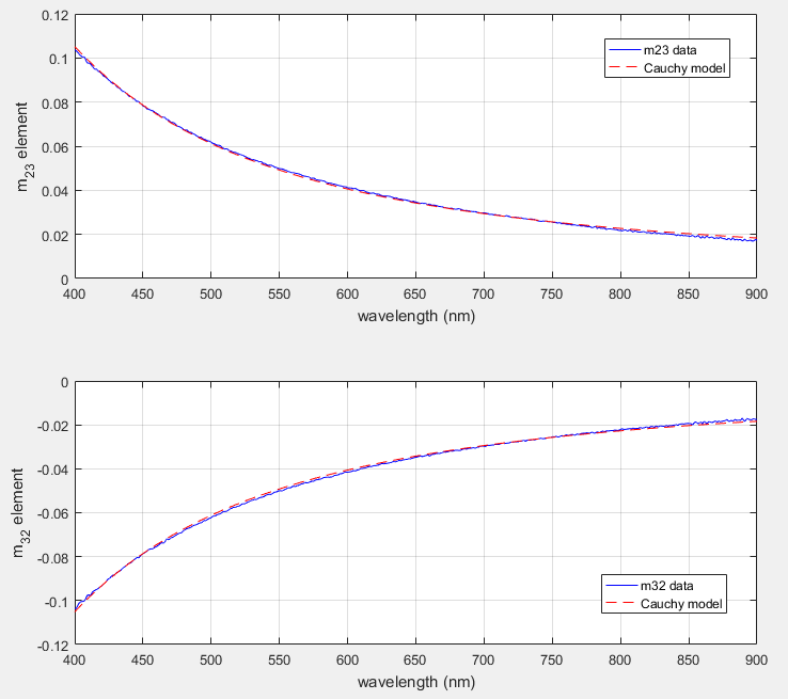

Figure 4.7: Experimental and modeled data of fitted elements of the experimental Mueller matrix for D-(+)-Glucose solution.

All other fitted dependences are at the same quality, therefore only one demonstrative Fig. 4.7 is shown. The observed optical activity for each solution were determined over measured spectra:

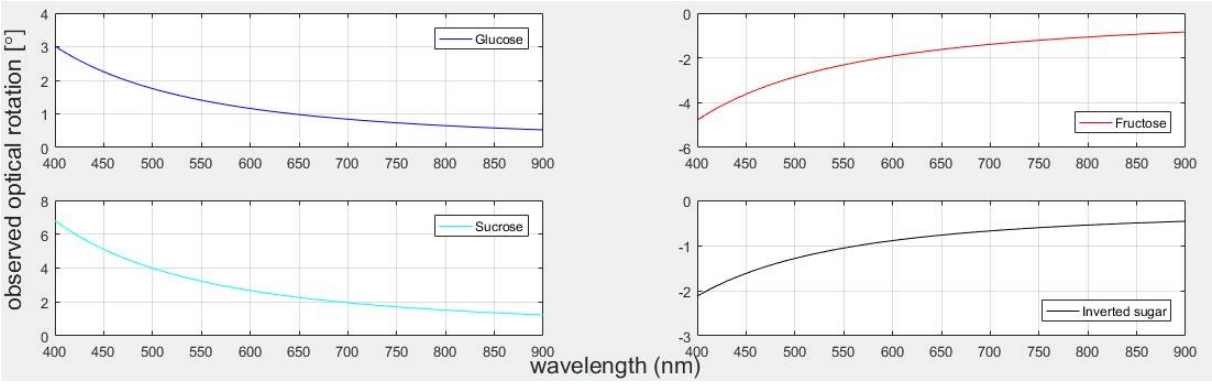

Figure 4.8: The observed optical activity of the sugar solutions. The angles show the deflection of the axis of linearly polarized light.

According to the angles shown in Fig. 4.8, the specific rotatory powers were calculated using Eq. (3.1). Figures 4.9 and 4.10 show the specific rotatory powers $[\alpha]_{\lambda}^{23}$ for monosaccharide solutions over spectral range of 400 to 900 nm and $[\alpha]_{\lambda}^{23}$ for hydrolyzed 0.25 M sucrose solution compared to artificially prepared inverted solution, respectivelly.

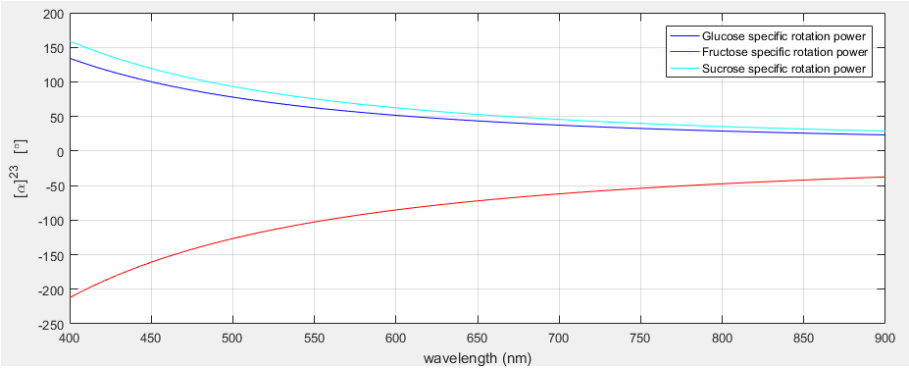

Figure 4.9: Specific rotatory powers $[\alpha]_{\lambda}^{23}$ of D-(+)-Glucose, D-(−)-Fructose and D-(+)-Sucrose. The qualitative shape of the functions are in good agreement with the assumption.

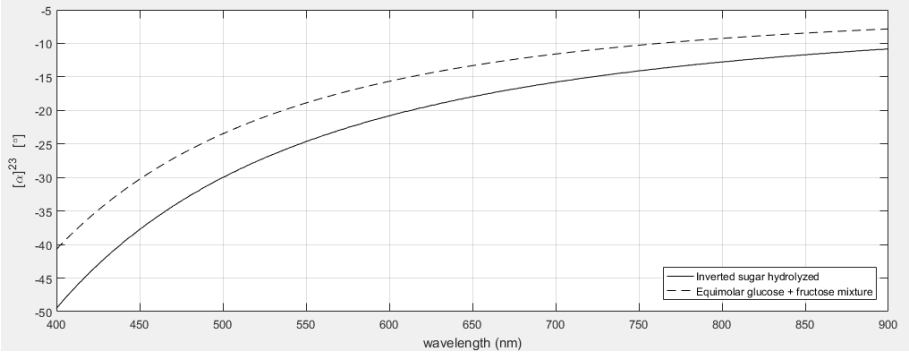

Figure 4.10: Specific rotatory powers $[\alpha]_{\lambda}^{23}$ of inverted sugar prepared by catalyzed hydrolysis of D-(+)-Sucrose compared to "artificially" prepared inverted sugar by simple mixture of 0.25 M solutions of D-(+)-Glucose and D-(−)-Fructose.

Using Lu-Chipman matrix decompostion given by Eq. (2.28), it is possible to achieve a pure retarder matrix, from which the observed optical activity, thus specific rotatory power of each solution can be calculated. Furthemore, diatennuation and depolarization effects of the experimental Mueller matrix can be determined as the possible source of the deviations.

For example, 0.25 M D-(+)-Sucrose experimental Muller matrix for 589 nm is decomposed as follows:

$$\begin{pmatrix} 1 & 0.0008 & 0.0002 & -0.0012 \\ -0.0003 & 0.9939 & -0.0987 & -0.0026 \\ 0.0000 & -0.0995 & 0.9939 & -0.0208 \\ -0.0025 & 0.0012 & 0.0217 & 1.0003 \end{pmatrix} = \begin{pmatrix} 1.0000 & 0.0000 & 0.0000 & 0.0000 \\ -0.0003 & 0.9987 & -0.0003 & 0.0004 \\ 0.0000 & -0.0003 & 0.9991 & 0.0003 \\ -0.0025 & 0.0004 & 0.0003 & 1.0005 \end{pmatrix} \times$$
$$\times \begin{pmatrix} 1.0000 & 0.0000 & 0.0000 & 0.0000 \\ -0.0008 & 0.9951 & 0.0992 & -0.0030 \\ -0.0001 & -0.0992 & 0.9948 & -0.0212 \\ 0.0016 & 0.0009 & 0.0213 & 0.9998 \end{pmatrix} \begin{pmatrix} 1.0000 & 0.0008 & 0.0002 & -0.0016 \\ 0.0008 & 1.0000 & 0.0000 & -0.0000 \\ 0.0002 & 0.0000 & 1.0000 & -0.0000 \\ -0.0016 & -0.0000 & 0.0000 & 1.0000 \end{pmatrix} \tag{4.3}$$

From the Lu-Chipman decomposition, the retardation, depolarizance and diattenuation parameters were calculated according to (2.32)–(2.34). The obtained parameters are summarized in Table 4.2.

Table 4.2: Qualitative parameters values for 589 nm of each sugar solution calculated from the matrices given by Lu-Chipman decomposition.

Solution	Retardance [○]	Depolarization [%]	Diattenuation [%]
D-(+)-Glucose	2.8082	0.0492	0.0492
D-(−)-Fructose	4.2738	0.0421	0.1375
D-(+)-Sucrose	5.8253	0.0543	0.1787
Inverted sugar artificial	1.5719	0.0449	0.0377
Inverted sugar hydrolyzed	3.7693	0.1160	0.1146

All calculated values were compared to commonly tabulated data for 589 nm [34].

Table 4.3: Comparison of calculated specific rotatory powers $[\alpha]_{589}^{23}$ from Cauchy model and Lu-Chipman decomposition with the tabulated data $[\alpha]_{589}^{20}$.

Solution	Cauchy	Lu-Chipman	Tabulated [34]
D-(+)-Glucose	53.79	62.44	52.70
D-(−)-Fructose	-88.67	-95.03	-92.00
D-(+)-Sucrose	65.02	68.09	66.37
Inverted sugar artificial	-17.68	-34.95	-19.65
Inverted sugar hydrolyzed	-22.39	-87.99	-19.65

From the Tab. 4.3, we see, that the calculations of specific rotatory powers directly from the measured spectra lead to the relatively meaningful values with respect to the tabulated data. However, certain deviations are observed.

Specific rotatory powers of monosaccharide solutions deviations are caused mainly, because of using ceramic weigh boats. D-(+)-Glucose and especially anhydrous D-(−)-Fructose is in the form of fine powder. The attractive electrostatic forces make impossible to put the whole weighted mass into the beaker. Even these small concentration changes significantly affect the rotation power of the solution. On the other side D-(+)-Sucrose is commonly supplied in the crystalline form, so the weighing error is not so significant. Despite the fact the beakers were sealed, the concentration was possibly increased due to the evaporation. The most significant discrepancies in the case of inverted sugars are caused both by weighing errors and additional concentration changes. For artificially prepared inverted sugar, these were caused by inaccurate prepapartion of both of the mother solutions, while for hydrolyzed sugars, we must take into account also strong evaporation during the hydrolysis and different melting points between glucose and fructose. It may happened, that glucose immediately started to decompose[3], therefore the optical activity of fructose was favorized.

Lu-Chipman decomposition showed, that all the solutions have only negligible depolarization and diatenuattion effect. However the values of specific rotatory power are not in very good match with the tabulated data. For monosaccharide solutions, they can serve as the indicative comfirmation of the measurement corectness, however for inverted sugar solutions, the data are unusable. More research on this field is needed, however we expect, that the order of the Mueller matrices decomposed according to the Lu-Chipman algorithm, does not reflect the reality (the sample), and one of the other decompositions would fit better. Moreover, it is convinient to say, that any Mueller matrix decomposition is unnecessarily strong tool for the data analysis, for which we have a simple theoretical model.

Note, that for each case, we still have to expect the mutarotation effect. The mutarotation rate constants are not tabulated for majority of the samples, so we don't know the reaction kinetics, therefore the optical activity affliction.

[3]This is other reason to use low concentrations of the solutions. If we hydrolyze saturated sucrose solutions, strong decomposition occurs just after reach of the boiling point. This process is commonly known as the caramelization.

5 Anisotropic crystals: Description and growth

All anisotropic structures, which are discussed in this bachelor thesis, have one more qualitative attribute, which si very specific for each of the structures – the periodicity. Let us take a look around the nature and let us forget the theory of the quantum electrodynamics for a while – despite the fact, that the probability amplitude of some event can be described by periodic function, on that scale, it is only the formalism, that is periodic [38]. Now, if we slightly zoom out, the periodicity can be found even on the atomic scale. Way, how the electrons fill the atomic shells, is periodical problem, and was predicted by Mendeleev in 1869. In 1980, the periodicity of the DNA was determined [39], and from the atoms of the DNA, it is only small step to describe the peridocity occuring in the whole living nature, even in the macroscopic meaning.

Everything, what does not meet the biological definition of the life, belongs to non-living nature. If we make an analysis (e.g. XRD) of some common example of some common average rock, we very likely find out, that our rock has no atomic periodicity. We call these structures to be *amorphous*. If we take a grain of kitchen salt and do the same procedure, we will see, that the atoms are grouped together in a cube. On the other side, XRD of the quartz gives us a Lauegram with a hexagon symmetry.

Sorting the crystals to the groups according to the specific rules is work of the special part of the geology – mineralogy, more precisely, descriptive mineralogy and descriptive crystallography. The adequate description of the crystals and their properties follows in the next paragraphs.

5.1 Descriptive crystallography

The crystal can be defined as the homogenous anisotropic discontinuum [40]. This is the most compact form of the definition, where the word *homogenous* is connected with the periodicity of the crystal, while the word *anisotropic* forces us to describe all physical and chemical properties of crystals as the function of the direction. Every *discontinuum* is spatially limited by its own surface and to ensure the existence of the crystal, it must satisfy the Euler's equation, valid for every convex polyhedron [41]

$$V + F = E + 2, \tag{5.1}$$

where V is number of vertices of the crystal, F number of its faces and E number of its edges.

The basic building unit of the crystals is the unit cell or the elementary cell. The elementary cell is clearly defined by 3 mutually linearly independent vectors called translation vectors and 3 angles between them. In some cases, these angles are called Euler angles. The origin of the vectors lyes at one of the cell point. Translating the whole cell along the direction of 1, 2 or along each of the vectors, the final crystal structure – with spatial limitation according to Eq. (5.1) – is formed and we call this structure crystal lattice.

The length of the vectors and values of the Euler angles directly affect the aspect ratio of the elementary cell, therefore they were chosen to be the fundamental parameters of the cell – lattice parameters. Using only these parameters, 7 crystallographic (crystal) systems are defined in Tab. 5.1.

Table 5.1: Lattice parameters of crystallographic systems

Symmetry	Euler angles	Crystal axes
Triclinic	$\alpha_e \neq \beta_e \neq \gamma_e \neq 90°$	$a_e < b_e < c_e$
Monoclinic	$\alpha_e = \gamma_e = 90°$, $\beta_e \neq 90°$	$a_e < b_e < c_e$
(Ortho)rhombic	$\alpha_e = \beta_e = \gamma_e = 90°$	$a_e < b_e < c_e$
Trigonal	$\alpha_e = \beta_e = 120°$, $\gamma_e = 90°$	$a_{e1} = a_{e2} = a_{e3} \neq c_e$
Tetragonal	$\alpha_e = \beta_e = \gamma_e = 90°$	$a_e = b_e \neq c_e$
Hexagonal	$\alpha_e = \beta_e = 120°$, $\gamma_e = 90°$	$a_{e1} = a_{e2} = a_{e3} \neq c_e$
Cubic	$\alpha_e = \beta_e = \gamma_e = 90°$	$a_e = b_e = c_e$

The crystallographic systems are based on the fact, that every crystal is symmetric in some manner. We define well-known symmetry elements: Symmetry axis (2-fold g_2, 3-fold g_3, 4-fold g_4, and 6-fold g_6), symmetry plane (m), inversion centre (C), and inversion symmetry axis (g_n). According to the geometry of the crystal, maximal element symmetry for each crystal system can be found and each crystal system belongs to the low, medium or high cathegory of symmetry [40].

Table 5.2: Maximal symmetry of crystal belonging to particular crystallographic system.

Order	Symmetry	Maximal crystallographic symmetry
low	Triclinic	C
low	Monoclinic	g_2, m, C
low	(Ortho)rhombic	$3g_2$, 3m, C
medium	Trigonal	g_3, $3g_2$, 3m, C
medium	Tetragonal	g_4, $4g_2$, 5m, C
medium	Hexagonal	g_6, $6g_2$, 7m, C
high	Cubic	$3g_4$, $4g_3$, $6g_2$, 9m, C

In crystallography, it is crucial to define the habit (external shape) of the crystal. We are not going to describe all possible external shapes, but for practical reasons, we define the basic shapes of the crystal planes – crystal forms. Every crystal habit is some particular combination of these then [40].

- **Pedion** – formed by one, unique plane.
- **Pinacoid** – two equivalent parallel and opposite faces symmetrical to 2-fold axis, symmetry plane or inversion centre.
- **Sfenoid** – two nonparallel equivalent faces symmetrical to 2-fold symmetry axis.

- **Doma** – two nonparallel equivalent and opposite faces symmetrical to symmetry plane or 2-fold axis *and* symmetry plane.
- **Prism** – three or more equivalent planes intersecting in parallel edges.
- **Pyramid** – three or more equivalent planes intersecting in common apex.

Now, we have defined crystal symmetries (microscopic parameters) and forms (macroscopic parameters). All possible combinations of microscopic parameters form 230 space groups, without translation components 32 point groups (Tab. 5.3). Every crystal is fully described with its point group and habit [40, 42].

Table 5.3: 32 symmetry classes. Every crystal belongs to one of these.

Crystal system	Hermann-Maugin symbol (point group)	Class (dominant habit)
Triclinic	1	Pedial
	$\bar{1}$	Pinacoidal
Monoclinic	2	Sphenoidal
	m	Domatic
	$2/m$	Prismatic
Orthorombic	222	Rhombic-Disphenoidal
	$mm2$	Rhombic-Pyramidal
	$2/m\ 2/m\ 2/m\ (mmm)$	Rhombic-Dipyramidal
Tetragonal	4	Tetragonal-Pyramidal
	$\bar{4}$	Tetragonal-Disphenoidal
	$4/m$	Tetragonal-Dipyramidal
	422	Tetragonal-Trapezohedral
	$4mm$	Ditetragonal-Pyramidal
	$\bar{4}2m$	Tetragonal-Scalenohedral
	$4/m\ 2/m\ 2/m\ (4/mmm)$	Ditetragonal-Dipyramidal
Trigonal	3	Trigonal-Pyramidal
	$\bar{3}$	Rhombohedral
	32	Trigonal-Trapezohedral
	$3m$	Ditrigonal-Pyramidal
	$\bar{3}\ 2/m\ (\bar{3}m)$	Hexagonal-Scalenohedral
Hexagonal	6	Hexagonal-Pyramidal
	$\bar{6}$	Trigonal-Dipyramidal
	$6/m$	Hexagonal-Dipyramidal
	622	Hexagonal-Trapezohedral
	$6mm$	Dihexagonal-Pyramidal
	$\bar{6}m2$	Ditrigonal-Dipyramidal
	$6/m\ 2/m\ 2/m\ (6/mmm)$	Dihexagonal-Dipyramidal
Cubic	23	Tetaroidal
	$2/m\bar{3}$	Diploidal
	432	Gyroidal
	$\bar{4}3m$	Hextetrahedral
	$4/m\ \bar{3}\ 2/m$	Hexoctahedral

5.2 Crystallographic-optical symmetry analogy

Crystallographic symmetry elements can be mathematically described using transformation matrix formalism. Every crystallographic symmetry operation can be understood as an operation that transforms a set of points or a point on itself. According to the Neumann's principle, if any crystal is invariant to certain symmetry operations according to the crystal symmetry it belongs to, any physical property must also be invariant with respect to these symmetry

operations [43].

If we take into account Eq. (2.9), we are looking for the derivation of the dielectric tensor shape describing any crystal of any symmetry. Derivation of particular dielectric tensor describing 422 tetragonal crystal is shown as an example: We apply rotation matrix of g_4 axis along c_e on the most general form of the dielectric tensor $\hat{\varepsilon}'$:

$$\hat{\varepsilon}' = \mathbf{R}(90°)\,\hat{\varepsilon}\,\mathbf{R}(90°)^{-1} = \begin{pmatrix} 0 & -1 & 0 \\ 1 & 0 & 0 \\ 0 & 0 & 1 \end{pmatrix} \begin{pmatrix} \varepsilon_{11} & \varepsilon_{12} & \varepsilon_{13} \\ \varepsilon_{21} & \varepsilon_{22} & \varepsilon_{23} \\ \varepsilon_{31} & \varepsilon_{32} & \varepsilon_{33} \end{pmatrix} \begin{pmatrix} 0 & 1 & 0 \\ -1 & 0 & 0 \\ 0 & 0 & 1 \end{pmatrix} = \begin{pmatrix} \varepsilon_{22} & -\varepsilon_{21} & -\varepsilon_{23} \\ -\varepsilon_{12} & \varepsilon_{11} & \varepsilon_{13} \\ -\varepsilon_{32} & \varepsilon_{31} & \varepsilon_{33} \end{pmatrix} \tag{5.2}$$

Now, the elements of the general expression of dielectric tensor can be compared with elements of the resulting tensor, which leads to:

$$\left.\begin{aligned} &\varepsilon_{11} = \varepsilon_{22} \\ &\varepsilon_{21} = -\varepsilon_{12} \Rightarrow \varepsilon_{21} = \varepsilon_{12} = 0 \\ &\varepsilon_{13} = \varepsilon_{23} \\ &\varepsilon_{13} = -\varepsilon_{23} \Rightarrow \varepsilon_{13} = \varepsilon_{23} = 0 \end{aligned}\right\} \begin{pmatrix} \varepsilon_{11} & 0 & 0 \\ 0 & \varepsilon_{11} & 0 \\ 0 & 0 & \varepsilon_{33} \end{pmatrix} \equiv \begin{pmatrix} \varepsilon_o & 0 & 0 \\ 0 & \varepsilon_o & 0 \\ 0 & 0 & \varepsilon_e \end{pmatrix} \tag{5.3}$$

Dielectric tensor forms derivation for other symmetry groups is analogical. Notice the analogy between tensor forms in Tab. 5.4 and lattice parameters in Tab. 5.1.

Table 5.4: Dielectric tensors forms for each crystal symmetry.

Symmetry	Dielectric tensor	Symmetry	Dielectric tensor
Triclinic	$\begin{pmatrix} \varepsilon_{11} & \varepsilon_{12} & \varepsilon_{13} \\ \varepsilon_{21} & \varepsilon_{22} & \varepsilon_{23} \\ \varepsilon_{31} & \varepsilon_{32} & \varepsilon_{33} \end{pmatrix}$	Uniaxial positive $\varepsilon_o < \varepsilon_e$	$\begin{pmatrix} \varepsilon_o & 0 & 0 \\ 0 & \varepsilon_o & 0 \\ 0 & 0 & \varepsilon_e \end{pmatrix}$
Monoclinic	$\begin{pmatrix} \varepsilon_{11} & \varepsilon_{12} & 0 \\ \varepsilon_{21} & \varepsilon_{22} & 0 \\ 0 & 0 & \varepsilon_{33} \end{pmatrix}$	Uniaxial negative $\varepsilon_o > \varepsilon_e$	$\begin{pmatrix} \varepsilon_o & 0 & 0 \\ 0 & \varepsilon_o & 0 \\ 0 & 0 & \varepsilon_e \end{pmatrix}$
Orthorombic	$\begin{pmatrix} \varepsilon_1 & 0 & 0 \\ 0 & \varepsilon_2 & 0 \\ 0 & 0 & \varepsilon_3 \end{pmatrix}$	Cubic	$\varepsilon \begin{pmatrix} 1 & 0 & 0 \\ 0 & 1 & 0 \\ 0 & 0 & 1 \end{pmatrix}$

From crystallographic point of view, the symmetries are divided into the orders. Optically speaking, we define isotropic, uniaxial and biaxial crystals, with respect to how many optic axes crystals exhibit. Because $n = \sqrt{\varepsilon}$, it is obvious, that the light travels with different speed along each crystallographic axis, since $n = v_c/v$. The effect caused by this phenomena is called the birefrigence. However, there are 1 or 2 directions called optical axes, along which the light travels with constant speed. According to the number of the optical axis, we define uniaxial and biaxial crystals. The optical axis lye on the intersection of the ellipsoids describing the relative value of wave vector along the crystal axes. In the case of uniaxial crystals, the intersections is between ellipsoid and sphere.

5.3 Wave equation solution for anisotropic media

Maxwell's equations for anisotropic media with no charges and no currents:

$$\boldsymbol{k} \times \boldsymbol{H} + \omega\varepsilon_0\hat{\varepsilon}\boldsymbol{E} = 0 \tag{5.4}$$

$$\boldsymbol{k} \times \boldsymbol{E} - \omega\mu_0\boldsymbol{H} = 0 \tag{5.5}$$

Assuming $\mu_\mathrm{r} = 1$, the wave equation for the anisotropic media can be derived substituting (5.4) into (5.5).

$$(\boldsymbol{k} \cdot \boldsymbol{E_0}) \cdot \boldsymbol{k} - \boldsymbol{k^2} \cdot \boldsymbol{E_0} + k_0^2\hat{\varepsilon}\boldsymbol{E_0} \tag{5.6}$$

Assuming $\boldsymbol{k} = k_\mathrm{x}\hat{\boldsymbol{x}} + k_\mathrm{y}\hat{\boldsymbol{y}} + k_\mathrm{z}\hat{\boldsymbol{z}} \equiv k_0\left(N_\mathrm{x}\hat{\boldsymbol{x}} + N_\mathrm{y}\hat{\boldsymbol{y}} + N_\mathrm{z}\hat{\boldsymbol{z}}\right)$ and rewriting the wave equation into the matrix form leads to:

$$\begin{pmatrix} \varepsilon_{11} - N_y^2 - N_z^2 & \varepsilon_{12} & \varepsilon_{13} \\ \varepsilon_{21} & \varepsilon_{22} - N_z^2 & \varepsilon_{23} - N_yN_z \\ \varepsilon_{31} & \varepsilon_{32} + N_zN_y & \varepsilon_{33} - N_y^2 \end{pmatrix} \begin{pmatrix} E_{0x} \\ E_{0y} \\ E_{0z} \end{pmatrix} = 0 \tag{5.7}$$

Equation (5.7) has nontrivial solution for N_z if and only if determinant of 3×3 matrix is equal zero. This leads to the solution in the form of the quartic function:

$$aN_z^4 + bN_z^3 + cN_z^2 + dN_z + e = 0 \begin{cases} a = \varepsilon_{33} \\ b = 2\varepsilon_{23}N_y \\ c = \varepsilon_{13}^2 + \varepsilon_{23}^2 - \varepsilon_{33}(\varepsilon_{11} + \varepsilon_{22}) + (\varepsilon_{22} + \varepsilon_{33})N_y^2 \\ d = (2\varepsilon_{12}\varepsilon_{13} - 2\varepsilon_{11}\varepsilon_{23})N_y + (\varepsilon_{23}^2 + \varepsilon_{23}) \\ e = 2\varepsilon_{12}\varepsilon_{13}\varepsilon_{23} - \varepsilon_{13}^2\varepsilon_{22} - \varepsilon_{12}^2\varepsilon_{33} + \\ +(\varepsilon_{23}^2 + \varepsilon_{12}^2 - \varepsilon_{22}\varepsilon_{33} - \varepsilon_{11}\varepsilon_{21})N_y^2 + \varepsilon_{22}N_y^4 \\ N_y = n_0 \sin\theta \end{cases} \tag{5.8}$$

Solving the equation for N_z will result in calculating the propagating eigenmodes in triclinic media with respect to the orientation of crystal.

The equation reduces as the symmetry of the crystal increases. For orthorombic case, $\hat{x}$, $\hat{y}$-perpendicular to the incidence plane propagating eigenmodes can be derived:

$$N_{z1,2} = \pm\sqrt{\varepsilon_{11} - N_y^2} \tag{5.9}$$

$$N_{z3,4} = \pm\sqrt{\frac{\varepsilon_{22}}{\varepsilon_{33}}(\varepsilon_{33} - N_y^2)} \tag{5.10}$$

$$\tag{5.11}$$

For uniaxial crystals:

$$N_{z1,2} = \pm\sqrt{\varepsilon_o - N_y^2} \tag{5.12}$$

$$N_{z3,4} = \pm\sqrt{\frac{\varepsilon_o}{\varepsilon_e}(\varepsilon_e - N_y^2)} \tag{5.13}$$

Here, ε_o and ε_e denotes the ordinary and the extraordinary dielectric constant, respectivelly. Using Yeh's matrix formalism [44], propagating eigenmodes can be used for the Fresnel coefficients calculations. For example, reflection coefficients of uniaxial crystals can be calculated analytically in terms of ordinary and extraordinary refraction indexes n_o and n_e, respectivelly and angle of incidence φ.

$$r_{ss} = \frac{\cos\varphi - \sqrt{n_o^2 - \sin^2\varphi}}{\cos\varphi + \sqrt{n_o^2 - \sin^2\varphi}} \tag{5.14}$$

$$r_{sp} = 0 \tag{5.15}$$

$$r_{ps} = 0 \tag{5.16}$$

$$r_{pp} = \frac{n_e^2 - \sin^2\varphi - \frac{n_o^3}{n_e}\cos\varphi\sqrt{n_o^2 - \sin^2\varphi}}{n_o^2 - \sin^2\varphi + n_o n_e\cos\varphi\sqrt{n_e^2 - \sin^2\varphi}} \tag{5.17}$$

5.4 Crystallization by slow evaporation, cooling and seeding method

Crystal growth method in industry are mainly based on the crystallization from high temperature solutions – from melts. Good example is Czochralski process [45] or zonal melting method [46]. Very high quality monocrystals without defects[4] are produced and usually used in semiconductor industry, which requires extreme purity of the materials.

We will focus on the slow evaporation and cooling method. Both methods are based on the crystallization from low temperature solution, e.g. water or also commonly used are alcohols

[4] Actually, absolutely perfect monocrystal is only hypothetical structure. Even the most perfect monocrystals (whiskers) have at least 2 crystallographic defects – its own surface and screw dislocation along which the crystal grows, usually called the growth spiral.

and aliphatic hydrocarbons. Both methods require very accurate preparation of the mother solution. If we crystallize a single compound monocrystal, a simple solubility curve of appropriate compound is needed, however for cocrystal growth, ternary, quaternary and higher dimension diagrams are used. The saturation curve (e.g. Fig. 6.1 in the following Chapter) is concentration on temperature dependance and represents saturated state of the system. The area below the curve is the undersaturated region, no nucleation occurs, crystal dissolves; area above the curve is the supersaturated region, the spontaneous nucleation is observed.

To achieve the spontaneous nucleation, the equilibrum must be shifted. If we let the solution to slightly evaporate, concentration of analyte increases. The solution is getting slightly oversaturated and nucleation occurs. The same effect has lowering the temperature of the prepared solution. As the temperature decreases, the ammount of analyte needed for the preparation of saturated solution decreases as well, therefore we obtain the supersaturated solution again, depending on the temperature difference, and the nucleus may form.

The best controlled method is the seeding method. The goal is to keep the concentration just on the saturated level and insert the seed crystal. The thermodynamic equilibrum shifts according to the Le Chatelier's principle and the seed crystal grows. The growth rate can be controlled by changing the temperature or allowing the solution to evaporate. Therefore, most commonly, the combination of all three methods is used.

In following sections, thermodynamics and kinetics of most important processes is discussed.

5.5 Temperature and concentration dependences of nucleation as the effects on the solubility curve shape

The crystal preparation in this thesis is based on the slow evaporation method from the water solution. The growth of the crystal is initiated by the embryo formation and it can be described from a thermodynamic point of view. Let's consider a thermodynamic system consisting only of solid and liquid phase. We does not include the existence of inpurities or presence of the beaker. Therefore, we are talking about homogenous nucleation.

At the temperatures lower then the melting point of the solid phase, the thermodynamic potential of solid phase $G_{(s)}$ becomes lower, then the potential of liquid phase $G_{(l)}$. When the temperature is lowered below the melting temperature, the melt becomes unstable and solidification occurs.

When a spherical nucleus is formed, its radius r is very small, therefore we can write:

$$\left|\frac{4}{3}\pi r^3 \Delta G_{\mathrm{V}}\right| < 4\pi r^2 \sigma, \tag{5.18}$$

where ΔG_{V} denotes change of the volume Gibbs energy and σ the surface tension. The total Gibbs energy ΔG is in the form,

$$\Delta G = 4\pi r^2 \sigma - \frac{4}{3}\pi r^3 \Delta G_{\mathrm{V}}. \tag{5.19}$$

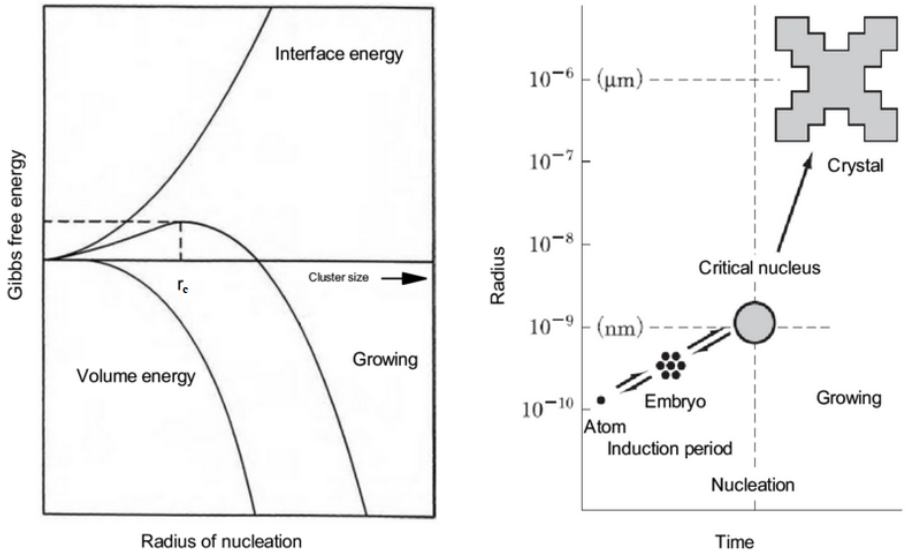

Figure 5.1: **Left:** The Gibbs energy bilantion. The nucleation is energetically disadvantageous, so the crystallization occurs, once the embryo reaches the critical radius. **Right:** Basic scheme of the nucleation and crystal growth [47]

.

The maximum of the curve (Fig. 5.1) given by equation (5.19) can be determined:

$$\frac{\mathrm{d}\,(\Delta G)}{\mathrm{d}r} = 0 \tag{5.20}$$

Solving (5.20), critical radius r_c of the nucleus is given by condition:

$$r_\mathrm{c} = \frac{2\sigma}{\Delta G_\mathrm{V}} \tag{5.21}$$

Substituting (5.21) into (5.19), ΔG_max is given:

$$\Delta G_\mathrm{max} = \frac{16\pi}{3}\frac{\sigma^3}{\Delta G_\mathrm{V}} \tag{5.22}$$

Now, with ΔG_max known, we can derive the dependence on the overcooling $\Delta T = T_\mathrm{m} - T$, where T_m is the melting temperature and T the temperature of surroundings. Because the volume V, pressure p, temperature T and entropy S are the state functions, the Gibbs energy can be rewritten dependent on these [48].

$$\mathrm{d}G = V\mathrm{d}p - S\mathrm{d}T \tag{5.23}$$

For slow evaporation crystallization method under normal condition, we can consider the isobaric process, therefore

$$\mathrm{d}G = -S\mathrm{d}T. \tag{5.24}$$

From (5.19), we know, that the change of the volume Gibbs energy is given by the Gibbs energy of the solid phase and the liquid phase, respectively, as follows: $\Delta G_{\mathrm{V}} = G_{(s)} - G_{(l)}$, therefore

$$\mathrm{d}\left(G_{(s)} - G_{(l)}\right) = -\left(S_{(s)} - S_{(l)}\right)\mathrm{d}T. \tag{5.25}$$

Integrating (5.24), we get the temperature dependence in terms of enthalpy H and T_{m}:

$$\Delta G_{\mathrm{V}} = \int_{T}^{T_{\mathrm{m}}} \Delta S \mathrm{d}T = \int_{T}^{T_{\mathrm{m}}} \frac{\Delta H}{T_{\mathrm{m}}}\mathrm{d}T = \frac{\Delta H}{T_{\mathrm{m}}}\Delta T \tag{5.26}$$

Now, we substitute (5.26) into (5.22) and all constants include into single constant K,

$$\Delta G_{\max} = \frac{16\pi}{3}\frac{\sigma^3}{(\Delta H)^2}\frac{T_{\mathrm{m}}^2}{(\Delta T)^2} = \frac{K}{(\Delta T)^2}. \tag{5.27}$$

To show the concentration effect, we need to define the chemical potential of i-th element μ_{i} with respect to the change of the ammount of substance $\mathrm{d}n$ [49].

$$\mu_{\mathrm{i}} = \left(\frac{\partial G}{\partial n_i}\right)_{T,p,n_j \neq n_i} \tag{5.28}$$

For isothermic and isobaric change of the Gibbs energy of N-element system applies:

$$\Delta G_{\max} = \sum_{i=1}^{N}\left(\frac{\Delta G}{\Delta n_i}\right)_{T,p,n_j \neq n_i} \tag{5.29}$$

For further discussion, let be (5.27) and (5.29) equal:

$$\sum_{i=1}^{N}\left(\frac{\Delta G}{\Delta n_i}\right)_{T,p,n_j \neq n_i} = \frac{K}{(\Delta T)^2} \tag{5.30}$$

From (5.27), it is obvious, that the lower the temperature of solution is, the higher energy for embryo formation is required. From Eq. (5.30), we further see, that the temperature is concentration dependent. However, this change of the Gibbs energy with concentration of the solid phase can be either positive or negative. Depending on the energy change, the saturation curves possesses positive or negative slope. In practice, most of chemical compounds has positive slope of the saturatuon curve (for example Fig. 6.1) – the higher concentration, the lower temperature for crystallization is needed. Discussed equations above describe homogenous nucleation. Description of heterogenous nucleation is exactly the same, but we must come out from Eq. (5.19) as a function of angle between the interface (beaker, seed crystal) and liquid-solid surface tension component ξ.

$$\Delta G = \left(4\pi r^2\sigma - \frac{4}{3}\pi r^3 \Delta G_{\mathrm{V}}\right) f(\xi) \tag{5.31}$$

5.6 Effect of impurities on the crystal growth

The purity of the mother solution is reasonable requirement, when growing crystals. For this purpose, the analytical grade chemical compounds are often repeatedly recrystallized to achieve the most pure substance as possible. In fact, it is only barely possible to get perfectly pure solution in common chemical laboratory. Therefore, impurities effect on the crystallization process was studied.

The most simple model describing the impurities kinectics is based on well-known Langmuir adsorption isotherm [50]. It expects the physisorption or chemisorption of impurity particles layer by layer on the surface of crystallizing solvent. The ammount of sorbed particles directly affects the crystal growth rate and ratio between step velocity of the pure R_p and in the presence of impurity R_im [51].

$$\frac{R_\mathrm{im}}{R_\mathrm{p}} = 1 - \Omega \tag{5.32}$$

The growth is stopped, when the Langmuir factor $\Omega = 1$, however, complete surface coverage differs also with shape, size and orientation of the impurity particles. Therefore, effectivness factor (weight parameter of the function Ω) ζ is included.

$$\frac{R_\mathrm{im}}{R_\mathrm{p}} = 1 - \zeta\Omega \tag{5.33}$$

The factor Ω is expressed in terms of the impurities concentration in the solution – Langmuir isotherm, where K is the Langmuir absorption isotherm constant, and c_im the concentration of the impurities.

$$\frac{R_\mathrm{im}}{R_\mathrm{p}} = 1 - \zeta\frac{Kc_\mathrm{im}}{1 + Kc_\mathrm{im}} \tag{5.34}$$

Relative step velocity is proportional to the relative face growth rate of the crystal:

$$\frac{G_\mathrm{im}}{G_\mathrm{p}} = 1 - \zeta\frac{Kc_\mathrm{im}}{1 + Kc_\mathrm{im}} \tag{5.35}$$

To determine the influence of ζ, geometry of the problem must be discussed. Kindhearted reader will find detailed derivation in [52], we simply state, that the derivation is based on the relation of the impurity molecule geometry (r_c) and separation of active sites available for adsorption (L) with impurity molecule spacing ratio on the surface.

$$\frac{G_\mathrm{im}}{G_\mathrm{p}} = 1 - \frac{r_\mathrm{c}}{L}\frac{Kc_\mathrm{im}}{1 + Kc_\mathrm{im}} \tag{5.36}$$

Using Eq. (5.21), the Gibbs-Helmholtz equation and substituting into (5.36), we get,

$$\frac{G_\mathrm{im}}{G_\mathrm{p}} = 1 - \frac{\sigma S_c}{kT\Xi L}\frac{Kc_\mathrm{im}}{1 + Kc_\mathrm{im}}, \tag{5.37}$$

where S_c is the are occupied by one crystallizing molecule, and Ξ the relative supersaturation.

Finally, we can see, that ζ decreases as the supersaturation increases. It is crucial statement for the crystal growth, because we are working with supersaturated solutions only. Martins et. al. proposed competitive adsorption model [53] as an extension of just described model, where G_{im}/G_p ratio is morover function of affinity. For sucrose, $\zeta = 0.9$, therefore the kinetics impurity effect is low. Please, make note, that the presence of impurities affects the principle of the nucleation, because with respect to the affinity of impuritiy particle to dissolved compound, the system exhibits homogenous or heterogenous nucleation.

6 Growth of sugar, butanedioic acid and its derivatives monocrystals

Hydroxyl group substituited butandeioic acids and saccharides monocrystals are structures forming hydrogen bonds between molecules. If any monocrystal of such organic compounds exhibits particularly benefiting infrared (IR) spectra, they can be potentionally used in nonlinear optics applications, for example pump-probe laser techniques.

In following paragraphs, monocrystals growth and characterization techniques are presented. Selected information crucial for crystallization and following processes about the compounds are discussed within each section. Table 6.1 contains basic information about used chemicals.

Table 6.1: Crystallographic symmetries of grown crystals

Compound	Producer	Symmetry	Euler angles
L-tartaric acid	LachNer	monoclinic $P2_1$	$\beta = 100.13°$ [54]
Succinic acid	LachNer	monoclinic $P2_1/c$	$\beta = 91.5°$ [55]
2:1 Urea-Succinic acid	Mach, LachNer	monoclinic $P2_1/c$	$\beta = 96.7°$ [56]
D-sucrose	LachNer	monoclinic $P2_1$	$\beta = 102.9°$ [57]

Substance masses and water volumes for solution preparation are shown in Tab 6.2 in Section 6.5.

6.1 L-tartaric acid

L-tartaric acid (LTA) is a butandioic acid with 2 hydroxyl groups substitued in the secondary carbons. Structural name of this molecule with 2 chirality centres is (S,S)-2,3-dihydroxybutanedioic acid.

Due to the presence of the hydroxyl groups, the acid is greatly soluble in water. Saturated water solutions were prepared according to appropriate solubility curves. The most well-known solubility data were obtained by Dalman [58] and Apelblat [59], see Fig. 6.1. There are certain deviations between the data of these authors, however, on the basis of my emphirical study, better results were achieved using Dalman's analytical expression of the solubility curve.

$$S_{\mathrm{LTA}} = 0.2643T + 51.8573 \tag{6.1}$$

Temperature of the laboratory was thermostated at constant temperature of approximatelly 23 °C. First, slightly supersaturated solution was prepared in order to obtain seed crystals. This was achieved by changing the concentration of the solution by preparing the solution saturated at temperature of approximatelly 28 °C. The solution was stirred well for 1 hour at constant temperature, filtered using Whatman filtration papers, covered with perforated aluminum foil and left undisturbed. The seed crystals started to grow after 2-3 days. A seed with no optical

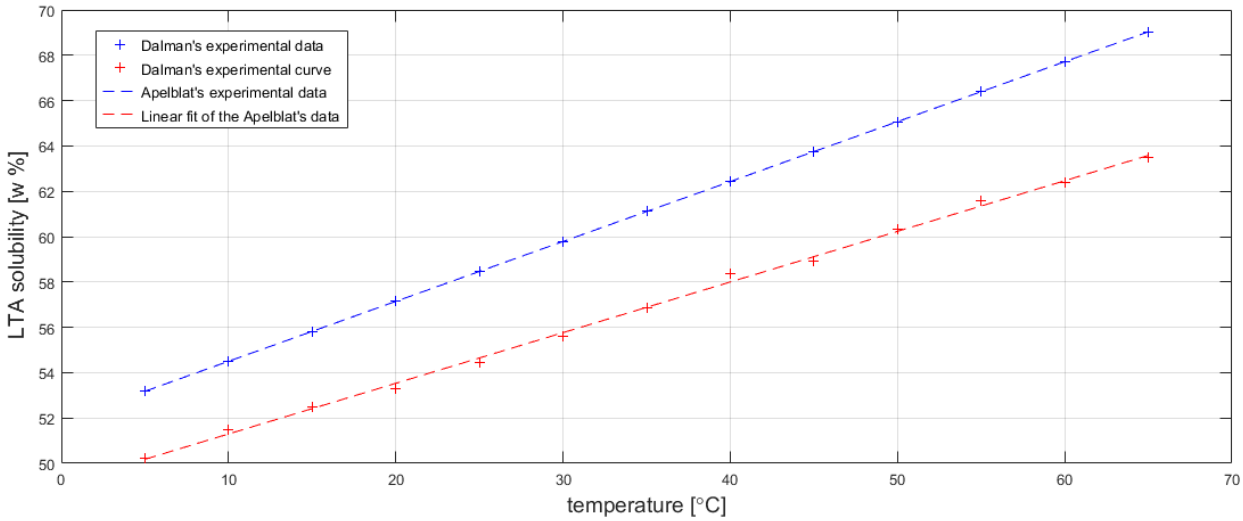

Figure 6.1: Dalman's and Apelblat's LTA solubility curves.

cracks and with well-defined crystalographic shape was dessicated and added into the new freshly prepared mother solution. Due to the transparency of the solution, the growth was controlled by eye – after 10 days of growth, several optically perspicuous polycrystal phases started to grow on the surface of the monocrystal, therefore the growth was interrupted. Good-quality and well-oriented 15 × 15 mm LTA monocrystal was obtained (Fig. 6.2A).

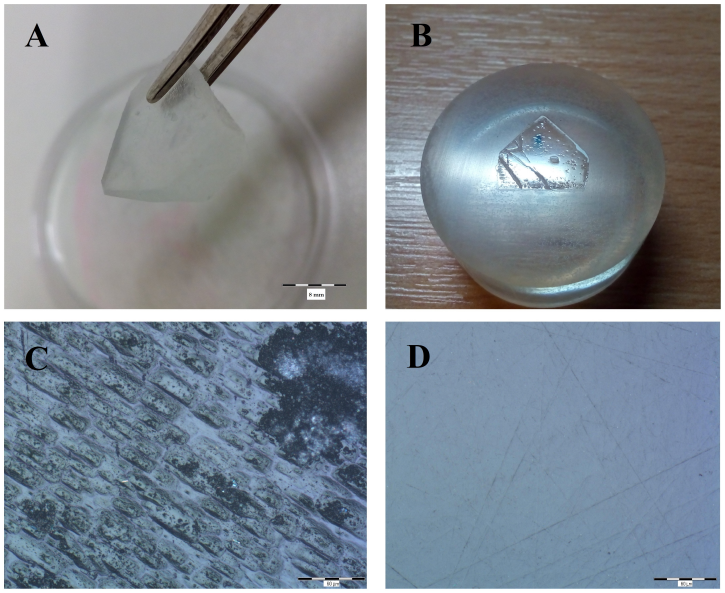

Figure 6.2: **A:** 15 × 15 mm LTA monocrystal after crystalization. The bar length is 8 mm. **B:** LTA monocrystal fixed in the Specifix-40 Kit resin. **C:** Surface of the crystal after crystalization. The bar length is 80 µm. **D:** Surface of the crystal after grinding and polishing. The bar length is 80 µm.

The (001) and (00$\bar{1}$) planes are crystallographically the most developed ones, therefore the most suitable for ellipsometric measurements. To get as little distorted ellipsometric information as possible, the crystal was fixed into polymeric resin Struers Specifix-40 Kit (Fig. 6.2B) and grinded with Metalimex grinder to flatten the surface of the crystal. P60, P400 and P1500 Hermes waterproof abrasive papers were used in the order (compare Figs. 6.2C and 6.2D). Flat, but still rough surface, was then dry polished for 4 minutes at 250 rpm using Struers LaboPol-25 polishing machine with 1 µm polishing cloth mounted. The polishing could not be further supported by a diamond abrassive suspension, because they are water or alcohol-based, therefore LTA dissolving.

Unfortunatelly, the polished surface of the crystal (Fig. 6.2D) remain untouched for tenths of minutes only. By further literature analysis, it was found that LTA is moderately hygroscopic [60], because of the presence of the hydroxyl groups. The surface is completely covered with thin film of amorphous and non-reflective Tartaric acid hydrate in the manner of minutes to hours. The measurement is therefore hardly repeteable or even achiveable.

6.2 Succinic acid

The succinic acid (SCA) is butanedioic acid with no chirality centre. Absence of the hydroxyl groups causes comparatively lower solubility then in case of the LTA, but in advance, there is no reason for the hygroscopicity [60].

The monocrystal growth was initiated by inserting the seed crystal of SCA into saturated solution prepared according to Apelblat data [59]. Despite the fact, the beakers were hold in temperature controlled water bath with 0.5 °C temperature-control accuracy, after few days, all grown crystals were full of cracks and with opaque milk-like turbidity spreading from the geometrical centre of the crystal as the crystal grows up. The turbidity is signalizing presence of the polycrystalline phases. Succinic acid monocrystal growth is possibly temperature fluctuation or vibration extremely sensitive, therefore urea-succinic acid (USA) cocrystals growth was found to be more viable alternative.

6.3 2:1 Urea-Succinic cocrystals

Urea-organic acid salts are commonly grown cocrystals [61, 62, 63, 64]. Urea in the structure of organic acid may cause change of the crystal symmetry, in the case of the hydroxyl-substituted butanedioic acids, the crystal symmetry remains monoclinic, however the space group differs due to change of the lattice parameters. This change also causes optical properties change (dielectric tensor) of the monocrystal.

The growth method is based on the slow evaporation method again. As in the previous cases, monocrystal growth was started using the seed crystal inserted into the mother saturated solution of the U_2S salt. Saturated solution was prepared at the temperature of 30 °C according to the Urea-Succinic acid-Water phase diagram [64] (Fig. 6.3).

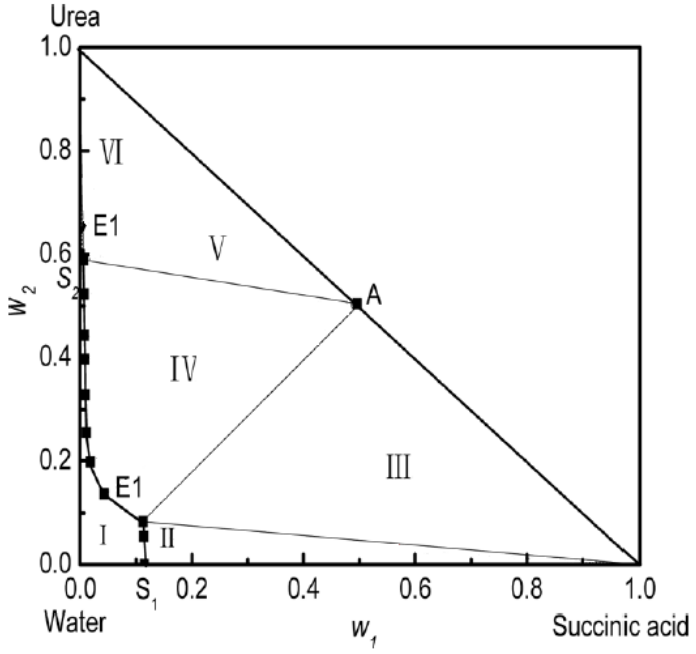

Figure 6.3: Ternary phase diagram of Urea-Succinic acid-Water system at 30°C. The solubility curve for water-U_2S salt is the solid curve between I and IV region. I is unsaturated region, II crystalline region of SCA, III crystalline region of SCA and U_2S, IV crystalline region of U_2S, V crystalline region of U_2S and urea, VI crystalline region of urea [64].

U_2S monocrystals grow very fast (approximatelly 2 mm per day), despite of the fact, when good-quality seed was used, grown monocrystal possesses well-grown habitus, no optical cracks or inhomogenities, nor polycrystalline phases.

Hygroscopicity of SCA was discussed in previous section, urea is hygroscopic only when the relative humidity of the air is very high [65]. All bonds of the salt are saturated, therefore U_2S is neither hygroscopic – stabile under normal conditions.

6.4 Sucrose

In contrast with butanedioic acids crystals preparation, sucrose monocrystal growth demands quite different aproach. As usual, the seed crystals were prepared from supersaturated solution according to the solubility curve [36]. However, sugars generally are extremely soluble even in small ammount of water. Typical example is wild honey, as supersaturated solution of inverted sugar. The solubility curve shown in Fig. 6.4 does not work very well for monocrystal growth. During the experiments, the excessive solubility has manifested and it becames clear, that the curve is very inacurrate, but it still can be used for orientation purposes.

The solution was prepared at 50 °C, the seed crystal was inserted and was observed carefully within 10 minutes period, if it dissolves, grows or overcrystalizes. In most cases, polycrystalic phases started to grow almost immediately, therefore the temperature of bath was gradually

increased up to approximately 58 °C. The parasite polycrystals started to dissolve and the seed crystal started to grow. In *all* cases, the temperature had to be regulated as needed to keep the crystal grow and the experiment was interrupted after 2 to 6 hours, as the polycrystaline phases on the crystal surface started to grow again. The temperature regulation was no longer effective possibly due to the insufficient 1 °C accuracy of the heater. Fortunately, the growth process of the sucrose is very fast. The whole process was conducted repeatedly for 15 times until surprisingly high-quality monocrystal was obtained, see Fig. 6.5.

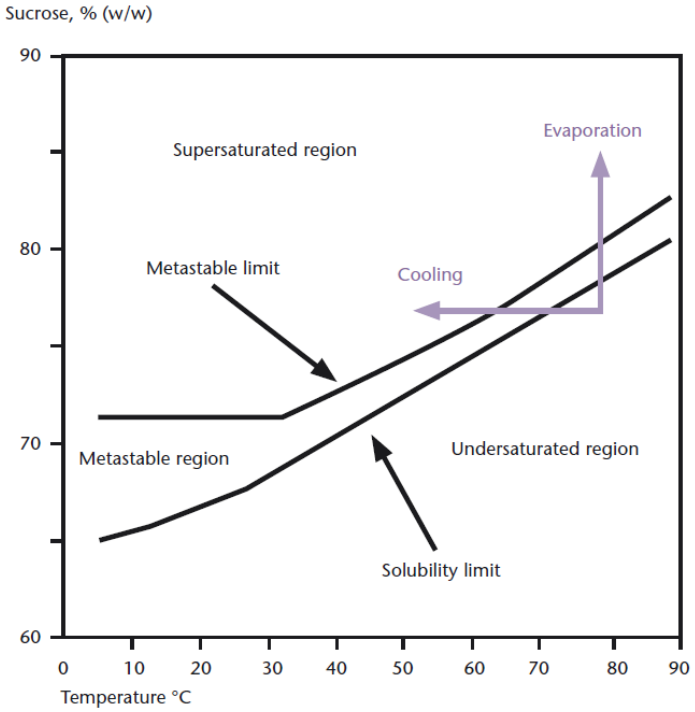

Figure 6.4: Solubility curve of sucrose. Wide metastable region is shown [36].

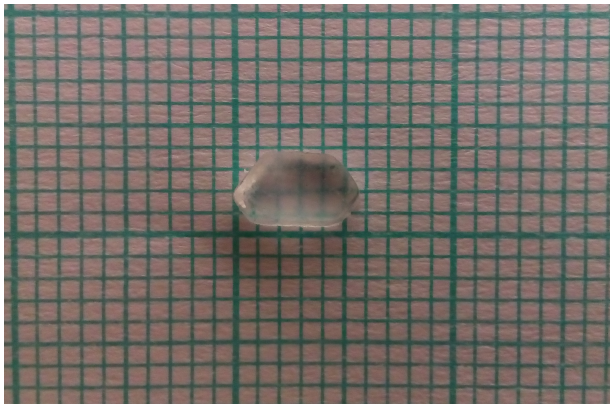

Figure 6.5: Sucrose single crystal.

.

6.5 Monocrystal analysis

For spectroscopic ellipsometry, it is crucial to determine, if the grown crystals contain only 1 monocrystalic phase. Standart X-ray diffraction analysis on monocrystal is very reliable technique, however it can be done only on crystals with size up to 0.5×0.5 mm. For ellipsometric purposes, it is recommended to grow crystals of size at least 3×3 mm. If the XRD measurement was conducted on 0.5×0.5 mm seed monocrystal, there is no guarancy, that the same crystal will be monocrystal after a week of growth.

Fortunately, crystals of all mentioned compounds are transparent in visible spectrum of light, so it is possible to use transmission polarized light optical microscopy. If light travels through linear polarizer, it is blocked when goes through polarizer with its axis oriented perpendicular to the first one. The anisotropic sample is situated between the cross-polarizers. When we rotate with the sample, the intensity of trasmitted light changes according to Malus's law, therefore, we can find intensity minima and maxima. If we measure a monocrystal, we surely find position, where the sample is homogenously bright (light is fully transmitted) or dark (light is blocked by the second polarizer)[5]. The same effect is observed, when the sample stays still and the polarizator axis rotates. If the sample is fixed in the resin already, we can no longer use the trasmission microscopy. For this purposes, the analysis was done using Bruker Hyperion microscope in the reflection configuration with two polarizers mounted.

Figure 6.6 confirms the validity of the described technique. If we observe two mutually perpendicular oriented Cu(1,3-diaminopropane)Cl_2 monocrystals under the polarization microscope and rotate the axis of one of the polarizers, we observe the extinction effect perfectly as described above. Further, if we analyse surely polycrystal, we can see (Fig. 6.7), that many different undulatory extinctions occur, each for the particular monocrystalic phase. As shown in Fig. 6.8, the grown USA cocrystal is perfectly monocrystalic (despite the lamelar habit) with noticeable polycrystalic phases on its surface, however we can easily grind them off. The sucrose crystals possesses perfect habit as well. It consists of two perfectly parallel monocrystalic phases with visible sharp-shaped boundary (Fig. 6.9, upper half). After the grinding and the polishing, the whole volume of the sample is homogenous and monocrystalic (Fig. 6.9, lower half.).

Table 6.2: Mass and volume ammounts best for the crystallization process.

Crystal	Water [ml]	LTA [g]	SCA [g]	Sucrose [g]	Urea [g]
LTA	8.000	10.899	—	—	—
SCA	10.000	—	0.675	—	—
Sucrose	8.000	—	—	20.169	—
USA	8.000	—	0.316	—	1.828

[5] Crystallographicaly speaking, we call this effect the undulose (or undulatory) extinction [66]. The polarization microscopy diagnosis is very popular method among the crystallographers.

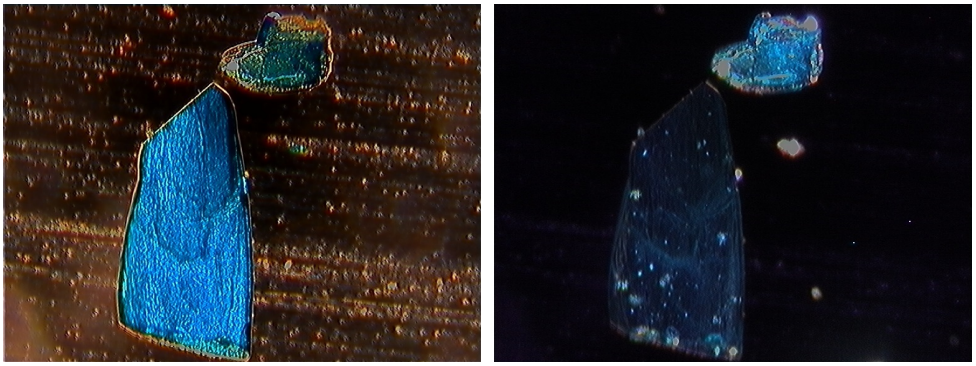

Figure 6.6: Demonstrative figure: Observation of two mutually orthogonally oriented Cu(1,3-diaminopropane)Cl_2 monocrystals under polarization microscope Bruker Hyperion, polarization axis is rotated. **Left:** Configuration polarizer-analyzer 0°-0°. **Right:** Configuration polarizer-analyzer 0°-90°.

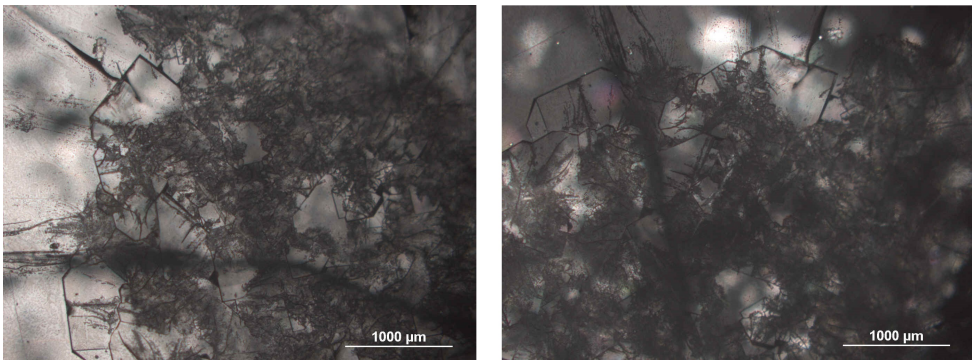

Figure 6.7: LTA crystal under polarization optical microscope Olympus BX60. The geometrical centre of the crystal is macroscopically turbid, using polarization microscopy, it is due to the polycrystallic character of the sample.

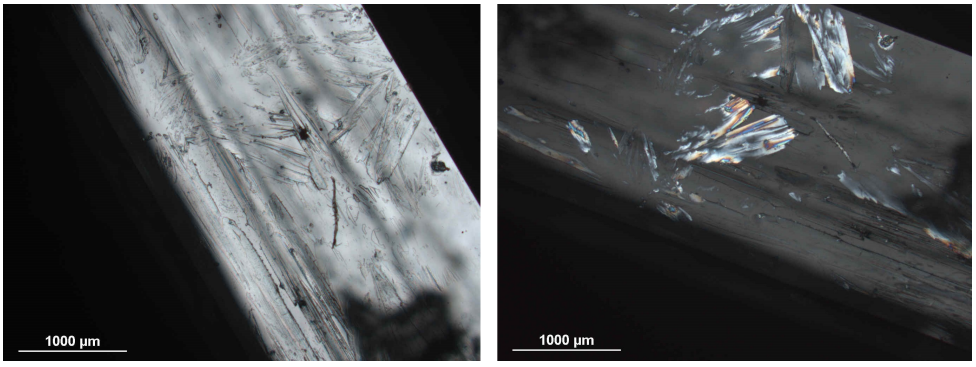

Figure 6.8: USA crystal under polarization optical microscope Olympus BX60. It is obvious, that the sample is monocystalic with a few parasite crystals of different orientation on the surface.

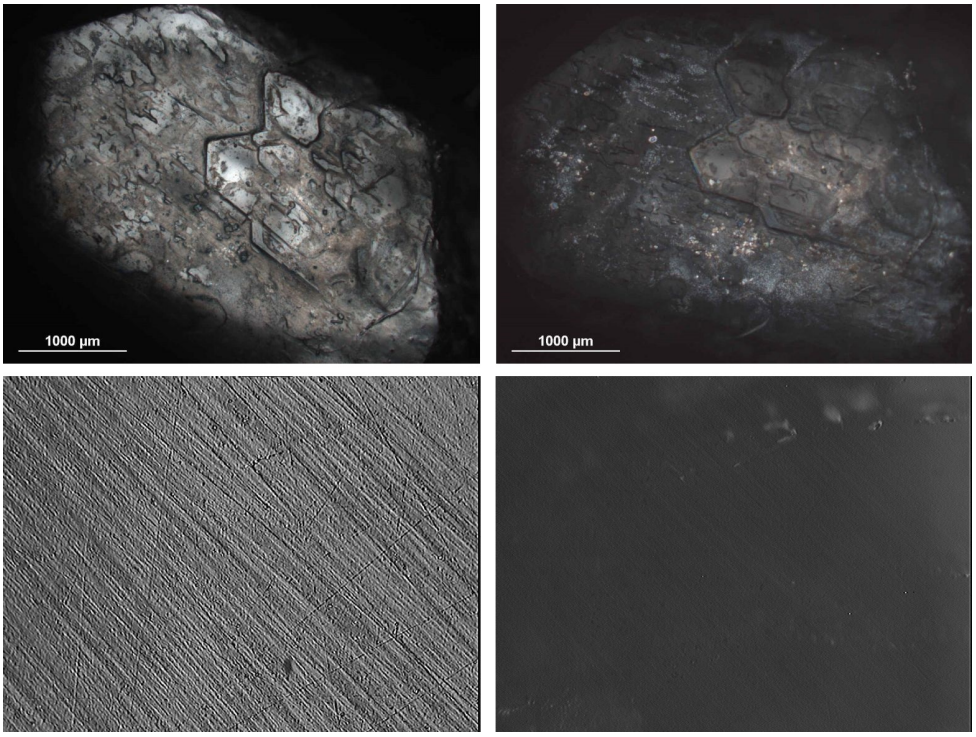

Figure 6.9: **Upper half:** Sucrose single crystal under polarization microscope Olympus BX60 before grinding and polishing. The crystal consists of two paralell monocrystals. The surface is greatly messy, because it is covered by remains of the sucrose viscous solution. **Lower half:** Sucrose polished monocrystal under polarization microscope Bruker Hyperion in reflection configuration. The monocrystal morphology is strictly homogenous.

7 Determining dielectric tensor spectra of anisotropic crystals

Following paragraphs describe ellipsometric measurements and anisotropic response modeling of two different natural crystals – minerals. First, cubic pyrite FeS_2 is treated as a most simple case in the field of crystal ellipsometry. Second, uniaxial cassiterite SnO_2 dielectric tensor is calculated. This chapter is intended as an introduction to the ellipsometry of particularly complicated organic molecular crystals grown in Chapter 6. More research is required due to their optical activity and much less perfect surface and crystal habit.

7.1 Pyrite

Pyrite is a FeS_2 (iron pyrite) mineral belonging to pyrite-marcasite subclass of sulfidic minerals. It possesses $2/m\bar{3}$ diploidal symmetry, therefore the mineral belongs to cubic crystal system.[6] Pyrite is one of the most common minerals on Earth. Formerly, pyrite was used as a source of sulfuric acid, nowdays it is ocassionaly used in battery industry. The main mineralogic attributes are shown in Table 7.1 [40].

Table 7.1: Special mineralogic parameters of Pyrite.

Color	Pale brass-yellow
Crystal habit	Cube, very often pyritohedral, sometimes octahedral
Luster	Metallic, glistening, dull on tarnished spots
Tenacity	Brittle
Mohs scale	6–6.5

The ellipsometric measurements were conducted on the (100) plane of $15 \times 15 \times 15$ mm perfectly cubic mineral, see Fig. 7.1.

The ellipsometric measurement using Woollam RC2 Mueller matrix spetroscopic ellipsometer is considered to be mostly demonstrative, for the purpose to show the difference between Mueller matrix spectra of the isotropic and anisotropic sample.

In the nature, it is quite common, that the minerals are not perfect monocrystals, despite the fact, they possesses perfect crystal habit. Therefore, to determine, if the sample is monocrystalic, for all measurements, angle of incidence 65° was chosen in order to provide sufficient sensitivity. The sample was fixed on the azimuthal rotation sample holder using vacuum. Azimuthal angles 0° to 360° with step 10° were measured. The experimental Mueller matrix on angle of rotation dependance is showed in Fig. 7.2.

[6] In some textbooks of solid state physics we can see that the term crystal refers only to anisotropic solids. This erroneous use is misleading, because crystallographic definition of a crystal can also be met by isotropic substances.

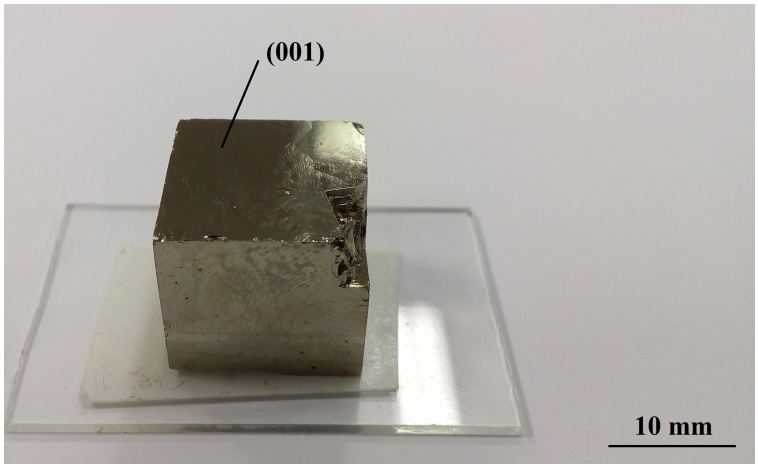

Figure 7.1: Pyrite single crystal placed on the microscope slide and fixed with double-side adhesive tape.

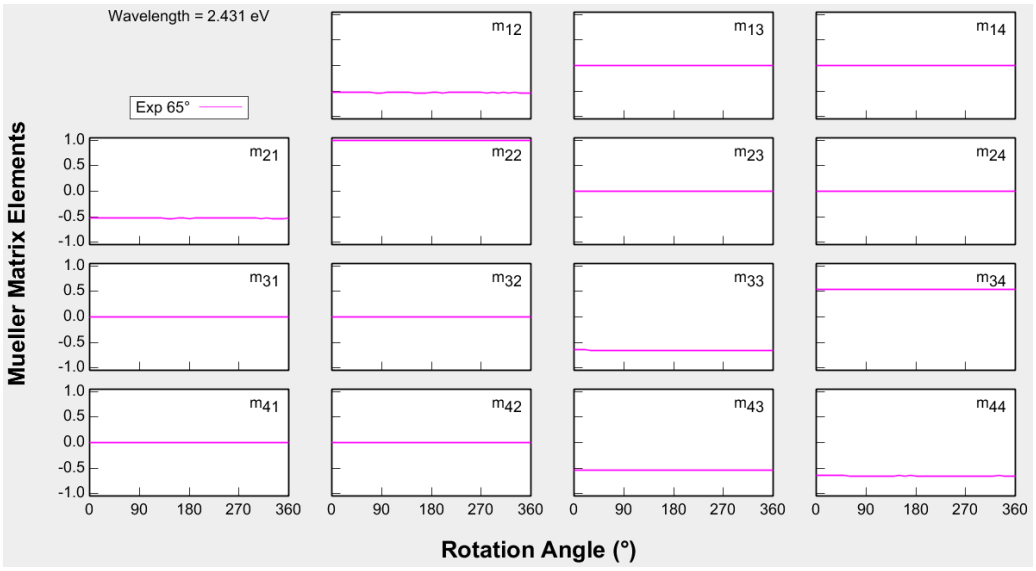

Figure 7.2: Rotation spectra of experimental Mueller matrix for $E = 2.431$ eV.

Ideally isotropic sample has all physical quantities as a function of direction. From Fig. 7.2 is obvious, that the Mueller matrix elements do not change with the rotation and our sample is therefore truly isotropic. Fig. 7.3 shows, that the sample is negligibly depolarizing, therefore Eq. (2.39) and Eq. (2.40) are valid.

The experimental data were simultaneously modeled in CompleteEASE software using B-spline function [67]. B-splines are a basis set of polynomial splines. The experimental ε_2 spectra are segmented to the knots – points, between which the curve transitions from one polynomial segment to another and for each, the basis function B_i^k is calculated. The resulting curve is weighted sum of the basis functions then. To keep the physical meaning, B-splines are Kramers-

Kronig consistent and the dispersion spectra ε_1 are calculated as follows:

$$\varepsilon_{1,\,\mathrm{BS}}(E) = \varepsilon_1(\infty) + \sum_{i=1}^{n} c_i \frac{2}{\pi} P \int_0^{\infty} \frac{\omega B_i^k(\omega)}{\omega^2 - E^2}\,\mathrm{d}\omega \tag{7.1}$$

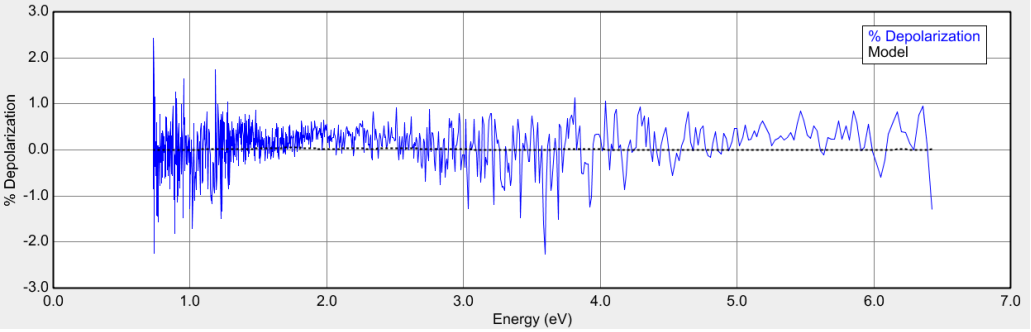

Figure 7.3: Depolarization spectra of pyrite compared to model. Azimuthal rotation of 140°

B-splines also assumes the existence of the transparent region and band-gap energy calculations. The model includes surface rougness compensation. The fit optimality is quantified with MSE (mean squared error) value and according to the CompleteEASE software, it is calculated as follows:

$$\mathrm{MSE} = 1000 \sqrt{\frac{1}{3n-m} \sum_{i=1}^{n} [(N_E - N_M)^2 + (C_E - C_M)^2 + (S_E - S_M)^2]} \tag{7.2}$$

where n is number of wavelengths, m number of fitted parameters, and subscripts E and M denotes experimental and modeled data, respectively. Best fit parameters are shown in Tab. 7.2.

Table 7.2: Best fit parameters of B-spline function model.

E_g	0.970 eV
surface rougness = 2.220 nm	
MSE = 1.356	

The band-gap energy was not set as the fitting parameter in the classical meaning, because it must be known, when treting with B-spline model. The value was manually changed until the MSE minimum value was obtained. The band-gap energy is similar as in [68]. Fig. 7.4 shows the measured and the modeled data for ψ and Δ and the isotropic Mueller matrix elements N, C, and S.

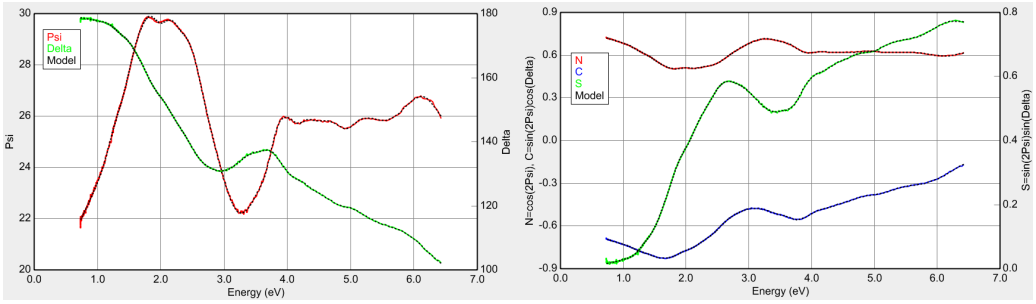

Figure 7.4: **Left:** Ellipsometric angles ψ and Δ compared to the model. **Right:** Isotropic Mueller matrix elements compared to model.

Fig. 7.5 shows the rotation spectra compared to the model for $E = 2.431$ eV. The off-diagonal elements are nonzero, however the deviations are related to the noise.

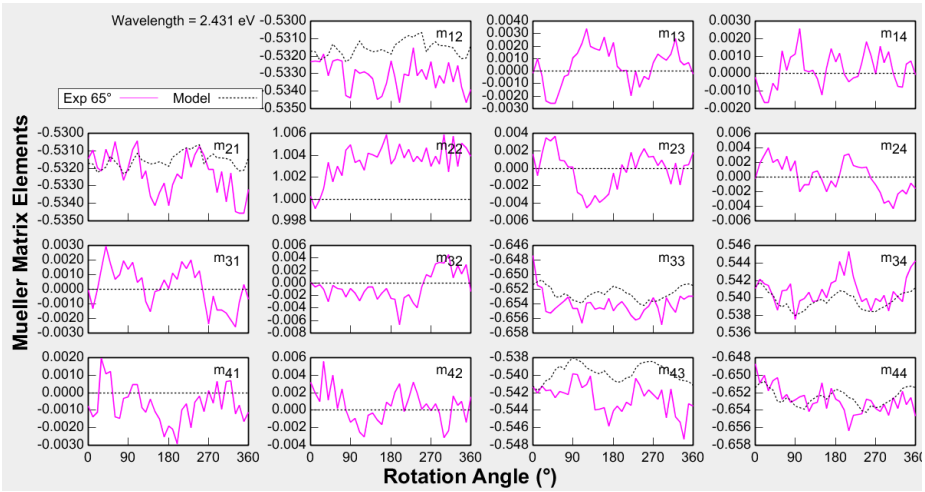

Figure 7.5: Rotation spectra for $E = 2.431$ eV compared to the model. Note the small deviations within off-diagonal elements, which correspond to noise of separately fitted spectra.

Based on the described model, pyrite dielectric function and refraction index were obtained, respectively. The spectra agree with [69].

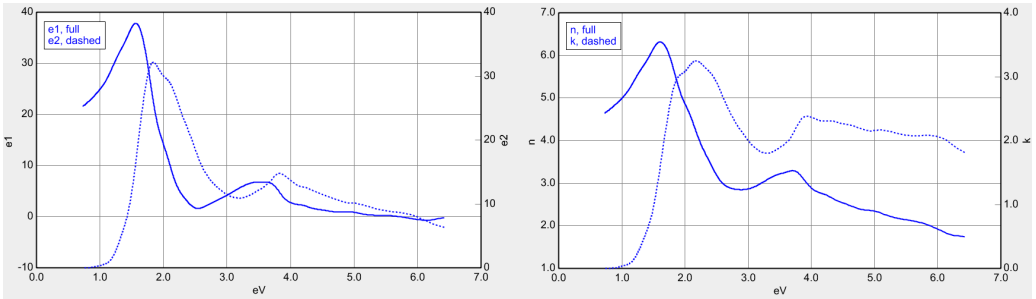

Figure 7.6: **Left:** Dielectric function of the pyrite. **Right:** Refractive index and absorption coefficient of the pyrite.

7.2 Cassiterite

Cassiterite is a SnO_2 (tin oxide) mineral belonging to MeO_2 class and rutil subclass of oxides. It possesses 4/mmm Hermann-Maugin point group, therefore, it has tetragonal symmetry and uniaxial positive anistropy. SnO_2 is economically the most important tin ore and significant source of Niobium (Nb) and Tantalum (Ta). Naturally, cassiterites contain a broad variety of intermixtures (Ti, Fe, Nb, Ta, Mn...). Depending on the type of the mixture, the color of the crystal is directly affected. The pure form of the Cassiterite is colorless. The main mineralogic parameters are shown in Tab. 7.3 [40].

Table 7.3: Special mineralogic parameters of Cassiterite.

Color	Black, gray, brown, yellow, rarely colorless
Crystal habit	Pyramidal, dipyramidal, rarely prismatic
Luster	Adamantine metallic, splendent, low-quality minerals greasy
Tenacity	Brittle
Mohs scale	7

The ellipsometric measurements were conducted on the $\{110\}$ cut of 8×5 mm colorless monocrystal with splendent and perfect luster. The sample contains a lot of mixtures, therefore the overall color is brown mostly. The $\{110\}$ plane was chosen to keep the optical axis of the crystal in the plane of the cut.

The ellipsometric measurements were conducted using Woollam RC2 Mueller matrix spectroscopic ellipsometer. For all measurements, the angle of incidence 50° was chosen, because the elliptic beam spot was completely within the surface of the sample, therefore no focusing optics was needed. The sample was fixed on the azimuthal rotation sample holder using vacuum. First, the position of the optical axis had to be determined. For this purpose, azimuthal rotation dependent measurements were conducted between angle of 0° to 180° with step 10°. All partial measurements were done separatelly, each was manually adjusted to maximize the correctness of the information. It wasn't necessary to conduct 180° to 360° measurements, due to the symmetry. If the optical axis is alligned perfectly the same, as the coordinate axis, off-diagonal elements of Mueller matrix vanish – no polarization conversion occurs. The optical axis position was found to be around azimuth angle 70°. Additional fine measurements were done between angles 68° and 72°. The position of the optical axis was found to be at 71° of azimuthal rotation (Fig. 7.7).

Therefore, the coordinate Euler angles, which distinguish the general orientation of the coordinate system related with the sample with respect to the laboratory coordinate system, were determined to be $\varphi = 0°$ and $\theta = 0°$ due to the symmetry defined by the cut along the $\{110\}$ plane. The correctness of this fact was confirmed modeling the spectra of two orthogonal azimuthal rotations: 71° ($\varphi = \theta = 0°$) and 160° ($\varphi = \theta = 89°$), respectively.

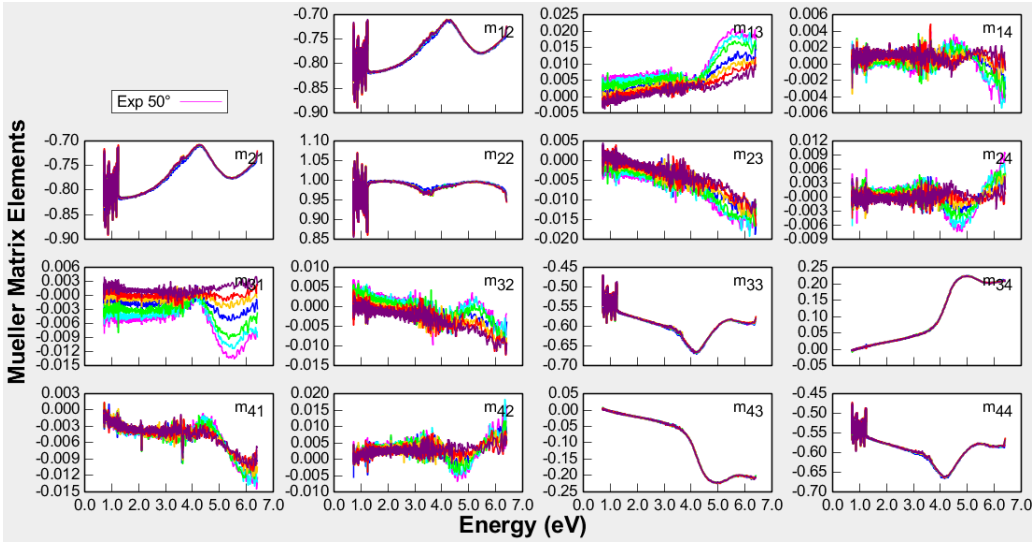

Figure 7.7: Determining the position of the optical axis.

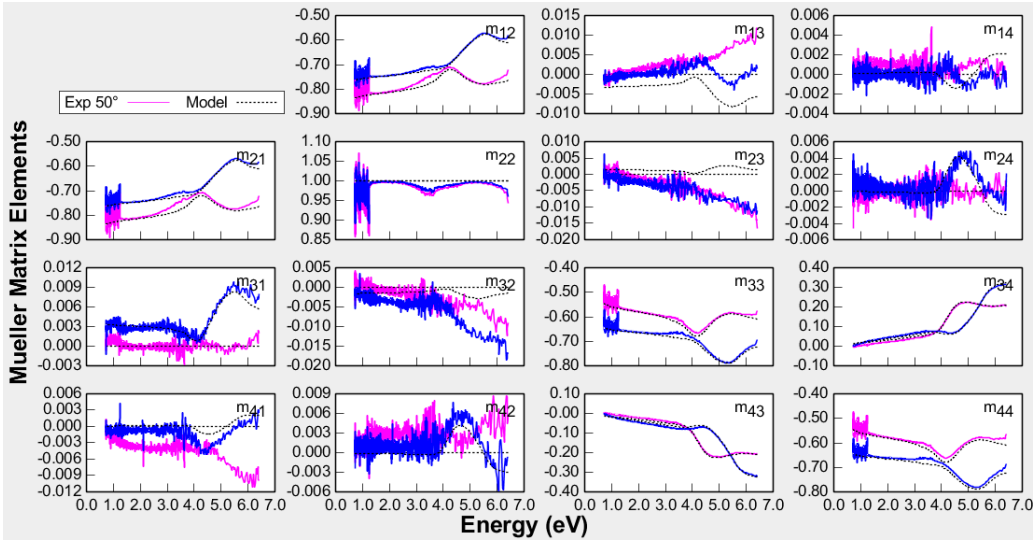

Figure 7.8: Experimental and modeled data for orthogonal orientation of the sample. Both cases reflect the allignment of the optical axis in the coordinate axis.

Now, having the sample oriented, to determine the dielectric functions of the crystal, all 18 azimuthal orientations from 0° to 180° were fitted (see fig 7.10) simultaneously using double Tauc-Lorentz oscillator [70],

$$\varepsilon_{2,\,\mathrm{TL}}(E) = \begin{cases} \frac{1}{E}\,\frac{AE_0C(E-E_\mathrm{g})^2}{(E^2-E_0^2)^2+C^2E^2} & \text{for } E > E_\mathrm{g} \\ 0 \text{ for } E \leq E_\mathrm{g} \end{cases} \tag{7.3}$$

where A is amplitude, C broadening term of the peak, E photon energy, E_0 peak central energy, and E_g is band gap energy. The data were fitted in the CompleteEASE software. First, the

imaginary part of the dielectric function was determined, and in the second step, the real part was calculated using Kramers-Kronig dispersion relations, where P is Cauchy principal value.

$$\varepsilon_{1,\,\mathrm{TL}}(E) = \varepsilon_1(\infty) + \frac{2}{\pi} P \int_{E_\mathrm{g}}^{\infty} \frac{\omega \varepsilon_2(\omega)}{\omega^2 - E^2}\,\mathrm{d}\omega \tag{7.4}$$

The model includes surface rougness compensation. Best fit parameters are shown in Tab. 7.4.

Table 7.4: Best fit parameters of double Tauc-Lorentz oscillator.

ordinary	TL1	TL2
A_1	95.774	101.069
C_1	8.404	1.853
E_{01}	11.022	4.142
$E_{\mathrm{g}1}$	3.714	3.714 (coupled)
extraordinary	TL1	TL2
A_2	184.198	13.306
C_2	6.320	0.855
E_{02}	6.235	5.635
$E_{\mathrm{g}2}$	4.033	4.033 (coupled)
$\varepsilon_1(\infty)$	1.722	—
$\varepsilon_1(\infty)$	—	3.148
surface rougness = 3.740 nm		
MSE = 11.318		

The band gap energy is in a good agreement with literature, despite the fact the publicated values differs between 3.6 eV [71], through 3.8 eV [72] up to 4.1 eV [73]. The deviations may be caused by the effect of impurities in the sample.

Figure 7.9 shows the measured and the modeled data for ψ and Δ and the isotropic Mueller matrix elements N, C, and S.

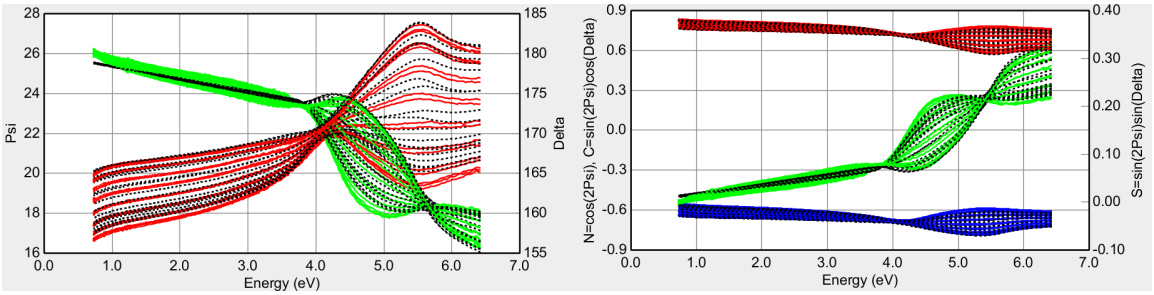

Figure 7.9: **Left:** Measured and modeled data of ψ and Δ. **Right:** Measured and modeled data of N, C, S isotropic components.

Figure 7.10 shows the best fit for 18 azimuthal rotations. The deviations between measured and modeled data especially within m_{13}, m_{14}, m_{23}, and m_{24} elements are mainly caused by the

imperfectness of the sample surface and small discrepancies, when adjusting was done separately for each measurement. The experimental Mueller matrix should be symmetric, but it is not and it causes the imperfectness of the fit.

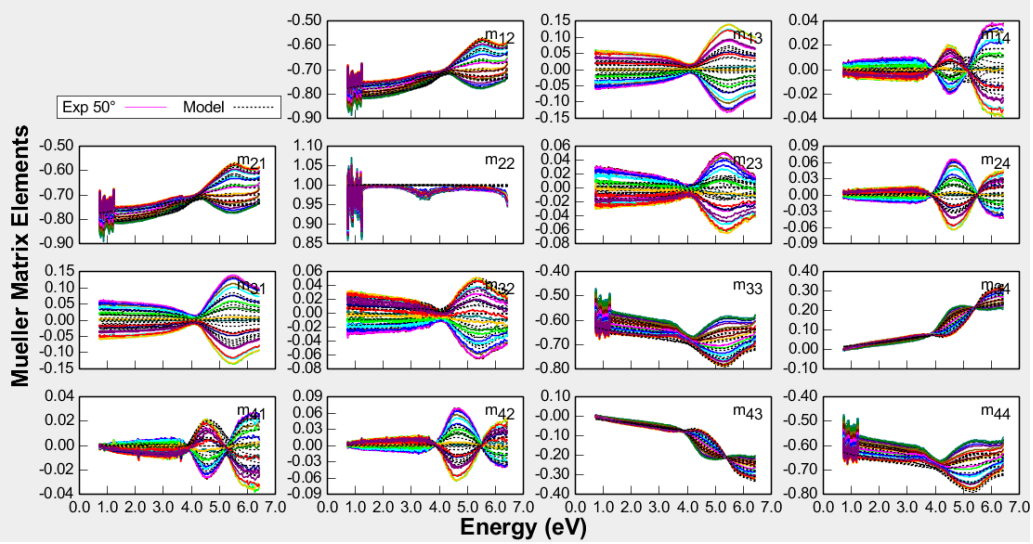

Figure 7.10: Mueller matrix spectra of all 16 measurements compared to the model.

Based on the described model, the dielectric tensor components were obtained. Figure 7.11 shows the ordinary and extraordinary elements separately, Fig. 7.12 both together.

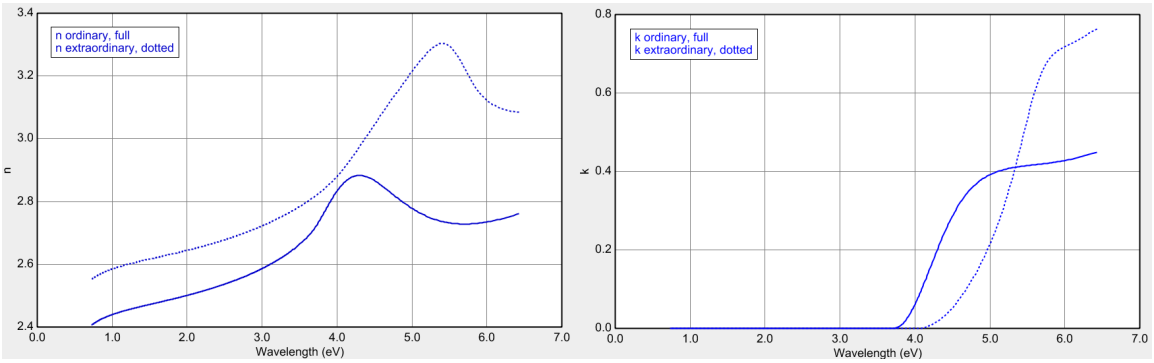

Figure 7.11: **Left:** Ordinary and extraordinary refraction index of the cassiterite. **Right:** Ordinary and extraordinary absorption coefficients of the cassiterite.

The ordinary and extraordinary dielectric tensor componenets ε_1, ε_2 are shown in the left part of Fig. 7.12. Right part shows ordinary and extraordinary indexes of refraction and related absorption coefficients.

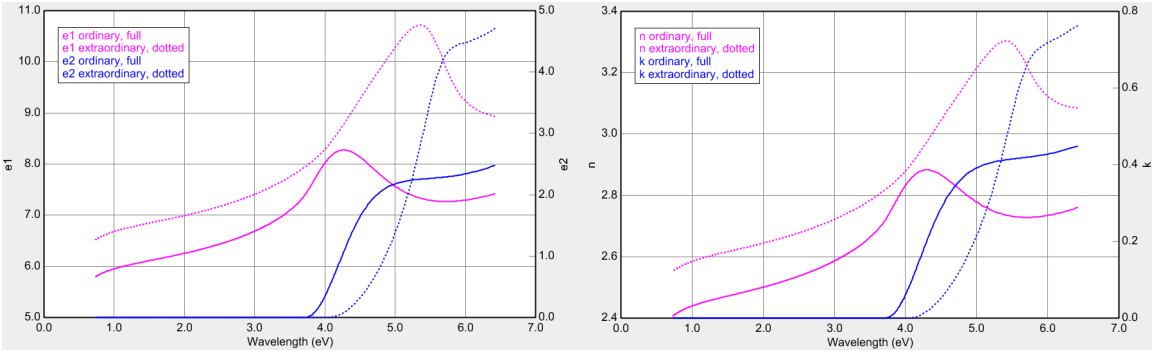

Figure 7.12: **Left:** Ordinary and extraordinary dielectric functions (dielectric tensor components spectra) of the cassiterite. **Right:** Complex refractive indexes of the cassiterite.

8 Diffraction efficiency: Principles and measurements

Diffraction gratings are special optical structures that are commonly used in many disciplines and devices, from analytical chemistry spectrometers, through x-ray diffraction analysis or stellar observations [74], to chirped laser pulse amplification [75]. The diffraction efficiency characteristics represent the direct quantitative and qualitative parameter of particular diffraction grating. In following paragraphs, the principle of diffraction gratings is briefly introduced. Next, diffraction efficiency is discussed, and novel method of diffraction efficiency measurements using spectroscopic ellipsometer is proposed.

8.1 Blazed diffraction gratings

Diffraction gratings are structures with periodically modulated surface. This modulation directly affect the amplitude and phase of the incident wave, resulting in the interference of the reflected or transmitted wave. Generally, there are two different types of diffraction gratings. Transmission gratings are periodically modulated with very thin slits, while reflection gratings are often made of periodically modulated substrate coated with a thin metal film. From now, we will talk about reflection gratings only.

If we seek for the phase condition of the constructive interference, two approaches can be employed. From the wave optics, the boundary conditions must be satisfied, therefore, tangential component of the wave vector must be continuous, which leads to

$$k_{\mathrm{m,t}} = k_{\mathrm{i,t}} + mK \tag{8.1}$$

where m is an integer number corresponding to the diffraction order, $k_{\mathrm{i,t}}$ is the tangential component of the incident wave vector, which is transformed discreetly by the grating vector $K = 2\pi/d$. The reflected wave vector is therefore irradiated into special directions only. If the interface is in the xy plane, the incidence plane is parallel to the grating modulation and the grating is periodic in one dimension (called the diffraction order) only, the *grating equation* can be derived:

$$d(\sin\varphi + \sin\beta) = m\lambda \tag{8.2}$$

where β is the diffraction angle, φ denotes the angle of incidence, and d is the grating period. Another way to derive the grating equation is to calculate total phase difference between two rays reflected from two neighboring grooves [76]. If performed correctly, we get the left side of the Eq. (8.2). The right side of the Eq. (8.2) comes from the constructive interference condition.

Note, that we have been talking about general periodic modulation so far, because the Eq. (6.2) is universally valid, if the conditions from the discussion are met. However, variety of differently modulated gratings exist, the most common are rectangulary modulated, blazed

(roofed, sometimes called echelette[7] gratings) and sinusoidal. This thesis is focused on the study of the blazed diffraction gratings, which are designed to reflect the incident light into one specific order only, while minimizing the reflection into other orders, especially into the specular reflection [77]. The geometrical meaning of the quantities from Eq. (8.2) is shown in Fig. 8.1.

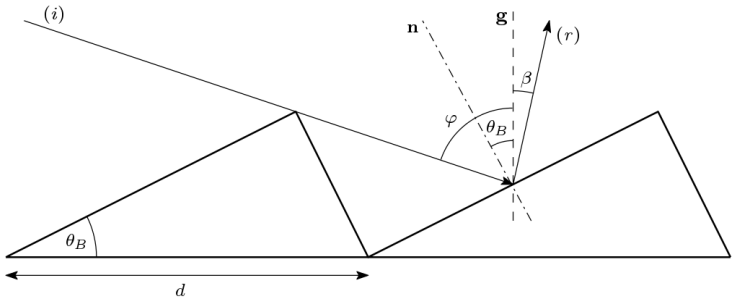

Figure 8.1: The grating with groove period d and blaze angle θ_B. φ is the angle of incidence of the incoming ray (i) measured from the normal $\boldsymbol{g}$ of the grating. β defines the direction of the diffracted ray (r).

Figure 8.2 shows the principle of diffraction grating. The sign convention of the angle β and integer m is defined. The angle β is negative, if the reflected order lyes in the same halfplane as the incident wave.

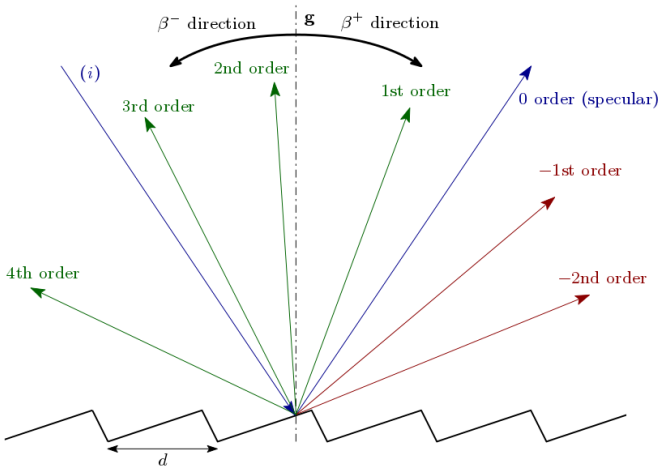

Figure 8.2: Incident ray (i) is reflected into the diffraction orders given by the grating equations. The 0 order is specularly reflected, so $\beta = \varphi$. The sign convention of m and β is given.

[7]From French, échelle, meaning ladder. The groove shape of these gratings is optimized for use at high diffraction orders.

8.2 Absolute diffraction efficiency measurements

Diffraction efficiency is an ammount of intensity of the light diffracted by a grating, with respect to the energy of the incident light. According to [78], we distinguish between absolute diffraction efficiency and relative diffaction efficiency. The *absolute diffraction efficiency* is the ratio of the diffracted light intensity of a given order, relative to the intensity of the incident light. The *relative diffraction efficiency* is the ratio between the intensity of the diffracted light into all diffraction orders, and the intensity of the incident light.

For diffraction efficiency measurements, we extend here the measurement abillity of the Woollam RC2 spectroscopic ellipsometer. Standart measurements in the reflection configuration are designed for the specular reflection detection at given angle of incidence, set by the pair of coupled stepper motor drivers (see Fig. 8.3).

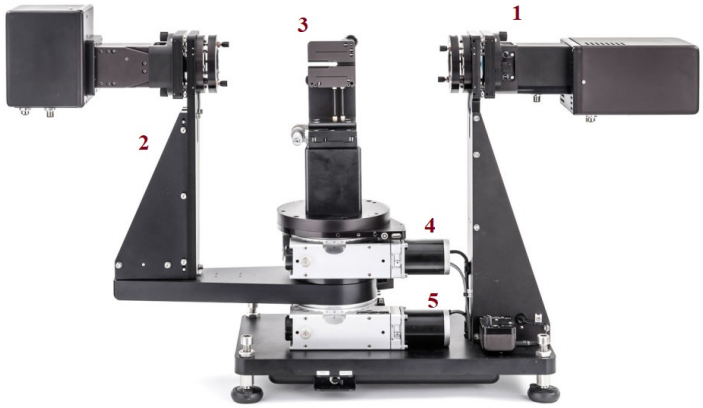

Figure 8.3: Woollam RC2 Mueller matrix spectroscopic ellipsometer scheme. 1 – source; 2 – mobile receiver arm; 3 – sample stage; 4 – sample stage stepper motor unit; 5 – receiver stepper motor unit [79]

.

Diffraction efficiency measurements were done as follows. First, the intensity baseline was measured, then angle of incidence was set. Disconnecting the sample stage stepper unit, the receiver arm was mobile independent of the sample stage. Edmund Optics blazed diffraction grating with the period $d = 1000$ nm and blaze angle 17.45° was placed on the sample stage. Allignment target mounted on the receiver arm and intenisty pre-measurements ensured us, that the diffraction orders lye perfectly within the plane of the incidence. Diffracted intensities of the diffraction orders within the range of 38° to 180° from the source were measured with step of 0.2°.

One must pay attention when orienting the grating. Depending on the way, how the facets of the blazes (defined by blaze angle θ_B) are oriented at given angle of incidence φ. Fig. 8.4 shows the case, when only the longer one of the facets is illuminated, and the shorter (shadowed) ones do not contribute to the overall phase difference of the diffracted light.

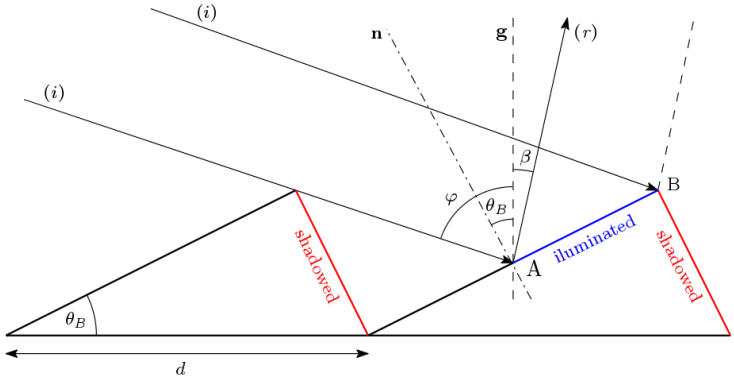

Figure 8.4: One of the possible orientation of the grating. The red lines represent the shadowed facets, the line segment between points A and B shows the illuminated area of the longer facet. The length of AB is dependent of the angle of incidence φ.

Depending on the angle of incidence φ, the length of the illuminated line segment AB changes. For $\theta_{\mathrm{B}} \leq \varphi < 90°$, only the longer facet is illuminated. For $\varphi < \theta_{\mathrm{B}}$, whole grating is illuminated, and this case must be treated separatelly. The same situation comes to the scene, when we 180° rotate the grating (see Fig. 8.5).

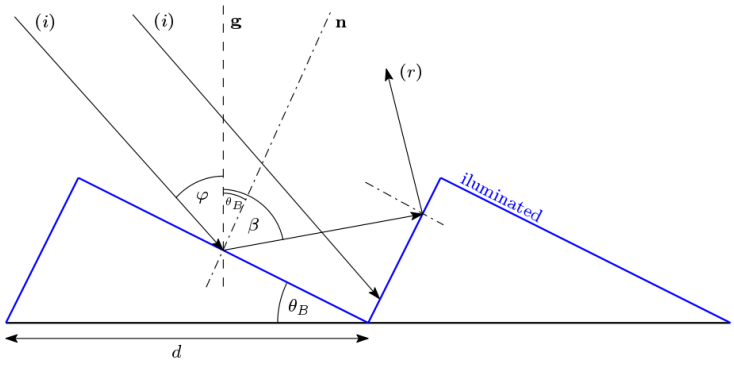

Figure 8.5: Grating rotated by 180°. For any $\varphi \neq 90° - \theta_{\mathrm{B}}$, the whole grating is illuminated, and the incident light is multiple reflected.

The incident beam is multiple reflected for any given $\varphi \neq 90° - \theta_{\mathrm{B}}$, and the phase difference between the reflected rays must be calculate separatelly.

Therefore, we used the configuration defined by Fig. 8.4 and to keep the shadowing effect active, the angle of incidence $\varphi = 45°$ was set, when the blaze angle is $\theta_{\mathrm{B}} = 17.45°$. The measurement was done as is described above. The spectral dependance of the intensity were measured and according to Eq. (8.2), angular dependances were calculated. The resulting absolute diffraction efficiency of the diffraction grating for unpolarized light is shown in Fig. 8.6.

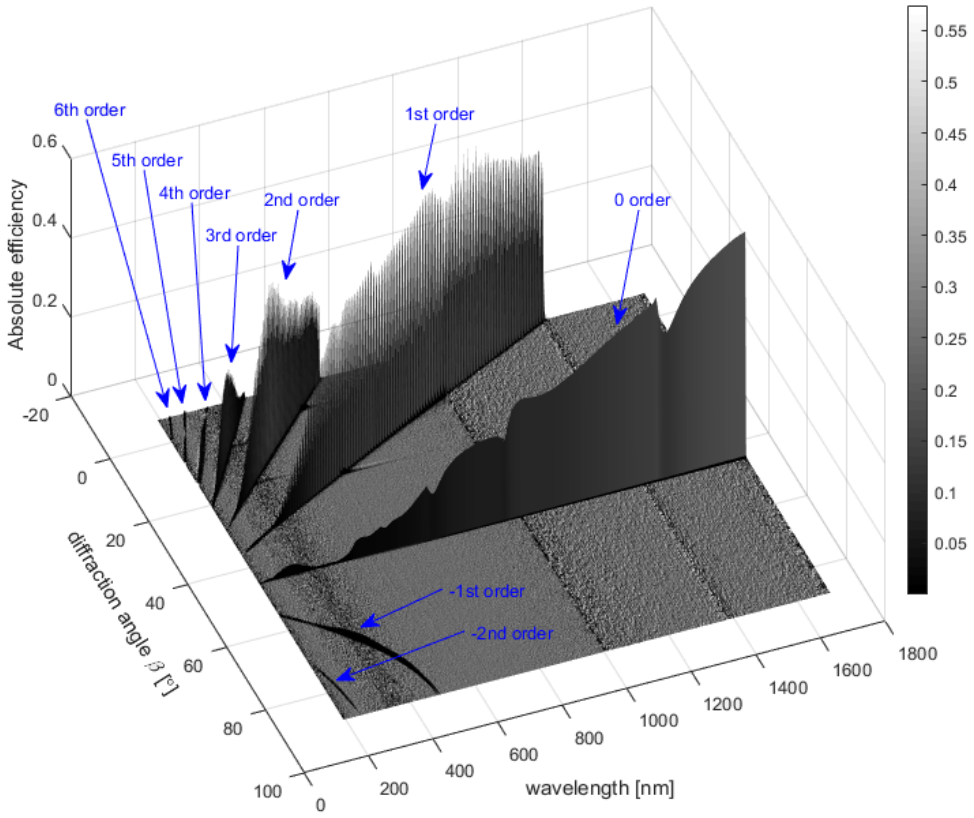

Figure 8.6: Spectral and angular dependances of the absolute diffraction efficiency for the $d = 1000$ nm blazed diffraction grating.

The first diffraction order exhibits the highest intensity distribution, even higher then the specular order, which is in perfect match with the principle of the ideal diffraction gratings, however it is clear, that the measured grating is far away from the idealty.

From Fig. 8.6 there are further obvious the intensity sharp peaks and drops, especially within the specular reflection. This phenomenom was first observed by Wood [80], and is so called the Wood anomally. They occure only for p-polarized wave (the wave vector lyes in the plane perpendicular to the grating grooves profile), and the wavelength differs with the type of the metal used for a coating of the grating. Fano [81] proposed, that the p-polarized wave do excite surface plasmon propagating normal to the grating grooves. Figure 8.7 exhibits strong Wood's anomalies, see the specular order. Note, that for s-polarized wave, no Wood anomaly occurs, see Fig. 8.8.

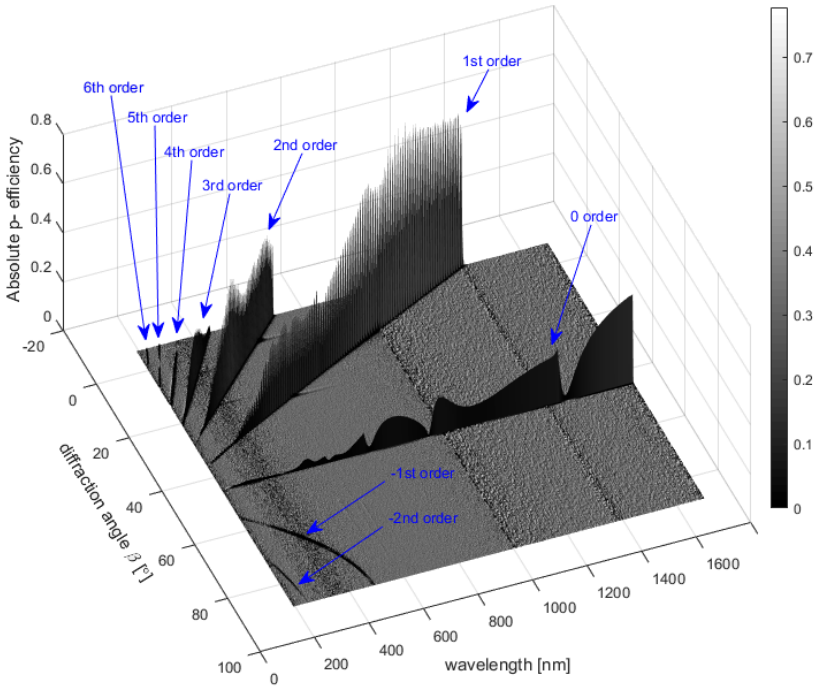

Figure 8.7: Spectral and angular dependances of the p-polarized light absolute diffraction efficiency for the $d = 1000$ nm blazed diffraction grating.

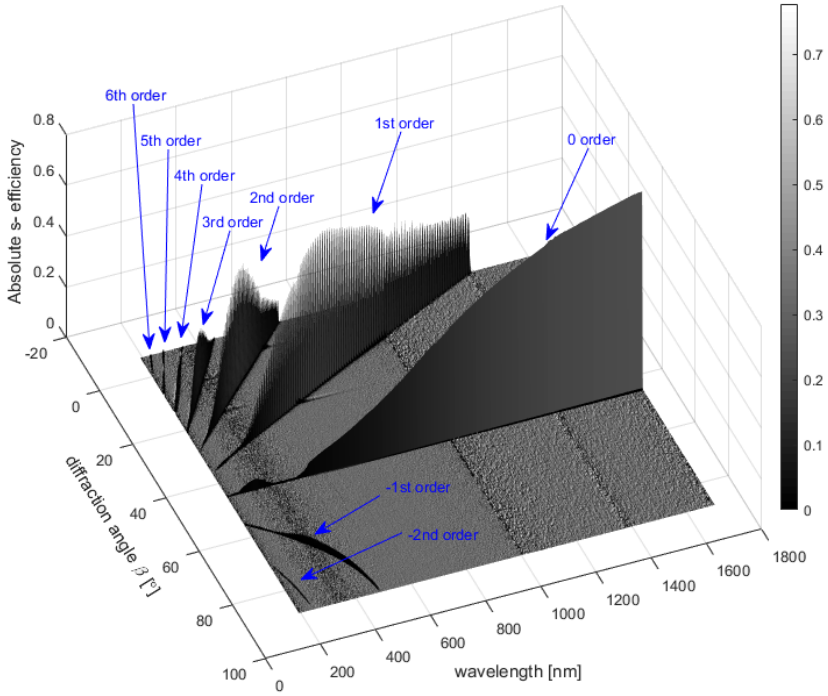

Figure 8.8: Spectral and angular dependances of the s-polarized light absolute diffraction efficiency for the $d = 1000$ nm blazed diffraction grating.

Figure (8.6) can be rearranged for the better orienation, so the z-axis lyes towards the reader – top view of Fig. (8.9).

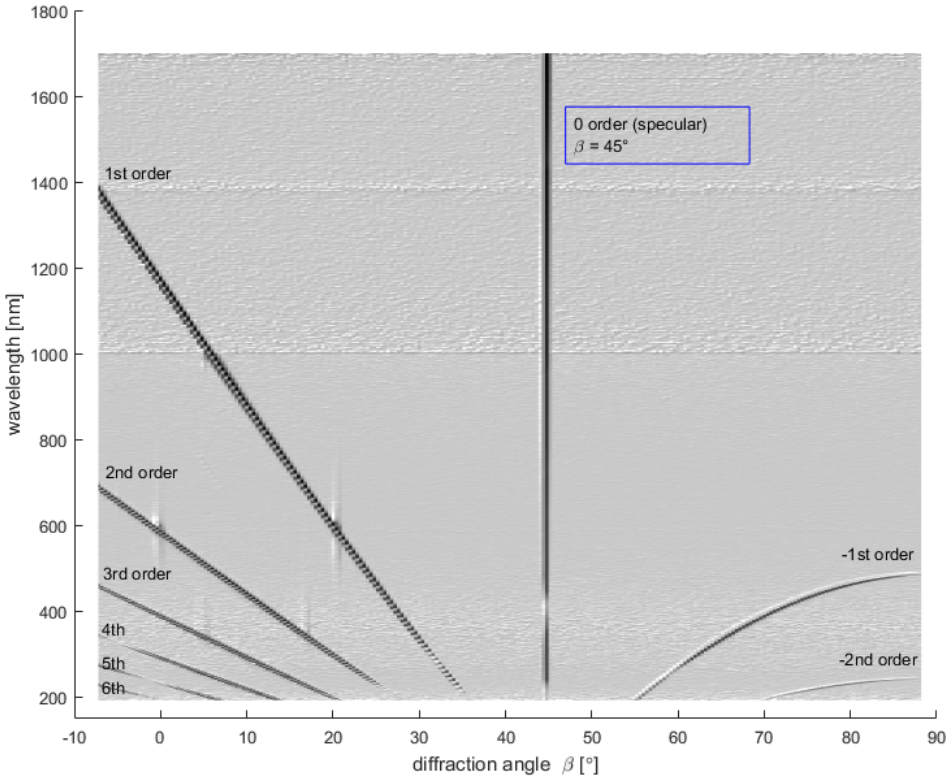

Figure 8.9: Spectral and angular dependances of the absolute diffraction efficiency for the $d = 1000$ nm blazed diffraction grating. Specular reflection is given by $\beta = \varphi = 45°$ condition, $m \neq 0$ orders satisfy Eq. (8.2).

The specular reflection corresponds to the angle of incidence, so $\beta = \varphi = 45°$. The $m \neq 0$ diffracted orders angular distribution differs with the wavelength according to the Eq. (8.2). Theoretically, the negative orders distribution continues above $\beta = 90°$, however they are suppressed by the dimension of the grating, but for the rigorous theoretical treatment [82], it is necessary to consider even the orders propagating along the surface of the grating. These orders are called evanescent.

9 Conclusion and perspective

One of the main goals of this thesis was to improve current techniques of the measurements using Mueller matrix spectroscopic ellipsometry, and to propose new measurement techniques, that can act as an advatageous substitution of currently existing techniques.
The main original results are:

- The new original method of chiral solution optical activity measurement was proposed. The method, using Mueller matrix ellipsometer, offers precise specific rotation power calculations over much more extended spectral range, then in the case of the classic chemical spectrometers. As shown in Tab. 4.3, the calculated values for the wavelength of 589 nm are in very good match with the tabulated values.

- The monocrystals of different chemical compounds were grown by the slow evaporation method. Despite the fact, that this method is not perfectly accurate and stabile, very good quality monocrystals were grown after gaining advanced know-how (see Figs. 6.8, and 6.9). The optimal parameters for the growth were empirically determined, so the method is well repeatable then. The optical characterization of these crystals would bring more insight into the further applications, as they can be potentially used as the sources for the terahertz lasers.

- The dielectric tensor spectra determination was calculated on pyrite and cassiterite minerals. The basic characteristics and the behaviour of the crystals were verified, the permittivity tensors were calculated using Kramers-Kronig consistent models.

- Another new and original method is based on the hardware reconfiguration of the Woollam RC2 spectroscopic ellipsometer, so the measurements of the diffraction structures is accurate and fully automated. The diffraction efficiencies of the blazed diffraction gratings were calculated. This method is sensitive enough to register even the 6th diffraction order, as shown in Fig. 8.6.

The perspective and the goal of my upcoming work is:

- to get more practice and experiences on the field of the crystallization techniques and great focus will lay on the improvement of fine crystal preparation for the ellipsometric measurements. Dielectric tensor spectra of the grown crystals will be calculated.

- to understand the optical activity phenomena within the bulk samples (anisotropic crystals) and to study the optical activity in infrared and terahertz spectra. My recent plans is to measure the tempertaure dependances of the optical activity of the chiral solution. This measurements will form the basis for the mutarotation kinetics study and rate constants calculations.

- to extend the diffraction efficiency measurements to the much more complicated structures, e.g. safety holograms and to compare the diffracted intensities with RCWA or Fourier-transform based calculations.
- to extract the diffraction efficiency information from the Mueller matrix spectra.
- to understand Mueller matrix decompositions into very detail and effectivelly use them on particularly complicated biological structures.

My very first work was aimed on the Mueller matrix spectroscopic ellipsometry and dielectric tensor determination of one-dimensional antiferromagnet Cu(1,3-diaminopropane)Cl_2 single crystal, and was presented at the poster section on the NanoOstrava 2017 conference [83].

The measurements and calculations of the specific rotatory power and optical activity temperature dependances will be presented at the 21st Czech-Polish-Slovak optical conference on wave and quantum aspects of contemporary optics in a form of the oral presentation.

References

[1] Fujiwara, H. *Spectroscopic ellipsometry: principles and applications.* Hoboken, NJ: John Wiley, c2007. ISBN 0470016086,

[2] Jellison, G. E., L. A. Boatner, J. D. Budai, B.-S. Jeong, and D. P. Norto *Spectroscopic ellipsometry of thin film and bulk anatase (TiO2)* J. Appl. Phys., 2003, vol. 93, iss. 12, pp. 9537–9541,

[3] Arteaga, O. *Mueller matrix polarimetry of anisotropic chiral media.* Bienni, 2010. Dissertation. Universitat de Barcelona,

[4] Postava, K., R. Sýkora, D. Legut, and J. Pištora *Determination of Anisotropic Crystal Optical Properties Using Mueller Matrix Spectroscopic Ellipsometry.* Proc. Mat. Sci., 2016, vol. 12, pp. 118–123,

[5] Arteaga, O., E. Kuntman, J. Antó, E. Pascual, A. Canillas and E. Bertran. *Mueller matrix microscopy on a Morpho butterfly.* J. Phys.: Conf. Ser. No. 605 012008, pp. 1–8,

[6] Novikova, T., J. Rehbinder, S. Deby, H. Haddad, J. Vizet, A. Pierangelo, P. Validire, A. Benali, B. Gayet, B. Teig, A. Nazac, B. Drévillon, F. Moreau, and A. De Martino. *Multi-spectral Mueller Matrix Imaging Polarimetry for Studies of Human Tissue.* 2016. ResearchGate,

[7] Rehbindera, J., S. Deby, H. Haddad, B. Teig, A. Nazac, A. Pierangelo, F. Moreau. *Diagnosis of uterine cervix cancer using Müller polarimetry: a comparison with histopathology.* N. Biophot. Tech. App. III, 2015, SPIE-OSA conf. paper,

[8] Jean Rehbinder., Huda Haddad, S. Deby, B. Teig, A. Nazac, T. Novikova, A. Pierangelo, and F. Moreau. *Ex vivo Mueller polarimetric imaging of the uterine cervix: A first statistical evaluation.* J. Biomed. Opt., 2016, vol. 21, iss. 7, pp. 2291-2305,

[9] Pierangelo, A., A. Benali, M.-R. Antonelli, T. Novikova, P. Validire, B. Gayet, and A. De Martino1 *Ex-vivo characterization of human colon cancer by Mueller polarimetric imaging.* J. Biomed. Opt., 2011, vol. 21, iss. 2, pp. 1582-1593,

[10] Brehonnet, F. Le Roy., and B. Le Jeune. *Utilization of Mueller matrix formalism to obtain optical targets depolarization and polarization properties.* Prog. Quant. Electr., 1997, vol. 21, iss. 2, pp. 109–151,

[11] Lu, S-Y., R. A. Chipman *Interpretation of Mueller matrices based on polar decomposition.* J. Opt. Soc. Am. A, 1996, vol. 13, iss. 5, pp. 1106-1113,

[12] Ossikovski, R. *Analysis of depolarizing Mueller matrices through a symmetric decomposition.* J. Opt. Soc. Am. A, 2009, vol. 26, pp. 1109-1118,

[13] Ossikovski, R., D. De Martino, and S. Guyot. *Forward and reverse product decomposition of depolarizing Mueller matrices.* Opt. Lett., 2007, vol. 32, pp. 689–691,

[14] Shukla, P., and A. Pradhan. *Mueller decomposition images for cervical tissue: Potential for discriminating normal and dysplastic states.* Opt. Express, 2009, vol. 17, iss. 3, pp. 1600-1609,

[15] Halliday, D., R. Resnick a J. Walker, Dub, P. (ed.), *Fyzika 2*, reworked ed. Translation: M. Černý. Brno: VUTIUM, c2013. University textbooks translations. ISBN 978-80-214-4123-1,

[16] Saleh, B. E. A. and M. C. Teich. *Fundamentals of photonics.* 2nd ed. Hoboken, N.J.: Wiley Interscience, 2007. ISBN 978-0471358329,

[17] Azzam, R. M. A. and N. M. Bashara. *Ellipsometry and polarized light.* New York: sole distributors for the USA and Canada, Elsevier North-Holland, 1977. ISBN 0720406943,

[18] Dostál, Z. *Lineární algebra.* Ostrava: VŠB-Technická univerzita, 2001. ISBN 80-7078-832-1,

[19] Garcia-Caurel, E., R. Ossikovski, M. Foldyna, A. Perangelo, B. Drévillon a A. de Martino. *Advanced Mueller Ellipsometry Instrumentation and Data Analysis.* Losurdo, M. a K. Hingerl, ed. *Ellipsometry at the Nanoscale.* Berlin, Heidelberg: Springer Berlin Heidelberg, 2013, s. 31-143 ISBN 978-3-642-33955-4,

[20] Gil J. J., and E. Bernabeu. *A depolarization criterion in Mueller matrices.* Opt. Act., 1985, vol. 32, Iss. 3, pp. 259-261,

[21] Cloude, S. R. *Group theory and polarisation algebra.* Optik, 1986, vol. 75, Iss. 1, pp. 26-36,

[22] Ossikovski, R., J. J. Gil, and I. San José. *Poincaré sphere mapping by Mueller matrices.* J. Opt. Soc. Am. A, 2013, vol. 26, pp. 2291-2305,

[23] Azzam, R. M. A., *Photopolarimetric measurement of the Mueller matrix by Fourier analysis of a single detected signal.* Opt. Lett., 1978, vol. 2, pp. 148-150 ,

[24] Smith, M. H., *Optimization of a dual-rotating-retarder Mueller matrix polarimeter.* Appl. Opt., 2002, vol. 41, pp. 2488-2493,

[25] Azzam, R. M. A. *A simple Fourier photopolarimeter with rotating polarizer and analyzer for measuring Jones and Mueller matrices.* Opt. Comm., 1978, Vol. 25, Iss. 2, pp. 137-140, ISSN 0030-4018,

[26] Wald, G. *The origin of optical activity.* Ann. NY Acad. Sc., 1957, vol. 69, pp. 352-368,

[27] Ernest, Z. *Introduction to Chirality and Chiral Centers.* SOCRATIC [online]. Cupertino, CA: Apple Inc., 2014. URL: https://socratic.org/organic-chemistry-1/r-and-s-configurations/introduction-to-chirality-and-chiral-centers ,

[28] McMurry, J. *Organic chemistry.* 8th ed., Belmont: Brooks/Cole, c2012. ISBN 9780840054449,

[29] Vollhardt, K. P. C. a N. E. Schore. *Organic chemistry: structure and function. 7th edition.* New York: W.H. Freeman and Company, 2014. ISBN 978-1464120275,

[30] Barron, Laurence. *Molecular light scattering and optical activity.* 2nd ed. Cambridge: Cambridge University Press, 2009. ISBN 9780521121378,

[31] Jirgensons, B. *Optical Activity of Proteins and Other Macromolecules.* 2nd, Revised and Enlarged Edition. Berlin, Heidelberg: Springer Berlin Heidelberg, 1973. ISBN 9783642877155,

[32] Wlodarczyk, P., K. Kaminski, M. Paluch, and J. Ziolo. *Mutarotation in D-Fructose Melt Monitored by Dielectric Spectroscopy.* J. Phys. Chem. B, 2009, vol. 113, pp. 4379-4383,

[33] Wong, S. Y., R. K. Bund, R. K. Connelly, and R. W. Hartel. *Determination of the dynamic limit for α-lactose monohydrate crystallization.* Int. Dairy J., 2011, vol. 21, pp. 839-847,

[34] Rumble, J. R. *CRC Handbook of Chemistry and Physics*, c2018, 98th edition,

[35] Simpson, J. *The functions of the salivary glands of Apis mellifera.* J. Insect Phys., 1960, vol. 4, pp. 107–108,

[36] Nordic Sugar: Member of Nordzucker Group. *The functional properties of sugar – on a technician level.* 1014 Copenhagen K, Denmark. URL: http://www.nordicsugar.com ,

[37] Engauge Digitizer: Extracts data points from images of graphs [online]. Markum Mitchell. URL: http://markummitchell.github.io/engauge-digitizer/ ,

[38] Feynman, R. P. *QED: the strange theory of light and matter.* Princeton, N. J.: Princeton University Press, c1985. ISBN 9780691083889,

[39] Rhodes, D. and A. Klug. *Helical periodicity of DNA determined by enzyme digestion.* Nature, 1980, vol. 586, pp. 573–578,

[40] Zamarský, V., H. Raclavská and D. Matýsek. *Mineralogie a krystalografie pro FMMI.* Ostrava: VŠB – Technická Univerzita, 2008. ISBN 978-80-248-1904-4,

[41] Mirman, R. *Point groups, space groups, crystals, molecules.* London: World Scientific, c1999. ISBN 978-981-02-3732-5,

[42] Nelson, S. A. *Introduction and Symmetry Operations.* Earth and Environmental Sciences 2110, Mineralogy [online]. Tulane Uiversity, 2013. URL: https://www.tulane.edu/∼sanelson/eens211/introsymmetry.htm ,

[43] Neumann, F. E., O. E. Meyer (ed.) *Vorlesungen über die Theorie der Elastizität der festen Körper und des Lichtäthers*, 1885. Leipzig: B. G. Teubner-Verlag,

[44] Yeh, P. *Optics of anisotropic layered media: A new 4x4 matrix algebra.* Surface Science, 1980, vol. 96, pp. 41–53,

[45] Czochralski, J. *A new method for the measurement of the crystallization rate of metals.* Zeitschrift für Physikalische Chemie, 1918, vol. 92, pp. 219–221,

[46] Pfann, W. G. *Zone melting.* Science, 1962, vol. 135, iss. 3509, pp. 1101–1109,

[47] Gudala, M. *Modelling of methane hydrate formation and dissociation in presence of surfactants by chemical affinity*, 2013, ResearchGate,

[48] Moore, W. J. *Physical chemistry.* 5th ed. –. Englewood Cliffs, N.J: Prentice-Hall, 1972. ISBN 9780582442344,

[49] Brdička, R., M. Kalousek, and A. Schütz. *Úvod do fyzikální chemie.* 2. dopl. a přeprac. vyd. Praha: SNTL - Nakladatelství technické literatury, 1972,

[50] Langmuir, I. *The adsorption of gasses on plane surfaces of glass, mica and platinum.* J. Am. Chem. Soc., 1918, vol. 40, iss. 9, pp. 1361–1403,

[51] Davey, R. J. *The effect of impurity adsorption on the kinetics of crystal growth from solution.* J. Crystal Growth, 1976, vol. 34, iss. 1, pp. 109–119,

[52] Kubota, N., and J. W. Mullin. *A kinetic model for crystal growth from aqueous solution in the presence of impurity.* J. Crystal Growth, 1995, vol. 152, pp. 203–208,

[53] Martins, P. M., F. A. Rocha, and P. Rein. *The influence of impurities of the crystal growth kinectics according to a competitive adsorption model.* Crystal Growth & Design, 2006, vol. 6, iss. 12, pp. 2814–2821,

[54] Moovendaran, K., and S. Natarajan. *Unidirectional growth and characterization of L-tartaric acid single crystals.* J. App. Crystallography, 2013, vol. 46, pp. 1–6, ISSN: 0021-8898,

[55] Krishnan, S., C. J. Raj, R. Robert, and S. J. Das. *Growth and characterization of succinic acid single crystals.* Cryst. Res. Technol., 2007, vol. 11, pp. 1087–1090,

[56] Krishnan, S., C. J. Raj, and S. J. Das. *Growth and characterization of novel ferroelectric urea-succinic acid single crystals.* J. Crys. Growth, 2008, vol. 310, pp. 3313–3317,

[57] Kumaresan, R., and S. M. Babu. *Crystal growth and characterization of sucrose single crystals.* Mat. Chem. Phys., 1997, vol. 49, pp. 83–86,

[58] Dalman, L. W. *The Solubility of Citric and Tartaric Acids in Water.* J. Am. Chem. Soc., 1937, vol. 59, pp. 2547–2549,

[59] Apelblat, A. and E. Manzurola. *Solubility of oxalic, malonic, succinic, adipic, maleic, malic, citric, and tartaric acids in water from 278.15 to 338.15 K.* J. Chem. Thermodynamics, 1987, vol. 19, pp. 317–320,

[60] Changgeng P., M. N. Chan, and Ch. K. Chan. *The Hygroscopic Properties of Dicarboxylic and Multifunctional Acids: Measurements and UNIFAC Predictions.* Environ. Sci. Technol., 2001, vol. 35, pp. 4495–4501,

[61] Sivasankari, B., and P. Selvarajan. *Characterization of Urea L-Malic Acid (ULMA) Crystals Grown in Water, Acetone and Ethanol.* J. Exp. Sc., 2010, vol. 1, pp. 01–03,

[62] Matos Gomesa, E. de, V. Venkataramanana, E. Nogueiraa, M. Belsleya, F. ProencËab, A. Criadoc, M.J. Dianezc, M. D. Estradac, and S. Perez-Garrido *Synthesis, crystal growth and characterisation of a new nonlinear optical material Ð urea L-malic acid.* Synth. Metals, 2000, vol. 115, pp. 225–228,

[63] Vinothkumar, P., K. Rajeswari, R. Mohan Kumar, and A. Bhaskaran. *Structural, optical, thermal and mechanical properties of Urea tartaric acid single crystals.* Spectrochimica A: Mol. and biomol. spectr., 2015,

[64] Yao, G.-B., L. Wang, Y.-P. Sun, J.-K. Yi, L. Meng, and H.-K. Zhao. *Ternary Phase Diagram for Systems of Succinic Acid + Urea + Water, Glutaric Acid + Urea + Water, and Adipic Acid + Urea + Water at 288.15 and 303.15 K.* J. Chem. Eng. Data, 2014, vol. 59, pp. A–I,

[65] Werner, E. A. *Urea as a Hygroscopic Substance.* Nature, 1937, p. 512,

[66] Passchier, C. W., and R. A. J. Trouw. *Microtectonics.* Berlin [u.a.]: Springer, 2005. ISBN 9783540293590,

[67] Hu, J., Y. Zhang, M. Law, and R. Wu. *Dielectric function representation by B-splines.* Phys. Stat. Sol. A, 2008, vol. 205, Iss. 4, pp. 715–719,

[68] Hu, J., Y. Zhang, M. Law, and R. Wu. *Increasing the Band Gap of Iron Pyrite by Alloying with Oxygen.* J. Am. Chem. Soc., 2012, vol. 134, Iss. 32, pp. 13216–13219,

[69] Subedi, I., K. P. Bhandari, R. J. Ellingson, and N. J. Podraza. *Near infrared to ultraviolet optical properties of bulk single crystal and nanocrystal thin film iron pyrite.* Nanotechnology, 2016, vol. 27, iss. 29, pp. 1–9,

[70] Jellison, G. E., and F. A. Modine *Parameterization of the optical functions of amorphous materials in the interband regione.* Appl. Phys. Lett., 1996, vol. 69, pp. 371–373,

[71] Zhou, W., Y. Liu, Y. Yang, and P. Wu. *Band Gap Engineering of SnO_2 by Epitaxial Strain: Experimental and Theoretical Investigations.* J. Phys. Chem. C, 2014, vol. 118, Iss. 12, pp. 6448–6453,

[72] Rockenberger, J., and U. zum Felde. *Near edge X-ray absorption fine structure measurements (XANES) and extended X-ray absorption fine structure measurements (EXAFS) of the valence state and coordination of antimony in doped nanocrystalline SnO_2.* J. Chem. Phys., 2000, vol. 112, p. 4296,

[73] Johari, A., M. C. Bhatnagar, and V. Rana. *Effect of substrates on structural and optical properties of tin oxide (SnO2) nanostructures.* J. Nanosci. Nanotechnol., 2012, vol. 12, Iss. 10, pp. 7903–7908,

[74] Gray, D. F. *The observation and analysis of stellar photospheres.* 3rd ed. Cambridge University Press, New York, 2005. ISBN 13978-0-521-85186-2,

[75] Bonod, N., and J. Neauport. *Diffraction gratings: from principles to applications in high-intensity lasers.* Adv. Opt. and Phot., 2016, vol. 8, iss. 1, pp. 1–44,

[76] Casini, R., and P. G. Nelson. *On the intensity distribution function of blazed reflective diffraction gratings.* J. Opt. Soc. Am. A, 2014, vol. 31, iss. 10, pp. 2179–2184,

[77] Gratings Tutorial [online]. Thorlabs, Inc., 1999-2018. URL: https://www.thorlabs.com/ ,

[78] ISO 17901-1:2015(E). *Optics and photonics - Holography: Part 1: Methods of measuring diffraction efficiency and associated optical characteristics of holograms.* 1st edition, 2015,

[79] RC2 Ellipsometer. *J. A. Woollam: Ellipsometry Solutions* [online]. Lincoln, NE 68508, United States: J.A. Woollam Co., 2017. URL: https://www.jawoollam.com/products/rc2-ellipsometer ,

[80] Wood, R. W. *On a remarkable case of uneven distribution of light in a diffraction grating spectrum.* 1902, Proc. Phys. Soc., vol. 18, pp. 269-–275,

[81] Fano, U. *The theory of anomalous diffraction gratings and of quasi-stationary waves on metallic surfaces Sommerfeld's waves.* 1941, J. Opt. Soc. Am., vol. 3, pp. 213-–222,

[82] Li, L. *Use of Fourier series in the analysis of discontinuous periodic structures* . J. Opt. Soc. Am. A, 1996, vol. 13, iss. 9, pp. 1871–1876,

[83] Vala D., K. Postava, D. Legut, U. D. Wdowik, A. Orendáčová, R. Tarasenko, and J. Pištora. *Spectroscopic ellipsometry of Cu(tn)Cl2 molecular crystal.* Poster session presented at: 4th international Nanomaterials and Nanotechnology meeting NanoOstrava, 2017, Ostrava, Technical University of Ostrava.